

Technical Report

EXPERIMENTAL AND NUMERICAL ANALYSIS OF
ELECTRIC CURRENTS AND ELECTROMAGNETIC
BLUNTING OF CRACKS IN THIN PLATES

G. R. Doelp, J. F. Abel, and F. C. Moon

Department of Structural Engineering Report
Number 84-12

submitted to the
Office of Naval Research
Structural Mechanics Program, Material Sciences Division
ONR Contract No. N00014-79-C-0224
Task No. NR 064-621

Departments of Structural Engineering
and Theoretical & Applied Mechanics
Cornell University
Ithaca, New York 14853

December 1984

ABSTRACT

Two problems in electromagnetics are studied: numerical analysis of electric currents in thin plates and experimental investigation of electromagnetic crack-tip blunting. In the first part, electric currents in thin plates are analyzed numerically with emphasis on expanding the capabilities of existing finite element programs. Specifically, the ability to calculate transport currents is added to programs which originally computed only induced currents. The final programs are capable of handling transport currents alone or combined with induced currents generated by a transient external magnetic field. Experimental and analytical verification of the resulting program is presented.

The second half of this study deals with the blunting of fatigue cracks by melting a hole at the crack tip by electromagnetic means. This technique is investigated experimentally for stainless steel 304 and titanium alloy Ti-6Al-4V. The blunting technique is described in detail, and the results from the testing program are presented. Analysis of the data emphasizes the hole sizes produced and their effect on the ultimate strength and fracture resistance of the test specimens. Electromagnetic blunting increases the ultimate static stress of stainless steel 304 plates by up to 19 percent and of Ti-6Al-4V by up to 78 percent. The effect of electromagnetic blunting on resistance to further fatigue remains to be investigated.

ACKNOWLEDGMENTS

This report is essentially a reproduction of the thesis submitted in August 1984 by the first author in partial fulfillment for the degree of Master of Science. The research was supervised by the second two authors, Professors John F. Abel and Francis C. Moon.

The authors would also like to thank Professor H. D. Conway, Walter Gerstle, and Professor Herbert Hui for their recommendations on various aspects of the study. In addition, the assistance of Gary Gabriel and Bryon Shapey with the experimental work is greatly appreciated. Harindra Rajiyah, Waleed Khushefati, Riyadh Aziz, and Mahmoud Khater conducted the finite element stress analysis of the test specimen geometry.

TABLE OF CONTENTS

	<u>Page</u>
CHAPTER 1: INTRODUCTION	1
1.1 NUMERICAL ANALYSIS OF ELECTRIC CURRENTS	1
1.2 ELECTROMAGNETIC CRACK TIP BLUNTING	4
1.3 OVERVIEW	8
 CHAPTER 2: BACKGROUND THEORY	 9
2.1 FRACTURE MECHANICS FUNDAMENTALS	9
2.1.1 Background	10
2.1.2 The Energy Balance Approach	14
2.1.3 The Stress Intensity Factor Approach	16
2.1.3.1 The Case Under Study: Mode I	20
2.1.3.2 The Stress Concentration Factor Relationship	22
2.1.3.3 Determining Stress Intensity Factors	23
2.1.3.4 Critical Stress Intensity Factors	25
2.2 MAGNETOMECHANICS THEORY	27
2.2.1 Basic Concepts	27
2.2.2 Application of the Theory to Plates	31
2.2.2.1 Solution Techniques	31
2.2.2.2 Types of Solution	33
2.2.2.3 Assumptions	33
2.2.3 Eddy Current Analysis Using a Stream Function	35

	<u>Page</u>
2.2.3.1 Definition of the Stream Function.	35
2.2.3.2 The Basic Governing Equation.	37
2.2.3.3 The Induced Field Term.	37
2.2.3.4 Governing Equation for the Steady State Problem.	38
 CHAPTER 3: FINITE ELEMENT ANALYSIS OF EDDY CURRENTS AND TRANSPORT CURRENTS.	 42
 3.1 EXISTING PROGRAMS AND MOTIVATION FOR FURTHER DEVELOPMENT	 42
3.1.1 Finite Element Modeling of the Stream Function.	43
3.1.2 A General Overview of the Programs EDDY1 and EDDY2.	45
3.2 FORMULATION OF THE TRANSPORT CURRENT PROBLEM.	47
3.2.1 The General Two-Dimensional Case.	48
3.2.2 Governing Equation for a Rectangular Plate	55
3.2.3 Governing Equation for a One-Dimensional Strip.	56
3.3 IMPLEMENTING TRANSPORT CURRENT CAPABILITY IN THE ONE DIMENSIONAL CASE	58
3.3.1 Nondimensional Steady State Formulation for the One-Dimensional Case.	59
3.3.2 Changes to the Finite Element Formulation	60
3.3.2.1 Changes to the System of Equations.	61
3.3.2.2 Changes at the Program Level	63
3.3.2.3 Implementing the Changes in EDDY1	64

	<u>Page</u>
3.3.3 The Induced Field Edge Terms.	65
3.3.3.1 The Significance of the Edge Terms.	65
3.3.3.2 Including the Edge Term Effects.	68
3.4 VERIFICATION OF THE TRANSPORT CAPABILITY IN EDDY1.	76
3.4.1 Related Changes to EDDY1.	76
3.4.2 Description of the Checks.	78
3.4.2.1 Comparison with Hand Calculation.	78
3.4.2.2 Verification Grid	79
3.4.2.3 Comparison of Induced Fields.	82
 CHAPTER 4: ELECTROMAGNETIC CRACK TIP BLUNTING.	 87
4.1 BASIC TESTING APPARATUS AND PROCEDURE	88
4.1.1 Fatigue Crack Generation.	88
4.1.2 Electromagnetic Blunting Operation.	91
4.1.3 The Analysis of Blunted Samples.	93
4.1.4 Studies on the Effect of Heating.	96
4.2 STAINLESS STEEL 304 SPECIMENS.	97
4.2.1 Fatigue Cracked Specimens.	99
4.2.2 Drilled Hole Specimens	104
4.2.3 Special Effects	105
4.2.3.1 Applied Magnetic Field.	108
4.2.3.2 Nitrogen Gas Cooling.	110
4.2.4 Discussion of Stainless Steel 304 Test Results	110

	<u>Page</u>
4.3 TITANIUM ALLOY (Ti6Al4V) SPECIMENS	115
4.3.1 Unloaded Fatigue Cracked Specimens	116
4.3.2 Tensile Loaded Fatigue Cracked Specimens	120
4.3.3 Discussion of Ti-6Al-4V Test Results.	126
 CHAPTER 5: STRESS ANALYSIS OF TEST SPECIMENS	 130
5.1 STRESS CONCENTRATION FACTORS.	130
5.2 FINITE ELEMENT ANALYSIS.	138
5.3 STRESS INTENSITY FACTORS.	151
5.3.1 Stress Intensity Factors in the Unblunted Case.	151
5.3.2 Stress Intensity Factors in the Blunted Case.	156
 CHAPTER 6: CONCLUSIONS.	 166
6.1 NUMERICAL ANALYSIS OF ELECTRIC CURRENTS.	166
6.1.1 Summary	167
6.1.2 Conclusions	168
6.1.3 Suggestions for Further Research.	169
6.2 ELECTROMAGNETIC CRACK TIP BLUNTING.	171
6.2.1 Summary.	171
6.2.2 Conclusions	172
6.2.3 Suggestions for Further Research.	176
 REFERENCES	 179

LIST OF FIGURES

<u>Figure</u>	<u>Page</u>
1.1 Typical Blunted Configuration in Stainless Steel 304.	7
2.1 Specimen Geometries	11
2.2 The Basic Modes of Crack Surface Displacement.	19
2.3 Coordinates at the Leading Edge of a Crack.	21
2.4 A Schematic of One Form of Magnetothermomechanical Coupling.	29
3.1 Two-Dimensional Plate Configurations.	49
3.2 Infinite One-Dimensional Plate.	57
3.3 Modified Solution Procedure.	62
3.4 Stream Function and Corresponding Current Distributions in an Infinite One-Dimensional Plate	66
3.5 Comparison of Current Distribution for Different Reynold's Numbers, computed by EDDY1.	73
3.6 Comparison of EDDY1 Pure Transport Current Solution with and without edge correction terms, $R = 5.0$	74
3.7 Verification Grid for EDDY1	80
3.8 Comparison of Induced Magnetic Field Distributions for a DC Current Strip with $I = 25$ Amps.	84
3.9 Comparison of Induced Magnetic Field Distributions for a DC Current Strip with $I = 50$ Amps	85
3.10 Comparison of Induced Magnetic Field Distributions for a DC Current Strip with $I = 75$ Amps.	86

<u>Figure</u>	<u>Page</u>
4.1 Standard Specimen Geometries.	89
4.2 Electromagnetic Blunting Apparatus	92
4.3 Blunted Hole Geometries	94
4.4 Effective Crack-Tip Radius vs. Current in SS304.	100
4.5 Equivalent Circular Hole Diameter vs. Current in SS304.	101
4.6 Ultimate Stress vs. Current in SS304.	102
4.7 Ultimate Stress vs. Effective Crack-Tip Radius in SS304.	103
4.8 Ultimate Stress vs. Drilled Hole Size in SS304 Razor Notched Specimens	106
4.9 Ultimate Stress vs. Drilled Hole Size in SS304 Fatigue Cracked Specimens.	107
4.10 The Effect of an External Magnetic Field and a Cooling Jet on Effective Crack-Tip Radius in SS304	109
4.11 Plastic Zone Size, p , as a Function of Stress Intensity Factor, K , and Yield Strength, σ_y , in Plane Stress	113
4.12 Effective Crack-Tip Radius vs. Applied Current in Unloaded Ti-6Al-4V	117
4.13 Ultimate Stress vs. Applied Current in Unloaded Ti-6Al-4V	118
4.14 Ultimate Stress vs. Effective Crack-Tip Radius in Unloaded Ti-6Al-4V	119
4.15 Effective Crack-Tip Radius vs. Applied Load in Ti-6Al-4V at 4kV	122
4.16 Ultimate Stress vs. Applied Load During Current Pulse in Ti-6Al-4V at 4KV	123
4.17 Ultimate Stress vs. Effective Crack-Tip Radius in Ti-6Al-4V Specimens Under Varied Load at 4 KV.	124

<u>Figure</u>	<u>Page</u>
4.18 Effective Crack-Tip Radius vs. Voltage in Ti-6Al-4V Under a Constant 700 lb Load	125
4.19 Ultimate Stress vs. Voltage in Ti-6Al-4V Under a Constant 700 lb Load	127
4.20 Comparison of Ultimate Stress vs. Effective Crack-Tip Radius for Stainless Steel 304, Unloaded Ti-6Al-4V, and Loaded Ti-6Al-4V	129
5.1 Superposition of Stress Concentration Factor Solutions for a Flat Test Specimen with a Single Edge Notch	132
5.2 Logarithmic Extrapolation of Stress Concentration Factor vs. r/a for a Flat Tension Bar with a U-Shaped Notch (Cole and Brown)	134
5.3 Logarithmic Extrapolation of Stress Concentration Factor vs. r/a for Bending of a Plate with a U-Notch (Leven and Frocht)	135
5.4 Test Specimen Configuration Used in Finite Element Stress Analysis	139
5.5 Variation of Maximum Normal Stress σ Along $\theta = 0$, $r/d = 0.009$, $a/d = 0.76^y$	141
5.6 Variation of Tangential Stress Around the Blunted Hole for $r/d = .009$	142
5.7 Variation of Tangential Stress Around the Blunted Hole for $r/d = .016$	143
5.8 Variation of Tangential Stress Around the Blunted Hole for $r/d = .017$	144
5.9 Variation of Tangential Stress Around the Blunted Hole for $r/d = .027$	145
5.10 Variation of Tangential Stress Around the Blunted Hole for $r/d = .038$	146
5.11 Stress Concentration Factors Based on Full Section	148
5.12 Stress Concentration Factors Based on Net Section	149

<u>Figure</u>	<u>Page</u>
5.13 Comparison of Net Section Stress Concentration Factors from Finite Element Analysis and Photoelastic Studies (Eqn. 5-4) for $a/d = 0.63$	150
5.14 Test Specimen Geometries for Computing K_I and K_{II}	154
5.15 Critical Apparent Stress Intensity Factor Computed from Equation (5-10) vs. Effective Crack-Tip Radius in Ti-6Al-4V	160
5.16 Critical Apparent Stress Intensity Factors Based on Stress Concentration Factors from Photoelastic Studies vs. Eff. Crack-Tip Radius in Ti-6Al-4V	163
5.17 Critical Apparent Stress Intensity Factors for Ti-6Al-4V Test Specimens based on Stress Concentration Factors from Finite Element Analysis	164
5.18 Comparison of Critical Apparent Stress Intensity Factors in Ti-6Al-4V Specimens Computed by Equation (5-10) and from Stress Concentration Factors Based on Photoelasticity and Finite Element Analysis	165

CHAPTER 1

INTRODUCTION

Two individual topics are considered in the research reported here: the numerical analysis of electric currents and electromagnetic crack tip blunting. The dual nature of this study requires a twofold approach be used, and therefore, this introduction is divided appropriately.

1.1 NUMERICAL ANALYSIS OF ELECTRIC CURRENTS

In the design of structures which are to be made of a conducting material and subjected in service to magnetic fields, the problem of induced currents is important. Both the external magnetic fields and the magnetic fields induced by the currents themselves interact with currents flowing in the structure to

generate forces. Hence, in problems such as these, it is necessary to compute these induced currents, which are known as eddy currents, in order to know the loadings on the structure.

Calculation of these eddy currents is especially important in structural situations involving strong magnetic fields. Examples of such situations include fusion reactors, superconducting motors and generators, magnetically levitated vehicles, transmission lines, magneto-hydrodynamic generators, and other electromagnetic devices. These structures are subjected to large magnetic forces because of the interaction between their fields and the eddy currents flowing in them. EDDY1 and EDDY2 are computer programs which were developed in earlier research to address these types of problems. In particular, EDDY2 analyzes currents induced in two dimensions, while EDDY1 considers the one-dimensional problem.

Structures such as these may also conduct directly applied currents, called transport currents, which interact with the magnetic fields to create additional forces. Magnetic forces created by transport currents in these structures may be large and, therefore, cannot be ignored. In their original versions, EDDY1 and EDDY2 lack the capability to address transport current problems. The principal objective of this part of the study is to extend the formulations of these programs to handle situations involving transport currents. Although the ideas presented here apply to both programs, the actual changes are only made in EDDY1.

In these programs the governing relationship and associated boundary conditions are formulated in terms of a stream function for the current. The local magnitude of the current is given by the gradient of the stream function, and its direction is perpendicular to the gradient direction.

Two major changes are required to implement the transport current capability. First, a rederivation of the governing integro-differential equation is necessary to account correctly for the magnetic field induced by the transport current. Second, the finite element formulation must be modified to include both the local and nonlocal (induced) effects of the nonzero boundary conditions associated with the applied current.

In the case of a two-dimensional plate with an applied transport current, the governing equation contains an additional integro-differential term not present in the original formulation used in EDDY2. Likewise, in the case of a one-dimensional plate there are two additional terms; one for each edge. These terms are referred to as "edge terms" because they are associated with the value of the stream function on the particular plate edges. As an alternative to calculating these terms in full, for simple geometries such as the one-dimensional plate, an equivalent field may be applied which produces the same effect as the edge terms.

The necessary changes in boundary conditions are accomplished by rearranging the finite element equations to include the constrained values as loading terms. Briefly, the changes required to do this in the programs are: input the boundary values, compute the necessary stiffness matrix, modify the load terms with appropriate constraining terms, and alter the program where homogenous boundary conditions are automatically assumed. For these changes there is no alternative approach as there is in the case of the governing differential equation.

By forcing the stream function to be zero on all plate boundaries the scope of the original programs was restricted to those problems in which the resulting currents flow in closed loops entirely within the conductor. The modifications open the possibility of solving problems where the resultant currents flow into and out of the conductor. For example, the problem of a conducting plate with a transport current imposed on it can now be analyzed.

1.2 ELECTROMAGNETIC CRACK TIP BLUNTING

One significant mode of failure for structures and structural components is brittle fracture. Failure by fracture, moreover, is frequently without warning, and therefore, such failures may be costly in terms of life and property.

Although cases of brittle fracture have been documented for years, this problem was not fully addressed until numerous ships failed in this manner during World War II. These failures initiated considerable research in the area of fracture mechanics. Despite an improved understanding of these problems, however, brittle fractures have continued to occur. An example of the continued problem is the 584-ft-long Tank Barge I.O.S. 3301 which broke in half in 1972 while at dock in calm water. Most of the documented failures of this type have been in airplanes, ships, pressure vessels, tanks, and bridges.

Much investigation into the behavior of cracks has been conducted, and the results have been used to develop suitable fracture-control plans for a variety of situations. This study focuses on the blunting of existing cracks and the increases in strength and fracture toughness possible by such methods.

In the proposed blunting technique, a sufficiently large current density is concentrated at the tip of a crack to cause melting. The necessary current may be either an induced current or a transport current, but only the latter is used in this study. Magnetic forces act on the molten material to create a hole at the crack tip. This results in a potential increase in fracture strength.

From a fracture mechanics perspective, the idea of electromagnetically blunting cracks is similar to the drilled-hole method of arresting cracks. In the latter approach, a hole is drilled at the tip of a crack to lower the stress concentration and keep the crack from growing. This technique is commonly used to stop crack growth in airplane components and bridges.

From an electromagnetic standpoint, the proposed method can be thought of as an extension of the use of induced currents for nondestructive testing. By inducing currents in a structure containing a crack, one can concentrate current at the tip of the crack. Localized heating occurs at the points where the current density is greatest. By infrared scanning one can detect the regions of higher temperature or "hot spots" and thereby locate the ends of the crack. Extending this method to blunting involves increasing the current to the point where melting occurs at the hot spots.

To investigate the blunting of cracks electromagnetically, experiments are conducted on long, thin plates. By subjecting the strips to a fatigue loading, one generates cracks in the side of each specimen. A current pulse is then applied to the sample and the resulting concentration of current produces a hole at the crack tip. Figure 1.1 shows a magnified view of a typical hole which was formed in stainless steel. Both blunted and unblunted strips are then tested for ultimate load.

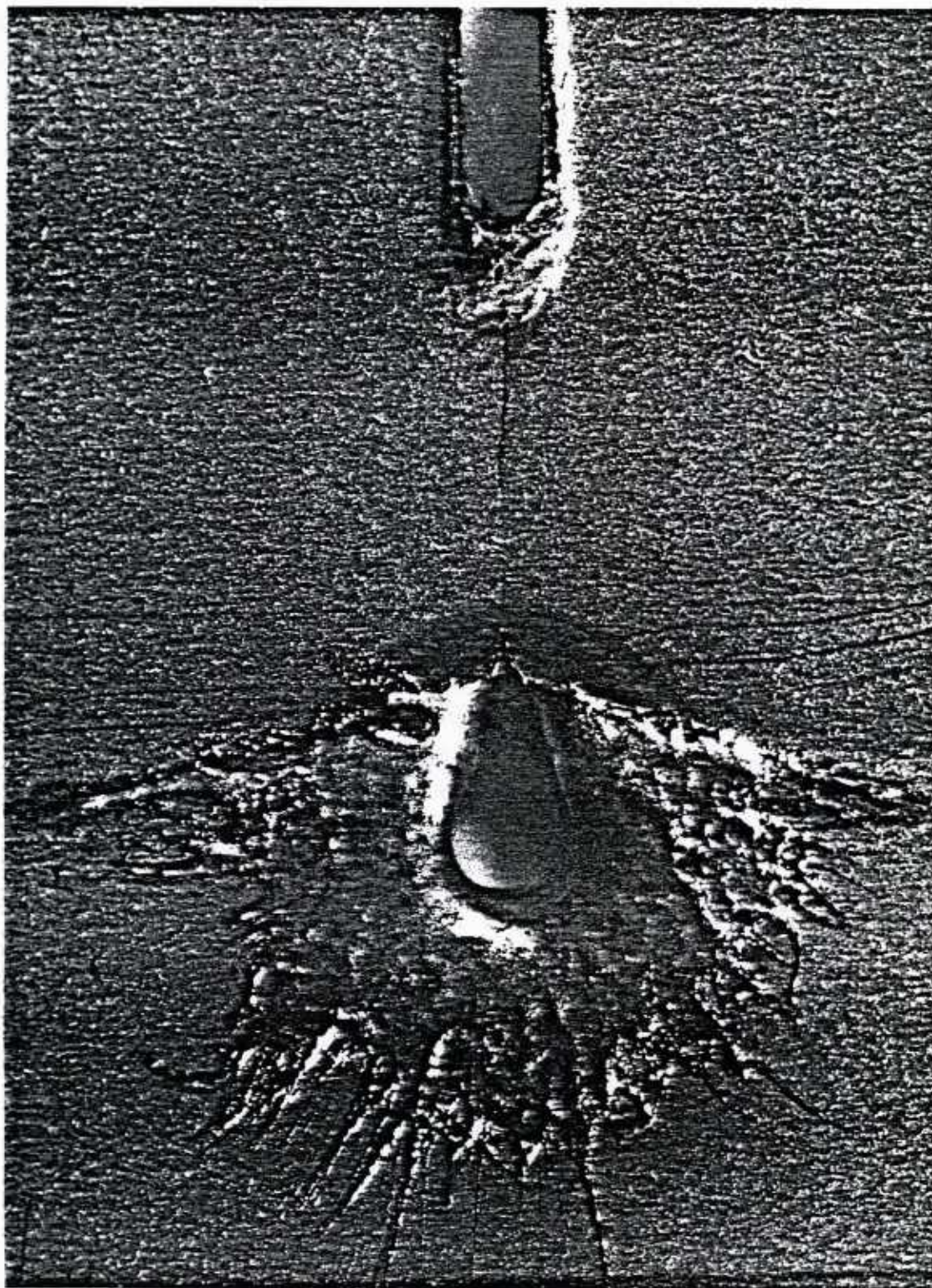


Figure 1.1 Typical Blunted Configuration in Stainless Steel 304
(Magnified 25X)

This study also analyzes the stresses in the geometry of the blunted specimens. These stresses are determined by analytical solutions and the finite element method. Results of these analyses are then used to express the data obtained from the blunting experiments in terms of apparent stress intensity factors at ultimate load.

1.3 OVERVIEW

As indicated at the beginning of this chapter, the entire discussion is divided according to the two electromagnetic problems under consideration: numerical analysis of electric currents and electromagnetic crack tip blunting. Chapter 2 consists of two parts, each of which covers the background theory for one of these areas. Chapter 3 is related to the finite element method as it is applied to the analysis of transport currents in this study. The experimental work involving the electromagnetic blunting of cracks is treated in Chapters 4 and 5. For each area, Chapter 6 contains a summary, a list of conclusions, and suggestions for further research.

CHAPTER 2

BACKGROUND THEORY

Two distinct fields of study are especially important to this work. They are fracture mechanics and magnetomechanics. The current chapter is divided into two main sections, each of which is devoted to one of these areas.

2.1 FRACTURE MECHANICS FUNDAMENTALS

This section provides a brief overview of fracture mechanics concepts as they apply to the problem at hand. There are two basic stress situations which need to be examined as part of this project. First is the stress field surrounding the fatigue crack, and second the changed stress pattern due to the blunted geometry.

In the case of the blunted geometry, it is desired to know the stress field around a circular hole at the end of a long

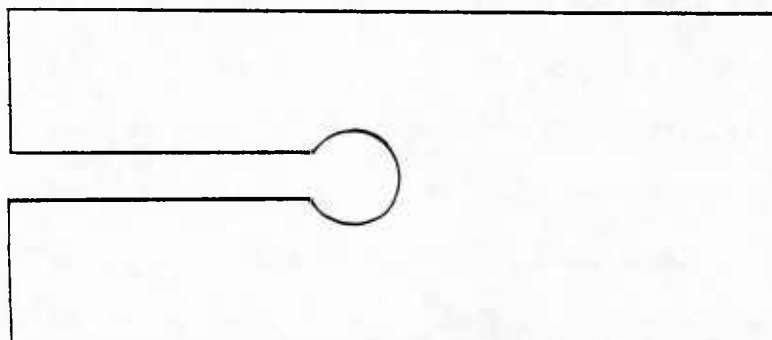
slender notch, Figure 2.1(a). Very little has previously been written about the state of stress for this configuration. However, a state of stress very similar to the one at hand will exist in the configuration shown in part (c) of that figure. The shaded regions shown in part (b) sustain little stress and, therefore, the stress field will be changed very little by ignoring them. This idea parallels the "equivalent ellipse" concept proposed by Cox [1] for ovaloids and similar shapes.

From the fracture mechanics literature it is evident that several methods have been proposed for the analysis of cracks and notches. There are three fundamental viewpoints from which these problems may be studied. These are: 1) the energy balance approach, 2) the stress intensity factor approach, and 3) the surface layer energy and strain energy density approach. The first and second methods have greater acceptance in the field of fracture mechanics and are more applicable to this study than the third. For completeness, the third approach is briefly discussed in the following background section, while entire sections are devoted to the first two approaches.

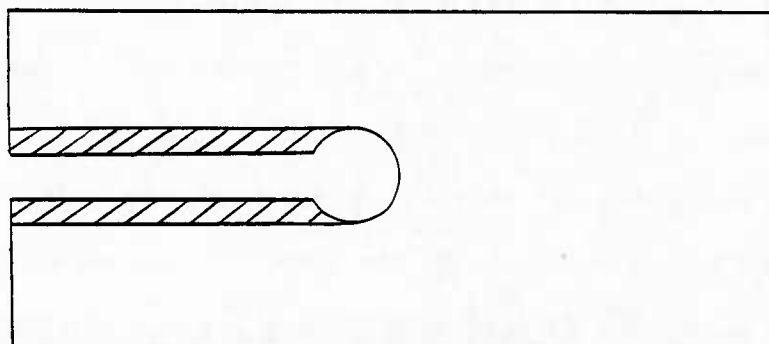
Preceding the descriptions of the first two techniques, a brief historical account of this area of fracture mechanics is given.

2.1.1 BACKGROUND

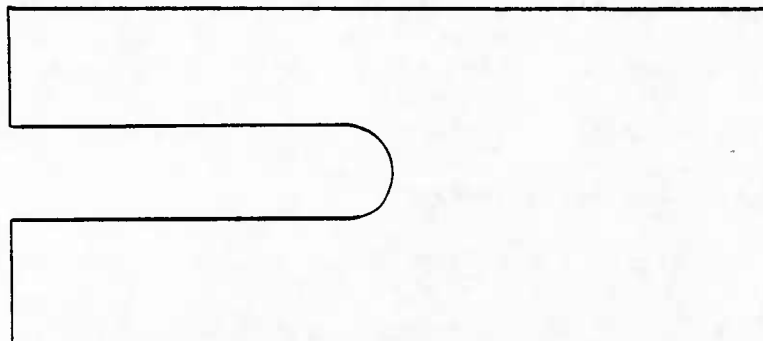
This section traces the development of fracture principles. One can see how improved theories have arisen to describe more accurately the conditions of stress around cracks, notches, and



(a) Blunted Crack



(b) Regions of Low Stress



(c) Geometry Considered

Figure 2.1 Specimen Geometries

other disturbances. Furthermore, this brief review helps to show how the different approaches are interrelated and what their relevance is to the problem under study.

Many of the initial theories in fracture mechanics were developed through study of the problems of a uniformly stressed plate containing an elliptical hole or an isolated crack. The literature on this subject frequently mentions the work of Inglis [2] in solving the elliptical hole problem as a significant first step in addressing fracture problems. Inglis' study analyzed the concentration of stress caused by the presence of the elliptical notch. Further studies in stress concentration for other shapes followed with the work of Neuber [3], Timoshenko and Goodier [4], and Savin [5].

Some difficulties arise in extending these stress concentration solutions to situations containing cracks. To make this transition various workers have used the notion that a crack is a limiting case of the slender elliptical hole [6]. In the elliptical hole the stress at the tips is proportional to the major-to-minor axes ratio. As this ratio goes to infinity, the case of the elliptical hole becomes that of a crack in the limit. Hence, according to the stress concentration idea, which is based on linear elasticity, the stresses become singular at the tip as the notch becomes a crack.

The stress concentration theory can be used to predict the failure of structural elements containing notches or other

non-singular disturbances. However, as Sih [7] points out in his discussion of Griffith's early work on fracture, this theory is not easily applied to cracked configurations as a failure criterion. Griffith used the stress concentration concept for notch failures and a completely separate theory for crack failures.

The separate theory developed by Griffith for cracks is based on an energy balance. Several modifications have since been suggested for this theory since Griffith first proposed it in 1921. The energy balance approach to crack analysis is discussed in the next section of this chapter.

The next major contribution to fracture mechanics was made in 1957 when Irwin [8] suggested a completely different approach than Griffith's for the study of cracks. Section 2.1.3 summarizes this theory which is known as the stress intensity factor approach. The concept advanced by Irwin considers the state of stress surrounding the crack tip.

Development of fracture mechanics theory up to this time still considered separate approaches for cracks and for notches. Recently, Sih [9] has proposed a consistent theory for both cracks and notches. Referred to as the surface layer energy and strain energy density approach, it considers an element always a finite distance in front of the crack tip. The theory assumes the crack will advance after the element has absorbed a critical amount of energy. This energy is then released upon material separation.

2.1.2 THE ENERGY BALANCE APPROACH

As mentioned earlier, the energy balance theory was first presented by Griffith in 1921. Since then, many adaptations and modifications to the basic theory have been suggested to improve and extend its applicability. A concise treatment of this theory is given by Hayes [10].

The energy approach is based on the principle that an existing crack will grow when the strain energy released during an increment of crack growth is greater than the energy required to form the new crack surfaces. Hence, with an excess amount of energy being given off, an unstable situation exists which causes the crack to propagate. This instability can be expressed by the relationship:

$$\delta U_{\text{tot}} > \delta U_s \quad (2-1)$$

in which δU_{tot} is the change in strain energy for an increment of crack growth and δU_s is the surface energy used in opening the crack increment. The utility of the energy balance theory is limited here by the need to compute these terms. Griffith was able to derive with the following equation for the critical stress, σ_{cr} , by assuming completely elastic behavior and the classical surface energy theory. For an isolated crack of length $2a$:

$$\sigma_{cr} = \sqrt{\frac{2E\gamma}{\pi a}} \quad (2-2)$$

in which γ is the specific surface energy and E is the modulus of elasticity.

To check his theory, Griffith ran a series of experiments with hard glass. Glass exhibits little plastic deformation before failure and hence conforms well to the assumption of pure elastic behavior. The experimental results, however, did not agree well with the theory in equation (2-2). Later, a refinement to the theory was suggested which produced conformity with the experimental results. In the latter refinement the surface energy term, 2γ , is replaced with a term, γ_p , which accounts for the energy absorbed by plastic deformation. This provides for a small area of plasticity around the crack tip.

Additional studies were done on this plastic surface energy term. These resulted in a further modification of Griffith's theory based on strain energy release concepts. To apply this theory, the strain energy release rates for various conditions must be determined experimentally.

Finally, the energy balance approach can be useful as a failure criterion for fracture studies but with several limitations. The foremost of these requires the area of yielding around the crack tip to be small relative to the dimensions of the structure. Also, sufficient accuracy appears to be possible only with the latest refinement of the theory which employs strain energy release rates. This necessitates adequate experimentation to determine these rates.

2.1.3 THE STRESS INTENSITY FACTOR APPROACH

The stress intensity factor approach is based on solutions from the theory of elasticity. Therefore, complete elastic behavior has been assumed. In reality, however, a region of yielding will always exist in the highly stressed area surrounding the crack tip. Hence, this theory is most appropriately applied to situations where the plastic zone can be assumed to be small relative to the other dimensions.

Before discussing the stress intensity factor approach further, two important points concerning its application to this work must be made. First, the stress intensity factor approach is devoted to the analysis of cracks or exceptionally slender notches which exhibit singular behavior at the tip. This theory was developed out of the need to compare the intensity of stress singularity between different cracks which was not possible with conventional theory. Therefore, only the unblunted crack geometry can be analyzed by this approach as it was originally proposed. This section describes the stress intensity factor approach in this context, while a suggested extension of the theory for the blunted crack geometry is treated in Chapter 5.

The second important point to be made involves the assumption of a small plastic zone. This assumption is not always valid when the theory is applied to plane stress situations such as plate

test specimens. The stress intensity factor approach is based on plane strain conditions which generally involve a small plastic zone. A situation of plane stress exists in the strips used in this study. Several difficulties to be discussed subsequently, arise when the concept of stress intensity factors is extended to the case of plane stress. The literature admits to inconsistent distinction between "plane stress" and "plane strain" and points to the need for further research to extend fracture analysis concepts to the former.

The stress intensity factor is based on linear elasticity and hence carries the restriction of "small-scale yielding" to situations where it is applied. Nevertheless, this method is the most widely used in fracture analysis and it is still applied to situations where the size of the plastic zone is considerable. The degree of accuracy required limits how large the nonlinear zone may be to still have an acceptable solution.

A correction to this theory for large-scale yielding has been proposed which considers an "effective crack size." Tada et al.[13] assert that this "effective crack size" correction is especially appropriate for observing trends and relating similar situations. One should bear in mind that the use of fracture analysis in this report is mainly for comparative purposes rather than a precise determination of the stress state in one case.

Based on the literature and related discussions [32], the modification of the stress intensity approach used in Chapter 5 is judged to be valid for the problem at hand.

The earlier discussion on fracture mechanics history indicated that the stress intensity factor approach was first proposed by Irwin [8]. Irwin based his method on the work in elasticity done by Westergaard [11].

These studies provide one with solutions for stresses and displacements around the crack tip. The solutions were developed for three different loading conditions. Figure 2.2 shows these three conditions which are known as the basic "modes" of crack surface displacement. Rolfe and Barsom [12] note that any crack configuration can be expressed as a superposition of these three modes. Likewise, the linear solution to any crack problem can be obtained by combining the solutions to each of the component configurations.

The fundamental premise of the stress intensity factor approach is that the pattern of stress (or strain) will be identical around any crack tip of a given mode. The magnitude of the stresses (or strains) is expressed in a linear factor based on the value of the load and the geometry of the structure. This multiplier is known as the stress intensity factor (SIF).

Values of the stress intensity factor can be determined in a variety of ways which will be described later. These factors are tabulated in handbooks (such as Tada et al., [13]) for a wide

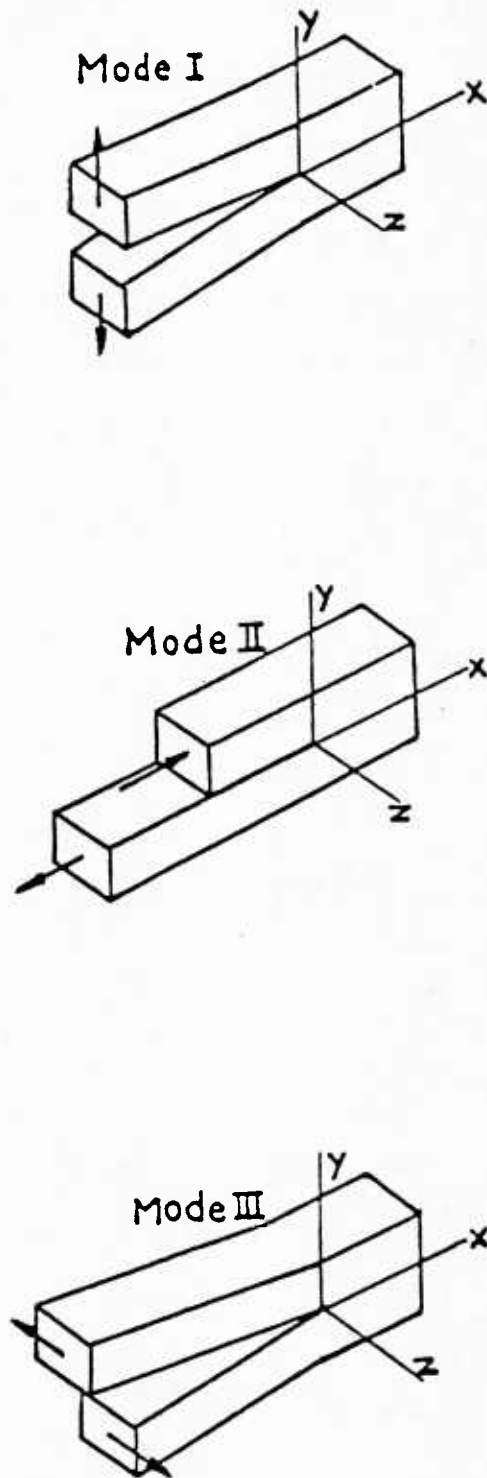


Figure 2.2 The Basic Modes of Crack Surface Displacement

range of loading configurations and geometries. The following section applies the stress intensity factor approach to the cracked test specimen used in this work.

2.1.3.1 The Case Under Study: Mode I.

In this study tests were done on thin strips under tensile load. The situation is one of plane stress in Mode I. Using the notation in Figure 2.3, Tada et al. [13] present the stress field for this condition as follows:

$$\sigma_x = \frac{K_I}{(2\pi\rho)^{\frac{1}{2}}} \cos \frac{\theta}{2} \left[1 - \sin \frac{\theta}{2} \sin \frac{3\theta}{2} \right] \quad (2-3a)$$

$$\sigma_y = \frac{K_I}{(2\pi\rho)^{\frac{1}{2}}} \cos \frac{\theta}{2} \left[1 + \sin \frac{\theta}{2} \sin \frac{3\theta}{2} \right] \quad (2-3b)$$

$$\sigma_{xy} = \frac{K_I}{(2\pi\rho)^{\frac{1}{2}}} \sin \frac{\theta}{2} \cos \frac{\theta}{2} \cos \frac{3\theta}{2} \quad (2-3c)$$

$$\sigma_z = \sigma_{xz} = \sigma_{yz} = 0 \quad (2-3d)$$

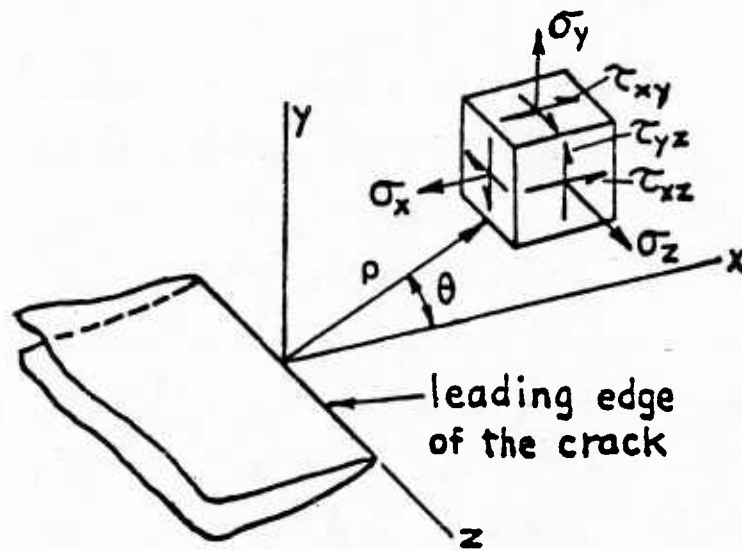


Figure 2.3 Coordinates at the Leading Edge of a Crack
(note: θ is contained in the x - y plane)

In these equations K_I is the stress intensity factor for Mode I. For Modes II and III the factors are K_{II} and K_{III} , respectively.

Furthermore, these expressions neglect higher order terms in ρ , e.g., $\rho^{1/2}$, $\rho^{3/2}$, etc. The solution then, is most accurate when ρ is small compared to the dimensions of the plate.

Tada et al.[13] describes the K 's physically as "the intensity of load transmittal through the crack tip region as caused by introducing the crack into the body of interest." Viewed in this manner, the stress intensity factor is valuable for comparing different cracks because it provides a measure of the severity a crack to a structure. The question of whether the stress intensity factor can be used to describe a nonsingular situation is subject to much controversy. This question is important to this study because herein it is necessary to compare the stresses around a sharp-tipped crack with the stresses around the blunted crack. Chapter 5 addresses this idea in more detail while the current discussion will continue to focus on the stress intensity factor approach in the conventional sense.

2.1.3.2 The Relationship to Stress Concentration Factors

A stress concentration factor approach does not offer the advantages of the stress intensity factor approach as just described. The latter approach is much more useful for studying cracks. Nevertheless, stress intensity factor concepts are closely related to the idea of stress concentration factors.

For an elliptical notch in a plate the stress concentration factor is the ratio of the maximum stress to the applied stress.

This parameter provides an easy way to compare the amount of concentration caused by different interruptions to stress flow. Basically, by considering a slender notch with a tip radius, r , one approaches the case of a crack in the limit as r goes to zero. By reducing the case of the ellipse to that of a crack, the stress concentration factor goes to infinity. Hence, this factor is not useful for characterizing different cracks because the factor will be infinity for all cracks. Also, the stress concentration factor says nothing about the stress field surrounding the crack tip. Only the condition at the point of maximum stress is described. On the other hand, a stress intensity factor approach characterizes the entire stress field surrounding a crack tip.

The main principle of this method asserts that the behavior of a crack can be described by the stress field around the tip. Furthermore, the method's primary advantage lies in the characterization of this stress field by a single parameter, K . The problem thus reduces to one of determining K , the stress intensity factor.

2.1.3.3 Determining Stress Intensity Factors

Both theoretical and experimental methods are used to determine stress intensity factors. Cartwright and Rooke [14] give an excellent review of the ways in which K 's are found.

Of the wide range of theoretical methods of computing stress intensity factors, this study considers three in particular. These are analytical solutions, stress concentration solutions, and finite element analyses. Other methods are available such as boundary collocation, conformal mapping, Green's functions,

integral transforms and dislocation models, force-displacement matching, and alternating methods. More on these is available in Reference 14. Each of these individual methods is especially useful in solving several different classes of problems having similar geometries.

Again, analytical, stress concentration, and finite element solutions are used to determine K 's in this work. The analytical method seeks to solve the equations of elasticity and satisfy the boundary conditions exactly. Two forms of elasticity solutions have been proposed in terms of Airy's stress functions. These are the Westergaard stress function and the complex stress functions of Mushkelishvili.

While these methods provide a convenient expression for K , the number of configurations which can be solved in this manner is limited. Fortunately, a solution does exist for a finite width strip in tension containing a notch in one side.

Another way to obtain stress intensity factors is from stress concentration factors. A relationship between stress intensity factors and stress concentration factors is developed in Chapter 5. Stress concentration factors are available for a wide variety of situations and hence the ability to convert them to stress intensity factors is valuable.

The use of finite element analysis to determine stress intensity factors can be approached in several ways depending on the problem at hand. These approaches can be generalized into three groups: 1) directly computing K 's, 2) indirectly computing K 's from changes in energy, and 3) utilizing special crack tip elements. The finite element stress analysis done in this work, however, does not use these methods. Instead, finite elements are used to determine the stress concentration factors from which the stress intensity factors are in turn obtained.

2.1.3.4 Critical Stress Intensity Factors

Any discussion of stress intensity factors should mention the ability of this approach to describe the conditions under which a crack propagates. In such a critical crack situation the crack penetrates further into the structure. Researchers in fracture mechanics have shown a relationship to exist between the strain energy release rate and the stress intensity factor. From the discussion of energy concepts in fracture earlier in this chapter, a crack propagates if a critical strain energy release rate is reached. Together, these two points imply that the occurrence of fracture may be expressed by a critical stress field around a crack or notch, or, in other words, a critical stress intensity factor which is a property of the material. Thus, a value of K_{cr} is defined as the critical stress intensity factor and is associated with a critical energy or force necessary to drive a crack forward.

In Mode I the critical stress intensity factor K_{Ic} is also referred to as the fracture toughness. Since Mode I is generally

the most critical crack situation, the fracture mechanics literature deals with this Mode almost exclusively as will the following discussion.

Values of K_{Ic} have been determined and are tabulated for a wide range of materials under standard ASTM plane strain conditions. For Ti-6Al-4V the fracture toughness is $74.6 \text{ MPa}\sqrt{\text{m}}$ ($68 \text{ ksi}\sqrt{\text{in}}$) [15]. These values can be used to predict adequately the occurrence of fracture in configurations which are sufficiently close to a state of plane strain.

When the conditions of plane strain are not met, K_{Ic} can no longer characterize the incidence of fracture as a material property. Tests have shown the fracture toughness to be strongly dependent on plate thickness. Only for sufficient thickness, can a specific value of the parameter be associated with the material. Therefore, in the current work the tabulated values of fracture toughness do not apply because the situation is one of plane stress.

Boresi et al. [6] note that in a plane stress case, the actual fracture load will typically be several times that which is predicted with K_{Ic} . Large amounts of yielding will occur around the crack zone prior to fracture. This behavior was observed as part of this study in comparison of experimental results and analytical calculations. Further discussion of this is given in Chapter 5.

In the fracture analysis of real structures the value of K must be accurately determined using one of the methods described

earlier. These techniques must account for many factors such as loading, geometry, corrosion environment, and fatigue. Crack initiation in a notch or the extension of an existing crack in a structure can then be predicted satisfactorily by how close this parameter, K , approaches its critical value for the mode, material, and stress state in question.

2.2 MAGNETOMECHANICS THEORY

The fundamental physical concepts involved in magnetomechanical problems are first briefly discussed in general. Following this presentation is a more specialized treatment of the theory's application to thin conducting plates in terms of a stream function formulation.

2.2.1 BASIC CONCEPTS

Analysis of conducting structures subject to magnetic fields is complicated because the effects which must be studied involve more than one discipline. The major areas concerned include electromagnetics, continuum mechanics, and thermodynamics. Only a brief discussion of the development behind the necessary formulations is presented rather than a detailed derivation of the

governing equations. A full account of this derivation can be found in Reference 16.

From each of the three disciplines involved one has a set of equations and boundary conditions. The equations from electromagnetic theory are Maxwell's equations, the Biot-Savart Law, the Lorentz body force equation, and Ohm's Law. From continuum mechanics we have the equilibrium, compatibility, and constitutive equations. Thermodynamic effects are governed by energy balance equations and conductivity relationships.

Yuan et al.[17] present a chart which outlines some of the couplings between the fields associated with each of these three disciplines. This chart is reproduced in Figure 2.4.

These equations are coupled in several ways. Mechanical equilibrium and temperature effects are related through the Duhamel-Neumann Law. This relationship introduces an $\alpha \Delta T$ term into the mechanical constitutive equations (where α is the coefficient of thermal expansion). The electromagnetic and thermal conditions are coupled through the Joule heating effects.

The interdependence of the mechanical equilibrium and electromagnetic field is the most complicated because several relationships are involved. One has the Lorentz force created when a magnetic field acts on moving charges. One also has Faraday's Law which implies that currents will be induced when the magnetic field is changed by the displacement of the structure.

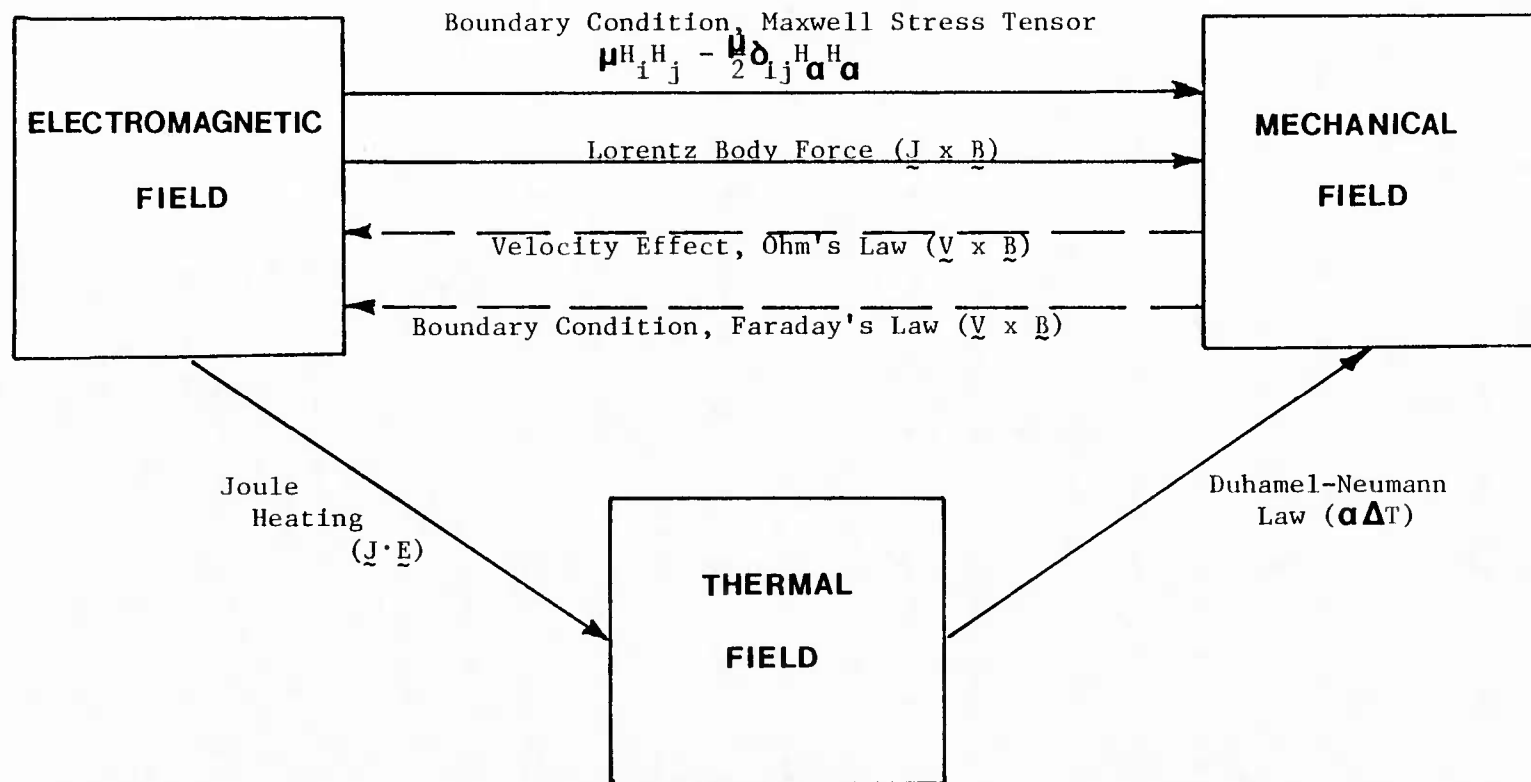


Figure 2.4 A Schematic of One Form of Magnetothermomechanical Coupling
 (\underline{E} = electric field, \underline{J} = electric current, \underline{B} = magnetic flux,
 \underline{V} = velocity field, μ = magnetic permeability, α = coefficient
 of thermal expansion, T = change in temperature from reference
 temperature, \underline{H} = magnetic intensity.)

Together, these last two effects can be thought of in terms of a negative stiffness. In other words, further deformations cause the loads on the structure to increase.

Another coupling effect also exists between the mechanical and electromagnetic fields. The motion of the plate in the magnetic field will induce currents within the plate itself. This is indicated mathematically by the velocity term in Ohm's Law. However, for the type of problems being considered in this study, this effect is assumed to be negligible.

Physically, the overall interaction can be described for the specific case of a plate as follows. Electric currents (known as eddy currents) are induced in the plate by the magnetic field. The eddy currents generate a further magnetic field which opposes the external one. Both of these magnetic fields interact with currents already present in the structure to cause magnetic forces. These forces deform the structure, which in turn changes the magnetic field distribution, and hence the coupled interaction between these effects is evidenced. Some specific applications of this theory for thin plates is given in the next section.

2.2.2 APPLICATION OF THE THEORY TO PLATE PROBLEMS

This application of the theory concerns the basic problem of an elastic conducting plate in a magnetic field. An important aspect of this type of problem is that the magnetic fields exist both in the plate and in the surrounding free space. Hence, the problem is three dimensional. Techniques used to solve these problems are discussed first, followed by a treatment of the types of solution available. A list of simplifying assumptions is then presented.

2.2.2.1 Solution Techniques

The coupled nature of problems of this type and the complex equations governing them make analytical solutions obtainable only for simple cases. Subsequently, these problems have usually been solved using an uncoupled approach where one performs discrete calculations for magnetic effects and then computes thermal and mechanical response based on these results.

The situation is further complicated when time-dependent magnetic fields are present. In this case a numerical approach is necessary even for the uncoupled problem. With this in mind the computer programs EDDY1 and EDDY2 were developed to analyze thin conducting plates subjected to time-varying magnetic fields. These programs use a finite element approach to compute the eddy currents and then determine the induced temperatures and magnetic pressures based on those results.

Two different techniques of formulating the uncoupled electromagnetic problem have been advocated by previous

researchers. One method obtains the solution in terms of magnetic vector potential, \underline{A} . The vector potential is defined by:

$$\underline{B} = \nabla \times \underline{A} \quad (2-4)$$

The governing equations are then written throughout the entire 3D space in terms of this value. Other studies have developed finite element formulations based on this technique. Since EDDY1 and EDDY2 are not based on this method it is not discussed further.

The second method introduces a stream function, Ψ , which applies to the one- or two-dimensional plate only. A formulation based on this function is used in EDDY1 and EDDY2. A finite element model is then used to determine the value of the stream function throughout the plate. The development based on the stream function formulation is used throughout this report. The formulation of the uncoupled electromagnetic problem based on the stream function will be briefly described in section 2.2.3. The temperature and pressure calculations based on the electromagnetic solution are also noted. A more detailed development of the formulation will be given in a later chapter when the extension to transport currents is discussed. Yuan [16] gives additional treatment of this theory as it is used in the original versions of the programs.

2.2.2.2 Types of Solution

By considering different frequencies in these problems, the possibility for two different types of solution is evident. These are referred to as the local and nonlocal approaches. The programs EDDY1 and EDDY2 perform analyses based on both solution techniques.

A local approach may be used when the frequency of the magnetic field or transport current is low. This allows simplification of the formulation to be made and the aim is then to satisfy the governing differential equations and boundary conditions directly. The region considered in the problem then is the full surrounding space, theoretically extending to an infinite distance.

For high frequencies on the other hand, a nonlocal solution is used. This approach reformulates the problem using integrals so that the domain of the problem is reduced to the conductor itself.

2.2.2.3 Assumptions

Several important assumptions used in this formulation should be made clear [16],[17].

1. The material is assumed to be a good conductor which is not magnetizable or polarizable. This assumption has implications

on the atomic level. Charge dipoles exist in the material due to the "spin" property of the atoms. Consideration will be given only to materials in which the dipoles do not reorient themselves under an external field to create additional field intensity.

2. Material properties are assumed to be independent of temperature.
3. Eddy current density across the thickness of the plate is assumed to be constant.
4. The electromagnetic relationships are considered in their quasistatic form. As noted by Moon [18], this observation is valid, because the wavelengths associated with frequencies in these problems are much longer than conventional structure dimensions. This manifests itself in allowing the velocity term of Ohm's Law to be dropped as was mentioned earlier.
5. Eddy currents are assumed to flow parallel to midsurface of the plate.
6. The normal component of the induced magnetic field does not vary across the thickness of the plate.

2.2.3 EDDY CURRENT ANALYSIS IN PLATES USING A STREAM FUNCTION SOLUTION

The previous section discussed the theoretical aspects of analyzing thin conducting plates subject to magnetic fields. The solution method using stream functions was noted. This chapter defines the stream function and develops the governing equations necessary to solve these problems.

First, some definitions pertaining to the following discussion are given here:

E = Electric field

B = Magnetic field

J = current density

σ = material conductivity

μ = magnetic permeability

w = frequency of the applied field

2.2.3.1 Definition of the Stream Function

The stream function is defined in terms of the current. Following the assumptions stated earlier, the current will be considered uniform over the thickness of the plate. In the following development $I = hJ$ is used as the current density, where h is the plate thickness and I is current per unit width.

First, it will be helpful to define some other terms used in the discussion to follow. A cartesian coordinate system, (x, y, z) , is used along with a set of orthogonal coordinates, (α, β) . The

latter coordinate system is coincident with the midsurface of the plate. The relationship between the two coordinates is given by:

$$x = x(\alpha, \beta) \quad y = y(\alpha, \beta) \quad z = z(\alpha, \beta) \quad (2-5)$$

The unit vectors in the α and β directions are then defined as:

$$\underline{e}_\alpha = \begin{Bmatrix} \frac{1}{f} & \frac{\partial x}{\partial \alpha} \\ \frac{1}{f} & \frac{\partial y}{\partial \alpha} \\ \frac{1}{f} & \frac{\partial z}{\partial \alpha} \end{Bmatrix} \quad \underline{e}_\beta = \begin{Bmatrix} \frac{1}{g} & \frac{\partial x}{\partial \beta} \\ \frac{1}{g} & \frac{\partial y}{\partial \beta} \\ \frac{1}{g} & \frac{\partial z}{\partial \beta} \end{Bmatrix} \quad (2-6)$$

in which f and g are:

$$f^2 = \left(\frac{\partial x}{\partial \alpha} \right)^2 + \left(\frac{\partial y}{\partial \alpha} \right)^2 + \left(\frac{\partial z}{\partial \alpha} \right)^2 \quad (2-7)$$

$$g^2 = \left(\frac{\partial x}{\partial \beta} \right)^2 + \left(\frac{\partial y}{\partial \beta} \right)^2 + \left(\frac{\partial z}{\partial \beta} \right)^2 \quad (2-8)$$

The current density vector, I , can then be expressed as:

$$\underline{I} = I^\alpha(\alpha, \beta) \underline{e}_\alpha + I^\beta(\alpha, \beta) \underline{e}_\beta \quad (2-9)$$

Based on this the stream function, Ψ , is defined in terms of the current density components:

$$I^\alpha = \frac{1}{g} \frac{\partial \Psi}{\partial \beta} \quad I^\beta = -\frac{1}{f} \frac{\partial \Psi}{\partial \alpha} \quad (2-10)$$

One physical significance of the stream function is that the current as travels along lines of constant stream function.

2.2.3.2 Basic Governing Equation

The basic governing equation for Ψ comes from Faraday's Law of Induction: $\text{curl } \mathbf{E} = -\partial \mathbf{B} / \partial t$. The magnetic field can be thought of as the sum of the applied field, B^O , and the induced field, B^I . Furthermore, by substituting in for \mathbf{E} using Ohm's Law ($\mathbf{E} = \mathbf{I} / h \sigma$) and using the definition of Ψ , one obtains the governing equation in vector form. For the case of a flat plate this equation is:

$$\nabla^2 \Psi = \sigma h \frac{\partial}{\partial t} (B_Z^O + B_Z^I) \quad (2-11).$$

This form considers only the in-plane current and assumes the mid-plane of the plate is aligned with the x-y plane.

In one dimension this problem simplifies to the case of an infinite strip. The program EDDY1 analyzes this problem.

2.2.3.3 The Induced Field Term

The induced magnetic field can be determined from the Biot Savart Law. Reference 19 gives the induced field at the midplane of the plate ($z=0$) as:

$$B_Z^I(X, Y, 0) = \frac{\mu}{h} \Psi - \frac{\mu}{4\pi} \int_A \frac{\Psi(X', Y') dA}{[(X - X')^2 + (Y - Y')^2 + (h^2/4)]^{3/2}} \quad (2-12)$$

in which A is the surface area of the top or bottom face. The point at which B^I is computed is given by the x and y coordinates. The x' and y' coordinates reference the current element which is contributing and it is over these coordinates that the integration is performed.

In this formula ψ is assumed constant through the thickness and zero on the lateral boundaries of the plate as is appropriate for the eddy current problem. When ψ is nonzero on the boundaries of the plate in connection with the transport current problem, this expression will involve additional terms which represent the effect of the edges on the induced magnetic field. The development of these terms and their implication is the subject of Chapter 3.

2.2.3.4 Governing Equation for the Steady State Problem

By considering the case of a harmonically applied magnetic field, $B^O = B^O e^{i\omega t}/2$, the currents are then also harmonic and the problem becomes steady state.

The previous equations are now combined to obtain one differential equation for substitution into the Galerkin criterion. First, substitute B^O (from above) and B^I (from eqn. 2-12) into the governing equation for ψ (eqn. 2-11). Furthermore, one can simplify and generalize the formulation by nondimensionalizing with respect to the half thickness, $h/2$, as follows:

$$\psi = \frac{hB}{2\mu} \phi e^{i\omega t} ; \quad x = \frac{2X}{h} ; \quad y = \frac{2Y}{h} ;$$

$$\xi = \frac{2X'}{h} ; \quad \eta = \frac{2Y'}{h} \quad (2-13)$$

After substitution the equation is in terms of the non-dimensionalized stream function Φ :

$$\nabla^2 \phi - i2\pi R\phi + iR \int_A \frac{\phi(\xi, \eta) d\xi d\eta}{[(x - \xi)^2 + (y - \eta)^2 + 1]^{3/2}} = i2\pi R\theta(x, y) \quad (2-14)$$

in which $R = \mu\sigma\omega h^2/8\pi$ = magnetic Reynold's number.

This equation can be thought of as an equilibrium between the applied magnetic field on the right hand side and the induced magnetic field and eddy currents on the left hand side. On the left hand side, the first term is associated with the eddy currents induced by the externally applied field. The second and third term are related to the induced magnetic field.

It is instructive at this point to examine equation (2-14) further and note different categories of problems which may arise. The previous section mentioned the theoretical aspects of the local and nonlocal problems. This section examines their meaning in more detail and addresses the implications for solution in each of these cases. Furthermore, a third type of solution, the "image" solution, will be introduced. While the local and nonlocal problems have low and medium Reynold's numbers respectively, the image solution is for very high Reynold's numbers.

The first case to be discussed is the local problem. In this case the frequency of the applied field is small, and hence the induced magnetic field is weak. Therefore, the eddy currents can be considered as due solely to the applied field acting at the point in question. Hence, the term "local" solution is used. This local condition is exploited in the solution process as follows. In the equations, the frequency is included as part of the magnetic Reynold's number. The Reynold's number will be small in this case and hence this allows the second and third terms on the left hand side of equation (2-14) to be dropped. The local form of the governing equation is then:

$$\nabla^2 \phi = i2\pi R\theta(x, y) \quad (2-15)$$

This is a powerful simplification. The resulting coefficient matrix is then symetric, banded, and requires much less computer storage and time for solution.

In the second case the frequency is in the middle range of values. This solution is generally refered to as the "nonlocal solution". Since the Reynold's number is not small, the second and third terms must be included. These latter terms couple the eddy currents with the induced magnetic field. More specifically, the second term is tied to the induced field at the point being considered while the third term (the integral term) is tied to the effect of the induced field from the rest of the plate. The eddy currents influence the induced field as well.

The third case involves a relatively high frequency and hence a relatively high Reynold's number. On the left hand side of the equation, the second and third terms now dominate. Physically, this means the induced magnetic field is strong and hence one can think of an "image" which creates the opposing field. The image would be a reflection of the configuration which sets up the externally applied field but would lie on the other side of the plate. The term "image solution" is used to refer to this type of situation.

CHAPTER 3

FINITE ELEMENT ANALYSIS OF EDDY CURRENTS AND TRANSPORT CURRENTS

The subject of this chapter is the analysis of electric currents in thin conducting plates using finite element analysis. In particular, the chapter focuses on the extension of the existing programs, EDDY1 AND EDDY2, to include the ability to handle transport currents as well as induced currents.

As noted in the introduction, the new formulation applies to both the one- and two-dimensional programs, EDDY1 and EDDY2. The actual changes are implemented only in EDDY1, however.

3.1 EXISTING PROGRAMS AND MOTIVATION FOR FURTHER DEVELOPMENT

This section describes the finite element method approach for the problem developed in the last chapter and then describes the computer programs EDDY1 and EDDY2 that were developed based on this scheme.

3.1.1 FINITE ELEMENT MODELING OF THE STREAM FUNCTION

The previous chapter developed the integro-differential equation (2-14) which governs the flow of eddy currents in thin plated subject to time varying magnetic fields. A stream function, Ψ , is defined in terms of the current, and the equation is obtained in terms of that parameter. The equation is put in steady state form, and the problem then remains to determine the distribution of the stream function over the plate. Finite element analysis is used to accomplish this final step in the solution process.

For the one-dimensional case the steady state nondimensional governing equation is a simplification of equation (2-14).

$$\frac{d^2\phi}{dx^2} - iR\phi + i \frac{R}{2\pi} \int_{-\ell}^{\ell} \frac{\phi}{(x - \xi)^2 + \frac{1}{4}} d\xi = iRB(x) \quad (3-1)$$

in which ℓ is the half width of the plate, and $R = \mu\sigma wh^2$.

The following finite element models are used to model the nondimensional stream function over each element and over the entire plate respectively [16].

$$\phi^E = \sum_{K=1}^2 N_K^E \phi_K \quad \phi = \sum_{K=1}^G M_K \phi_K \quad (3-2)$$

in which M_k are the global interpolation functions generated from the local element shape functions, N_k , and ϕ_k are the nodal

values of the nondimensional stream function. In the second expression G is the total number of nodes in the structure. Equation (3-1) and the above models are substituted into the Galerkin criterion from which the following set of finite element equations results:

$$-\sum_{K=1}^2 S_{JK}^E \phi_K - i \sum_{K=1}^2 P_{JK}^E \phi_K + i \sum_{K=1}^G Q_{JK}^E \phi_K = i R_j^E ; \quad j = 1(1)n \quad (3-3)$$

or

$$(-[S] - i[P] + i[G]) \{\phi\} = i\{R\} \quad (3-4)$$

in which $[S]$ and $[P]$ are banded, symmetric $n \times n$ matrices, $[Q]$ is a nonsymmetric, full $n \times n$ matrix, $\{\phi\}$ is an $n \times 1$ vector of nodal stream function values, and $\{R\}$ is an $n \times 1$ vector containing loading terms. The integral expressions for these matrices are:

$$S_{JK}^E = \int_E \frac{dN_j^E}{dx} \frac{dN_K^E}{dx} dx ; \quad P_{JK}^E = R \int_E N_j^E N_K^E dx \quad (3-5)$$

$$Q_{JK}^E = \frac{R}{2\pi} \int_0^\ell M_K(\xi) W_j^E(\xi) d\xi ; \quad R_j^E = R \int_E N_j^E B dx$$

in which the weighting function for the integral term is:

$$W_j^E(\xi) = \int_E \frac{N_j^E(x)}{(\xi - x)^2 + \frac{1}{4}} dx \quad (3-6)$$

These matrix equations form the basis of EDDY1. A similar development in two dimensions is used for EDDY2.

3.1.2 A GENERAL OVERVIEW OF THE PROGRAMS: EDDY1 AND EDDY2

The computer programs, EDDY1 and EDDY2, use the finite element approach just described to calculate eddy currents in thin plates subjected to time varying magnetic fields.

In the finite element equations the magnetic field, B , is analogous to the load on a plate in structural mechanics. Hence, the B term is frequently referred to as the loading.

Furthermore, in EDDY1 and EDDY2 the source of the applied magnetic field can be one of several types. EDDY1 can accommodate uniform fields and infinite filaments parallel to the long direction of the plate. Following an improvement made by Hara (Ref. 20), EDDY2 is capable of handling uniform magnetic fields, line currents, and circular current loops in any orientation as sources of the magnetic field.

Also required as input are the coordinates of several nodes in the structure from which the complete set of nodes and their locations are generated. The material properties are specified in

a magnetic Reynold's number. In EDDY2 this Reynold's number is defined as $R = \mu\sigma w h^2 / 8\pi$, where w = the frequency of the applied field. The Reynold's number is defined as $R = \mu\sigma w h^2$ in EDDY1 because of the difference in nondimensionalization. EDDY1 and EDDY2 are nondimensionalized with respect to the half thickness and thickness respectively.

A temperature constant is also specified which contains the material properties related to thermal behavior such as specific heat, conductivity, and density. This value is used as a direct multiplier in the temperature calculation and therefore is important for comparing the temperature change of different materials under the same loading.

The programs also have the capability of specifying multiple load cases and multiple parameter sets. The latter option is useful in doing parameter studies. Another valuable feature of the programs is their connection to postprocessors which produces graphical displays of the results. This facilitates interpretation of the results.

The programs perform the three different types of solution that were discussed in the previous chapter. These solutions (local, nonlocal, and image) are all computed in a single program execution. This allows one to observe the range of Reynold's numbers for which certain of these solutions are valid. Thus, one can obtain insight of which frequencies create strong induced fields and which do not.

As discussed in the introduction, the motivation behind modifying the original programs lies in their inability to solve cases in which a transport current exists. To implement this capability it was necessary to alter the programs to admit the possibility of non-zero boundary conditions. In their original versions, EDDY1 and EDDY2 automatically set the value of the stream function to zero on the edges of the plate. Furthermore, the equation for the induced field (2-12) used in the formulation assumes zero edge values of the stream function. The requirements for nonzero boundary conditions are discussed in more detail in section 3.3.

3.2 FORMULATION OF THE TRANSPORT CURRENT PROBLEM

The basic formulation and capabilities of the original versions of EDDY1 and EDDY2 have been given. This section will now develop the formulation of the same problem in one- and two-dimensions, but with the addition of an applied transport current. The detailed development follows very closely that given in Chapter 2. Therefore, the fundamental steps are reviewed, and the significant differences in the development are emphasized as they occur.

This section presents the formulation of the problem while a full treatment of the differences between this and the original formulation is reserved until the following section.

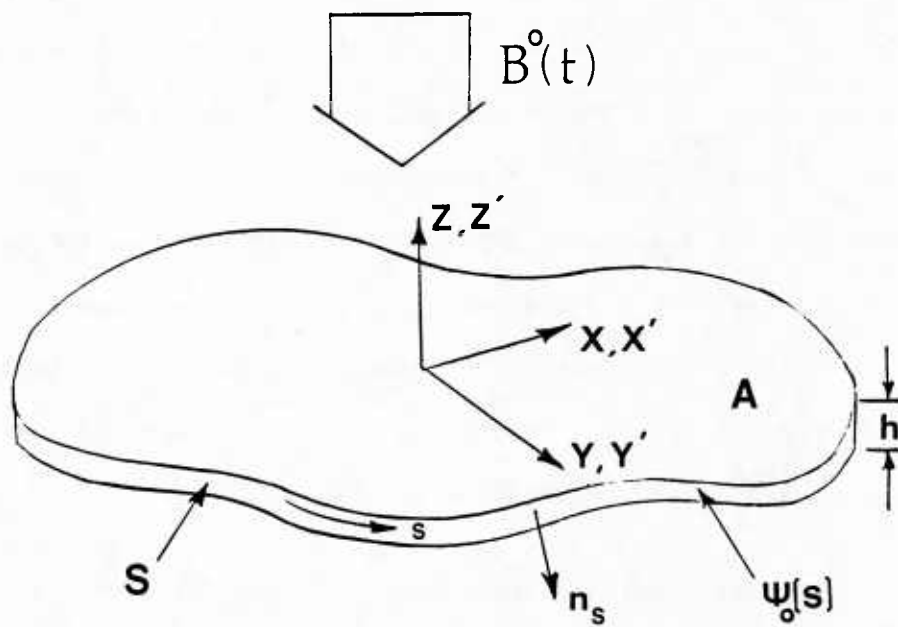
The general two-dimensional case is derived first. This formulation is then specialized to the case of a rectangular plate and then for the case of an infinite strip.

3.2.1 THE GENERAL TWO-DIMENSIONAL CASE

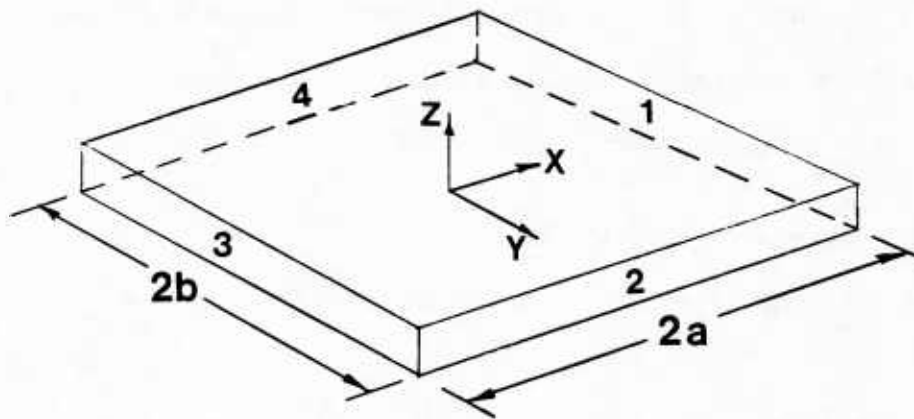
In the following development is for a thin conducting plate of arbitrary shape as shown in Figure 3.1(a). The plate is subjected to an applied magnetic field, B^0 , and a transport current. The transport current loading is specified by the derivative of the stream function along the plate edge, $I = \partial \psi_0(s) / \partial s$. In this expression I is the transport current perpendicular to the edge and ψ_0 is the edge stream function distribution in terms of the edge tangent coordinate, s .

As before, the fundamental equation begins with Faraday's Law of Induction. Furthermore, the stream function is defined in the manner of section 2.2.3.1. The next step is substitution of this definition, Ohm's Law, and the applied and induced field expressions into Faraday's Law. Simplifying this for the midplane of a plate, results in equation (2-11) as in the previous chapter.

$$\nabla^2 \psi = \sigma h \frac{\partial}{\partial t} (B_z^0 + B_z^I) \quad (3-7)$$



(a) Two-Dimensional Plate of Arbitrary Shape



(b) Two-Dimensional Rectangular Plate

Figure 3.1 Two-Dimensional Plate Configurations

Up to this point the development has been the same as in Chapter 2, and, likewise, the assumptions used in that chapter are applicable here. Now, however, the development departs from the previous description. With nonzero values of the stream function required on the edge to apply a transport current, the previous formula used for the induced field no longer applies. However, in the following discussion (in which the induced field expression with nonzero boundary conditions is derived) one can see the direct similarity between the two cases.

The important difference between the two cases is the existence of "edge terms" in the expression admitting nonzero boundary values. These "edge terms" arise out of the integration of the stream function along the plate edge. Section 3.3.3.1 addresses the significance of these terms.

In section 2.2.3.3 the formula for the induced field is taken directly from reference 16. The induced field expression for the problem at hand is derived in a concise manner below.

The Biot-Savart Law is the basis of the B equation for the case of both zero and nonzero boundary conditions. From Biot-Savart [24] one has the contribution, dB , to the total field at the point in question due to an infinitesimal current segment dl :

$$dB = \frac{\mu i}{4\pi} \frac{d\vec{l} \times \vec{r}}{r^3} \quad (3-8)$$

In this expression r is the perpendicular vector between the current segment dl and the point at which dB is being computed. The current in the segment dl is i and μ is the magnetic permeability of the material inbetween.

To obtain the total induced field at the point in question, the above expression is integrated over the entire current distribution. For the case of a plate of volume V and current distribution $I(r')$, the integral is:

$$\underline{B}^I(r) = \frac{\mu}{4\pi h} \int_V \frac{\underline{I}(r') \times (r - r')}{|r - r'|^3} dV' \quad (3-9)$$

In this derivation it is important to keep in mind that the primed coordinates refer to the current distribution while the unprimed coordinates refer to the point at which the field is being computed.

The notation $R = r - r'$ is now introduced. From vector calculus the following identity is applied to the integrand of equation (3-9):

$$\frac{\underline{I} \times \underline{R}}{R^3} = -\underline{I} \times \nabla \left(\frac{1}{R} \right) \quad (3-10)$$

Using the definition of the stream function for the current, one obtains the equation in its expanded vector form. For substitution in equation (3-7) only the Z component of B^I is necessary which leaves the following expression:

$$B_z^I(r) = \frac{\mu}{4\pi h} \int_V \left[\frac{\partial \psi}{\partial X'} \frac{\partial}{\partial X'} \left(\frac{1}{R} \right) + \frac{\partial \psi}{\partial Y'} \frac{\partial}{\partial Y'} \left(\frac{1}{R} \right) \right] dV' \quad (3-11)$$

The corresponding derivative in the above expression with respect to Z' is now both added and subtracted. This enables equation (3-11) to be rewritten:

$$B_z^I(r) = \frac{\mu}{4\pi h} \int_V \left[\nabla_1 \psi \cdot \nabla_1 \frac{1}{R} - \frac{\partial \psi}{\partial Z'} \frac{\partial}{\partial Z'} \left(\frac{1}{R} \right) \right] dV' \quad (3-12)$$

in which ∇_1 is the gradient operator in primed coordinates.

The second term in the integrand will be zero following the assumption of uniform ψ over the thickness.

In the next step the remaining term of the integrand is expanded and several associated terms are then simultaneously added and subtracted. After regrouping and simplifying back into vector form:

$$B_z^I(r) = \frac{\mu}{4\pi h} \int_V \left[\nabla_1 \cdot \left(\psi \nabla_1 \frac{1}{R} \right) - \psi \nabla_1^2 \frac{1}{R} \right] dV' \quad (3-13)$$

Integration by parts is now performed on the second term in the integrand. The singularity involved is overcome using an identity containing delta functions given by Jackson [21].

The divergence theorem is now applied to the first term to transform it from an integral over the volume to an integral over the surface area of the plate. From these two steps the resulting expression is:

$$B_z^I(r) = \frac{\mu\psi}{h} + \frac{\mu}{4\pi h} \int_{S_T} \mathbf{n} \cdot \left[\psi \nabla_1 \frac{1}{|R|} \right] dS_T' \quad (3-14)$$

in which S_T is the total surface area of the plate, and \mathbf{n} is the unit vector normal to the surface.

The surface integral is now divided into an integral over the top and bottom faces of the plate and an integral over the edge surface. Denoting the surface area of the top or bottom face as A , and the edge surface as S , the expression is:

$$B_z^I(r) = \frac{\mu\psi}{h} + \frac{\mu}{4\pi} \int_A \frac{\psi(X', Y')}{[(X - X')^2 + (Y - Y')^2 + (h^2/4)]^{3/2}} dA' \\ + \frac{\mu}{4\pi h} \int_S \mathbf{n}_s \cdot \left[\psi \nabla_1 \frac{1}{|R|} \right] dS' \quad (3-15)$$

in which \mathbf{n}_s is the unit vector normal to the edge surface. One can observe that the first two terms in the above expression are

identical to equation (2-12). It is the third term that involves the transport current effect.

A further simplification of the expression can be made by integrating over Z' . This step only involves the edge surface integral. The result is a line integral around the edge of the plate for the third term.

The final step in the development of the governing equation for the general two-dimensional problem is differentiation of the expression for B^I with respect to time and substitution into equation (3-7). With C to indicate the line integral in the third term, the resulting expression is

$$\begin{aligned} \nabla^2 \psi - \sigma \mu \frac{\partial \psi}{\partial t} + \frac{\sigma \mu h}{4\pi} \int_A \frac{\frac{\partial \psi}{\partial t}}{[(X - X')^2 + (Y - Y')^2 + (h^2/4)]^{3/2}} dA' &= \sigma h \frac{\partial B_z^0}{\partial t} \\ + \frac{\sigma \mu h}{4\pi} \oint_C \frac{(\frac{\partial \psi}{\partial t})[n_x(X - X') + n_y(Y - Y')]}{[(X - X')^2 + (Y - Y')^2][(X - X')^2 + (Y - Y')^2 + (h^2/4)]^{1/2}} dC' & \end{aligned}$$

(3-16)

In the following two sections this equation is modified for the case of a rectangular plate and an infinite one-dimensional strip.

3.2.2 GOVERNING EQUATION FOR A RECTANGULAR PLATE

The notation for the rectangular plate is shown in Figure 3.1(b).

Simplification of equation (3-16) for this case involves the last term only. Based on the geometry the function n_x takes on the value 1 at $X=a$ and -1 at $X=-a$. Likewise, n_y is 1 on $Y=b$ and -1 on $Y=-b$.

This implies a division of the final term into four separate integrals, one on each edge face of the plate. The expression is then written as:

$$\begin{aligned}
 \nabla^2 \psi - \sigma \mu \frac{\partial \psi}{\partial t} + \frac{\sigma \mu h}{4\pi} \int_A \frac{\partial \psi(X', Y') / \partial t}{[(X - X')^2 + (Y - Y')^2 + (h^2/4)]^{3/2}} dA' &= \partial h \frac{\partial B_z^0}{\partial t} \\
 + \frac{\sigma \mu h}{4\pi} \int_{-b}^b \left\{ \frac{[\partial \psi_1(Y') / \partial t] (X - a)}{[(X - a)^2 + (Y - Y')^2][(X + a)^2 + (Y - Y')^2 + (h^2/4)]^{1/2}} \right. \\
 - \left. \frac{[\partial \psi_3(Y') / \partial t] (X + a)}{[(X + a)^2 + (Y - Y')^2][(X + a)^2 + (Y - Y')^2 + (h^2/4)]^{1/2}} \right\} dY' \\
 + \frac{\sigma \mu h}{4\pi} \int_{-a}^a \left\{ \frac{[\partial \psi_2(X') / \partial t] (Y - b)}{[(X - X')^2 + (Y - b)^2][(X - X')^2 + (Y - b)^2 + (h^2/4)]^{1/2}} \right. \\
 - \left. \frac{[\partial \psi_4(X') / \partial t] (Y + b)}{[(X - X')^2 + (Y + b)^2][(X - X')^2 + (Y + b)^2 + (h^2/4)]^{1/2}} \right\} dX'
 \end{aligned}
 \tag{3-17}$$

in which ψ_i denotes the specified steam function distribution along side i .

3.2.3 GOVERNING EQUATION FOR A ONE-DIMENSIONAL STRIP

Figure 3.2 shows the notation used for this problem. The case of an infinite one-dimensional strip assumes that everything is constant in one dimension which is taken as the Y direction here. Hence, only a cross-section of the plate need be considered since the situation will be the same at any section.

Edges 2 and 4 on the rectangular plate in Figure 3.1(b) are now at an infinite distance away from the section under consideration. Equation (3-17) is now modified by allowing b to go to infinity in the last two terms. These terms go to zero in the limit as b goes to infinity. Physically, this makes sense because the influence of these faces will not be felt at the current section if they are large distance away.

Further simplification of the three remaining integral terms is possible by integrating over Y' from negative to positive infinity. The final expression is:

$$\begin{aligned} \frac{\partial^2 \psi}{\partial X^2} - \sigma \mu \frac{\partial \psi}{\partial t} + \frac{\sigma \mu h}{2\pi} \int_{-a}^a \frac{\partial \psi(X')/\partial t}{(X - X')^2 + (h^2/4)} dX' &= \sigma h \frac{\partial B_z^0}{\partial t} \\ &+ \frac{-\mu(\partial \psi_1/\partial t)}{\pi \sqrt{(X - a)^2 + (h^2/4)}} (\lambda_1 + (1/\lambda_1)(\tan^{-1}(1/\lambda_1) - \tan^{-1} \lambda_1 + (\pi/2))) \\ &+ \frac{-\mu(\partial \psi_3/\partial t)}{\pi \sqrt{(X + a)^2 + (h^2/4)}} (\lambda_3 + (1/\lambda_3)(\tan^{-1}(1/\lambda_3) - \tan^{-1} \lambda_3 + (\pi/2))) \end{aligned} \quad (3-18)$$

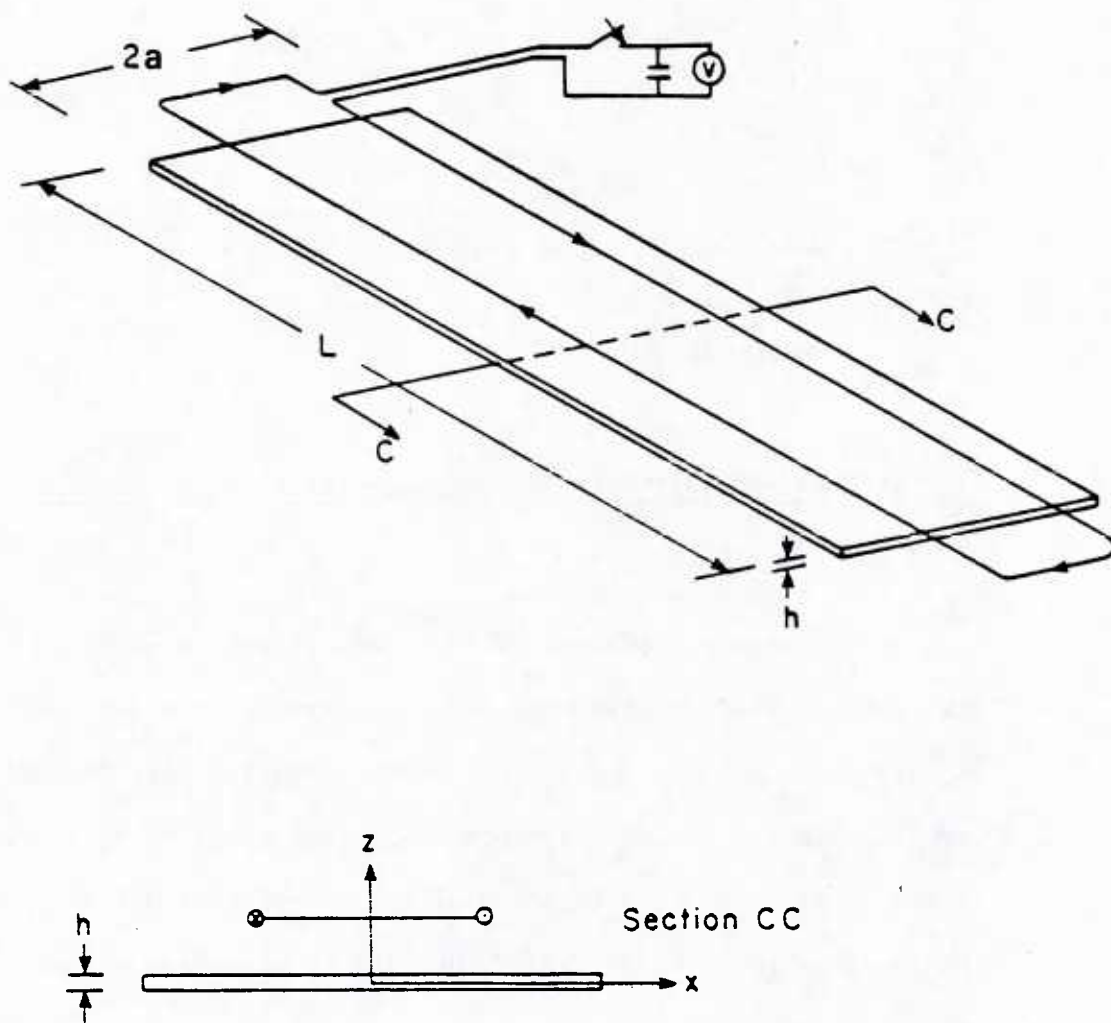


Figure 3.2 Infinite One-Dimensional Plate

in which:

$$\lambda_1^2 = 1 + \frac{4(X - a)}{h^2} \left[2(X - a) + \sqrt{4(X - a)^2 + h^2} \right] \quad (3-19)$$

$$\lambda_3^2 = 1 + \frac{4(X + a)}{h^2} \left[2(X + a) + \sqrt{4(X + a)^2 + h^2} \right] \quad (3-20)$$

3.3 IMPLEMENTING TRANSPORT CURRENT CAPABILITY IN THE 1D CASE

The necessary formulations for the one- and two-dimensional transport current problem have been developed in the last section. As noted earlier, the changes required to analyze this problem were implemented in the one-dimensional case only. Therefore, the following discussion is in terms of the one-dimensional problem. The required changes for the 2D case are an extension of the procedure described here.

Two major changes are required to admit transport currents in the programs. These two modifications correspond to changes in the boundary conditions and changes in the differential equation. First, to recognize nonzero boundary conditions the original finite element equations must be rearranged. Second, in the

differential equation, when a transport current exists, the additional terms not found in the original equation must be included. These aspects are treated separately in sections 3.3.2 and 3.3.3, respectively.

Before addressing the modifications above, the formulation of the 1D problem will be put in the nondimensional terms which are used in EDDY1.

3.3.1 THE NONDIMENSIONAL STEADY STATE FORMULATION OF THE 1D PROBLEM

Following the method of Yuan [15], the 1D problem is nondimensionalized with respect to the plate thickness, h , and put in its steady state form using the relationships:

$$x = \frac{X}{h}, \quad \xi = \frac{X'}{h}, \quad \ell = \frac{a}{h}, \quad \psi = \phi(x) I_0 e^{i\omega t} \quad (3-21)$$

$$B_z^0 = \frac{\mu}{h} B(x) I_0 e^{i\omega t}, \quad \psi_1 = C_1 I_0 e^{i\omega t}, \quad \psi_3 = C_3 I_0 e^{i\omega t}$$

in which I_0 is the current in the exciter coil, ω is the frequency, ϕ is the dimensionless stream function, and C_1 and C_3 are the values of ϕ at the edges of the plate. To apply a uniform transport current, C_1 and C_3 are given the same absolute value and one is then made negative. In this way a linear

distribution of the stream function is specified which represents a uniform applied current.

Introducing these terms into equation (3-17) and substituting in the magnetic Reynold's number, one obtains:

$$\begin{aligned} \frac{\partial^2 \phi}{\partial x^2} - iR\phi + \frac{iR}{2\pi} \int_{-\ell}^{\ell} \frac{\phi(\xi) d\xi}{(x - \xi)^2 + \frac{1}{4}} = iRB(x) \\ - \frac{iRC_1[\lambda_1 + (1/\lambda_1)]}{\pi[(x - \ell)^2 + \frac{1}{4}]} [\tan^{-1}(1/\lambda_1) - \tan^{-1} \lambda_1 + (\pi/2)] \\ - \frac{iRC_3[\lambda_3 + (1/\lambda_3)]}{\pi[(x + \ell)^2 + \frac{1}{4}]} [\tan^{-1}(1/\lambda_3) - \tan^{-1} \lambda_3 + (\pi/2)] \end{aligned} \quad (3-22)$$

in which λ_1 and λ_3 are in the form of equations (3-19) and (3-20) with X and a replaced by their dimensionless counterparts, x and ℓ . With the last two terms (the edge terms) neglected, it is this governing equation which is solved by the original version of EDDY1.

3.3.2 CHANGES TO THE FINITE ELEMENT FORMULATION

The necessary modifications at the finite element level are now discussed. These changes allow the program to solve the governing equation with nonzero boundary conditions but with the differential equation unchanged. First, the new form of the

finite element equations is explained and then the necessary program alterations to implement them are examined. A third subsection discusses the specific problems for EDDY1 involved with this step.

3.3.2.1 Changes to the System of Equations

Let the full set of finite element equations be symbolized by:

$$[K] \{\phi\} = \{P\} \quad (3-23)$$

There is one equation expressing the condition at each node.

The equations are partitioned as shown in Figure 3.3. Together, Φ_2 and Φ_3 correspond to the value of Φ at all the boundary nodes. The nonzero values of Φ_2 are specified in the input while the program assumes the remaining edge values, Φ_3 , to be zero.

Following the outline of Figure 3.3, each subset of equations is written out, and then (2) is substituted into (1). From equation (4) in that figure we can generalize the following set of equations which is now solved by EDDY1:

$$\left[\begin{array}{c|c} [K_{11}] & 0 \\ \hline 0 & [I] \end{array} \right] \left\{ \begin{array}{c} \phi_1 \\ \hline \phi_2 \end{array} \right\} = \left\{ \begin{array}{c} \{P_1\} - [K_{12}] \{\phi_2\} \\ \hline \phi_2 \end{array} \right\} \quad (3-24)$$

The partitioned finite element equations are:

$$\begin{bmatrix} K_{11} & K_{12} & K_{13} \\ K_{21} & K_{22} & K_{23} \\ K_{31} & K_{32} & K_{33} \end{bmatrix} \begin{Bmatrix} \Phi_1 \\ \Phi_2 \\ \Phi_3 \end{Bmatrix} = \begin{Bmatrix} P_1 \\ P_2 \\ P_3 \end{Bmatrix}$$

in which:

(Φ_1) = Unknown Values (internal nodes)

(Φ_2) = Prescribed Nonzero Edge Values

(Φ_3) = Prescribed Zero Edge Values

The individual rows of the above equations are:

$$K_{11}\Phi_1 + K_{12}\Phi_2 + K_{13}\Phi_3 = P_1 \quad (1)$$

$$K_{21}\Phi_1 + K_{22}\Phi_2 + K_{23}\Phi_3 = P_2 \quad (2)$$

$$K_{31}\Phi_1 + K_{32}\Phi_2 + K_{33}\Phi_3 = P_3 \quad (3)$$

Substitution of (2) into (1) yields:

$$K_{11}\Phi_1 = P_1 - K_{12}\Phi_2 \quad (4)$$

Figure 3.3 Modified Solution Procedure

3.3.2.2 Changes at the Programs Level

Abel and Shepard (Ref.22) suggest an efficient algorithm for implementing these constraints. A similar algorithm given by Desai and Abel (Ref.23). The procedure is valuable because it preserves the banded nature of the equations. In the problems under consideration, however, the stiffness matrix is fully populated. Therefore, the total advantage of this algorithm cannot be realized.

The constraints are implemented in the programs by simply modifying the load vector $\{P_1\}$ with the $-[K_{12}]\{\Phi_2\}$ terms and proceeding with the solution as before.

In their original version, both EDDY1 and EDDY2 did not determine the matrix $[K_{12}]$. Therefore, revisions were necessary to have the program calculate the terms in this matrix. Introducing these revisions was tedious because the stiffness matrix is full, complex, and each term is computed as the sum of three separate components. Furthermore, one of these components involves coupling of each node to all nodes of the structure.

The following is a concise summary of the program changes made to implement the new form of the finite element equations:

- a) input the specified values of Φ_0
- b) compute the matrix $[K_{12}]$ (local and nonlocal)

- c) compute the modifying terms: $-[K_{12}]\{\Phi_2\}$ (local and nonlocal)
- d) modify the load vector (local and nonlocal)
- e) print out the boundary conditions
- f) modify the subroutines which compute eddy currents, induced temperature, and magnetic pressure so that they use the non-zero boundary conditions.
- g) place the constrained boundary values of Φ_0 in appropriate locations in output of the three stream function solutions (local, nonlocal, and image).

3.3.2.3 Implementing the Changes in EDDY1

The major obstacle in successfully modifying EDDY1 was the computation of the matrix $[K_{12}]$. As mentioned in the preceding section, each term of the stiffness matrix is actually the sum of three components. These terms can be observed in equation (3-4). Referring to this equation, the P and S terms were relatively easily found for $[K_{12}]$. The Q terms, however, were more difficult to assemble. This complication occurs primarily because the node being considered is coupled to every node in the structure through this term.

In the original version the values in $[Q_{11}]$ are computed in the subroutines ASSEM and CALC. A modified version of CALC, called CALC2, was created to compute the Q values in $[Q_{12}]$.

To make these modifications to other versions of the programs, an attempt was made to keep the changes as modular as possible. Most of the changes, therefore, are made up of several subroutines which can be added to another program. However, several fundamental alterations at the internal level were necessary also.

3.3.3 THE INDUCED FIELD EDGE TERMS

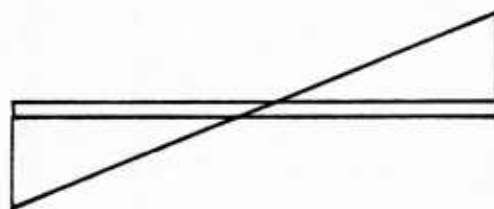
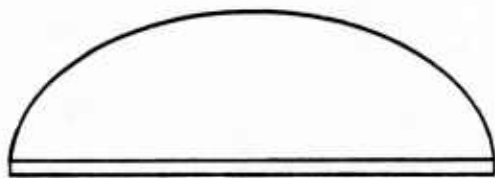
As mentioned earlier, the governing differential equation for the problem with a transport current is different than the problem without a transport current. The difference is the existence of the "edge terms" in the derivation of section 3.2 for the transport current problem. This section discusses the physical significance of these terms first, followed by the method used to include them in the program. This is the second step in implementing transport current capability in the programs.

3.3.3.1 The Significance of the Edge Terms

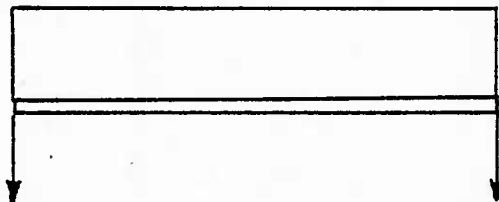
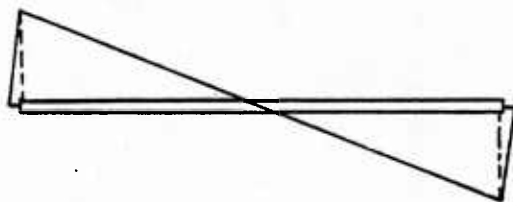
In the problem where a transport current is not applied, the distribution of the stream function under a uniform magnetic field will appear as in Figure 3.4a. The value of the stream function is forced to zero in both the finite element equations and the induced field representation.

Φ

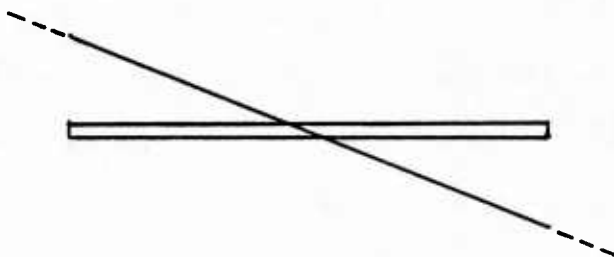
J



(a)



(b)



(c)

Figure 3.4 Stream Function and Corresponding Current Distributions in an Infinite One-Dimensional Plate

Now, if the finite element equations are modified as in the preceding section to admit nonzero boundary conditions, the stream function distribution will become changed. For the case of a pure low frequency uniform transport current, the distribution will be linear with an abrupt drop to zero at the ends as shown in Figure 3.4b. The sharp drop-off to zero at the edges occurs because the induced field expression used in equation (3-1), assumes Φ to be zero at the edges.

The question may now arise as to what problem has been solved at this point. The problem is that of a transport current with concentrated currents flowing along the edges in the reverse direction. This current pattern is evident from the stream function distribution of Figure 3.4(b) by its sharp gradient at the edge of the plate.

The final step in the development is then to have a formulation containing an induced field expression which does not assume the stream function to be zero on the edges. This formulation is given in equation (3-22) for the 1D case. The difference in employing this formulation versus the original one is the inclusion of the "edge terms" previously mentioned. These terms are the last two terms in equation (3-22).

The effect of including these edge terms is to cancel out the reverse edge currents implied by the stream function distribution in Figure 3.4b. On the edges now, the stream function may remain nonzero which results in a distribution as shown in Figure 3.4(c).

3.3.3.2 Including the Edge Term Effects

For reasons brought out later on, an approximate method of cancelling out the reverse edge currents implied in the original program is used in this study rather than a direct application of the edge terms to the current program. This method is judged to represent adequately the effect of the edge terms in cancelling out the reverse edge currents implied in the present induced field expression.

The method proposed for including edge effects assumes that the reverse current sheets actually on the plate edges can be approximated by current filaments. Therefore, to cancel out the effect of the reverse edge currents, one simply applies a loading of two current filaments at the ends of the plate. In this manner, a magnetic field is set up which represents the field given by the edge terms in the complete formulation.

This method of including the edge effects can be justified by showing the equivalence of these two representations. In other words, the formulation containing the full induced field can be

shown identical to the formulation with an applied field generated by two edge filaments. For simplicity, consideration is given to the case where no other externally applied magnetic fields exist.

The governing equation (3-17), reduced to the 1D case, serves as the starting point for the full formulation. By considering $h^2/4$ to be small the integration of the edge terms is greatly simplified. After this assumption the governing equation may be written:

$$\begin{aligned} \frac{\partial^2 \psi}{\partial X^2} - \sigma \mu \frac{\partial \psi}{\partial t} + \frac{\mu \sigma h}{2\pi} \int_{-a}^a \frac{\partial \psi(X')/\partial t}{(X-X')^2 + (h^2/4)} dX' \\ = \frac{\mu \sigma h}{2\pi} \left[\frac{\partial \psi_3}{\partial t} \frac{1}{(X+a)} - \frac{\partial \psi_1}{\partial t} \frac{1}{(X-a)} \right] \end{aligned} \quad (3-25)$$

The next step is to nondimensionalize this equation using the relationships given in (3-21). Using the same procedure as before and considering the case when $C_3 = -C_1$, the above equation becomes:

$$\begin{aligned} \frac{\partial^2 \phi}{\partial x^2} - iR\phi + \frac{iR}{2\pi} \int_{-\ell}^{\ell} \frac{\phi(\xi) d\xi}{(x-\ell)^2 + \frac{1}{4}} \\ = \frac{iRC_3}{2\pi} \left[\frac{1}{x+\ell} + \frac{1}{x-\ell} \right] \end{aligned} \quad (3-26)$$

In the second case the starting equation is the dimensionless formulation used by the original version of EDDY1. An applied field, B^0 , for two edge filaments is substituted into this equation. By superimposing the field due to two individual current filaments, the expression for the total applied field is obtained. This equation is in nondimensional form:

$$B_T(x) = \frac{\mu i}{2\pi h} \left[\frac{1}{(x + \ell)} + \frac{1}{(x - \ell)} \right] \quad (3-27)$$

where i is the current in the edge filaments.

Using the definition of the stream function the current i is now written in terms of Ψ . The appropriate expression for the distribution of the magnetic field is then:

$$B(x) = \frac{C_3}{2\pi} \left[\frac{1}{(x + \ell)} + \frac{1}{(x - \ell)} \right] \quad (3-28)$$

Substitution of this form of the applied field into equation (3-22) without the edge terms yields:

$$\begin{aligned} \frac{\partial^2 \phi}{\partial x^2} - iR\phi + \frac{iR}{2\pi} \int_{-\ell}^{\ell} \frac{\phi(\xi) d\xi}{(x - \ell)^2 + \frac{1}{4}} \\ = \frac{iRC_3}{2\pi} \left[\frac{1}{x + \ell} + \frac{1}{x - \ell} \right] \end{aligned} \quad (3-29)$$

Equations (3-26) and (3-29) are identical. Thus, we have shown when h is small that the formulation solved by EDDY1 in this manner is identical to the exact formulation containing the full expression for the induced field.

This technique for including the edge effects is further justified when one considers how these effects differ between the local and nonlocal problem. For simplicity here a pure transport current case is considered. In the local problem the frequency is small, and hence the time rate of change of the total magnetic field will be small also. Hence, the induced currents given by Faraday's Law will be negligible and the resultant current distribution will be unchanged from that of the applied current.

On the other hand, for the nonlocal problem the frequency is high which causes significant induced currents. As a result the applied current distribution will be changed to achieve an equilibrium between the magnetic fields.

This comparison of the local and nonlocal cases implies that the edge terms will have no effect on the solution of the problem at hand for low frequencies. Therefore, it is of no use to implement these terms into the programs for the local case. The influence of the edge terms will be felt, however, in the nonlocal case.

These observations can be clearly seen in the output from EDDY1 as shown in Figure 3.5. This figure shows the current distributions computed by EDDY1 for a pure transport current at several frequencies. The Reynold's number is used to express the relative frequency of the various cases. The results here are based on the method of accounting for the edge effects described previously.

One can see from Figure 3.5 that the influence of the induced field is not really felt for Reynold's numbers less than unity. Furthermore, Figure 3.6 compares the solution with and without the edge term effects for a Reynold's number of five. Even for this large Reynold's number the maximum difference in the two solutions is only five per cent.

In an actual plate problem, the concept of skin depth is useful in determining whether the induced field has a significant effect. The skin depth, δ , is defined as the depth to which an oscillating magnetic field can penetrate a conductor and is given by [18]:

$$\delta = \left(\frac{2}{\mu \sigma \omega} \right)^{\frac{1}{2}} = h \left(\frac{2}{R} \right)^{\frac{1}{2}} \quad (3-30)$$

in which R is given in equation (3.1) for the one-dimensional plate, and h is the plate thickness.

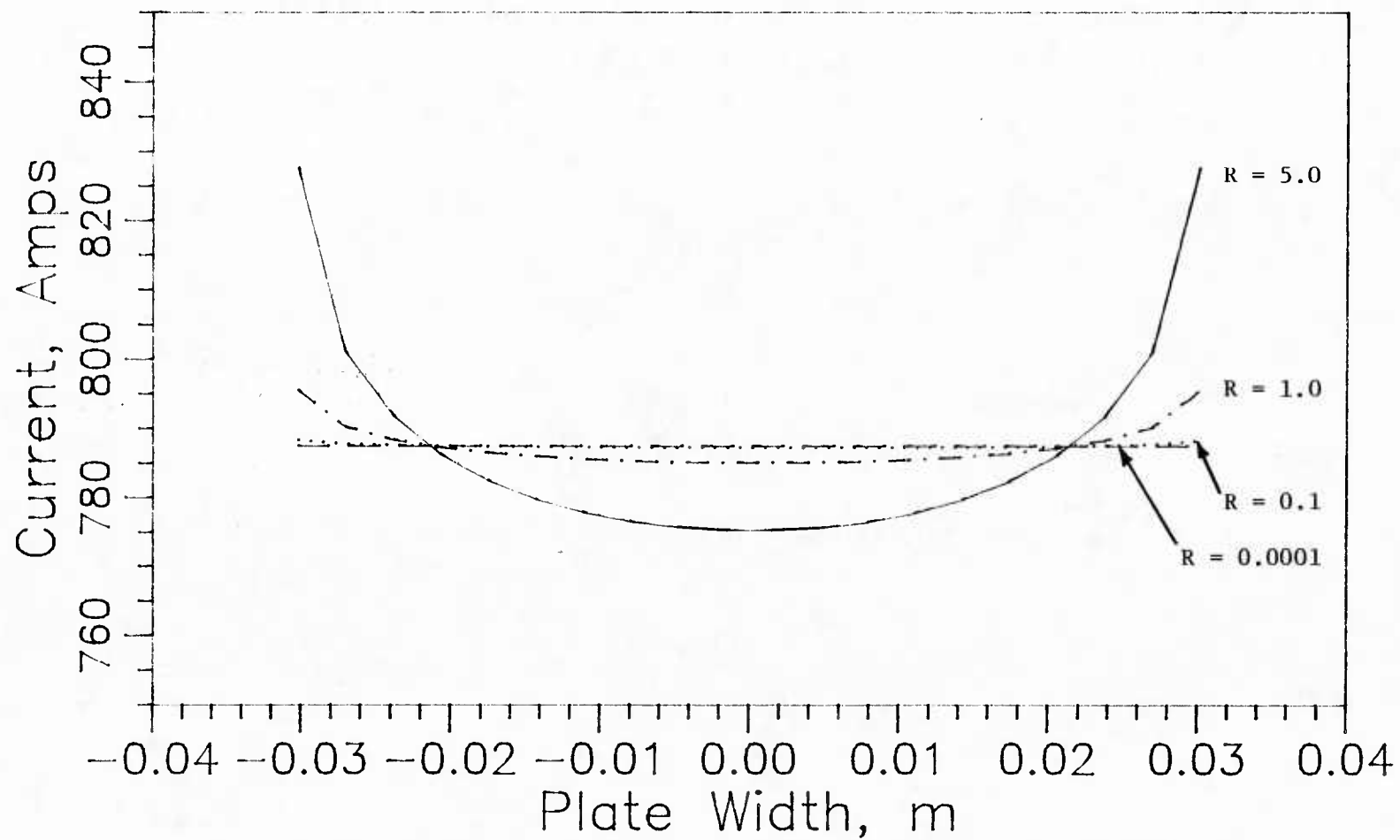


Figure 3.5 Comparison of Current Distribution for Different Reynold's Numbers, computed by EDDY1.

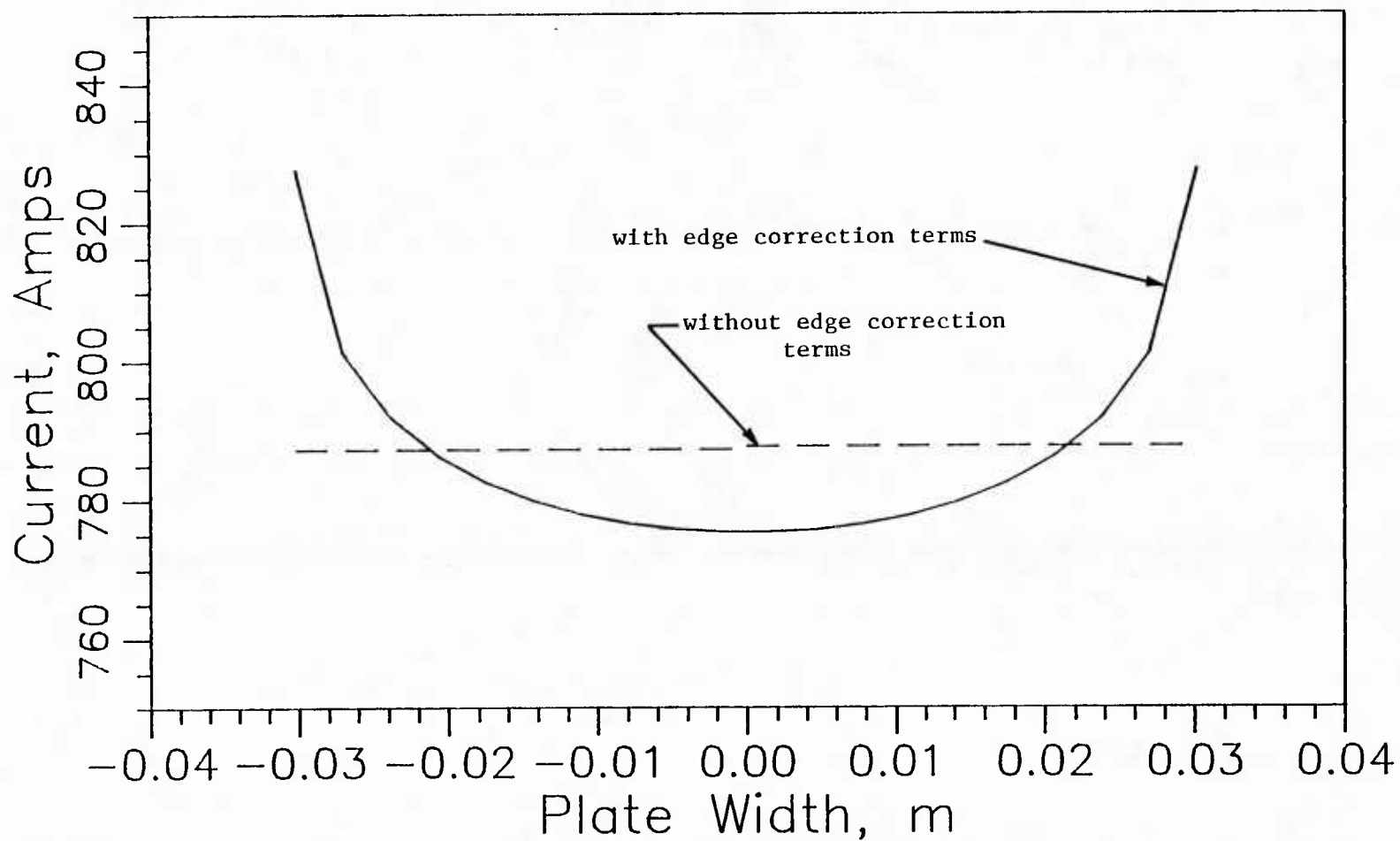


Figure 3.6 Comparison of EDDY1 Pure Transport Current
Solution with and without Edge Correction Terms, $R = 5.0$

Equation (3-30) can be used to compute the ratio of skin depth to plate thickness for a problem with a particular Reynold's number. Problems in which the ratio of skin depth to plate thickness is less than about 0.5 should not be analyzed by EDDY1 because in these cases the magnetic field does not penetrate the full plate thickness as assumed in the program. For $R = 5.0$ the ratio of skin depth to plate thickness is 0.65. Therefore, the Reynold's number of five considered in Figure 3.5 is a good upper limit on the range of R 's which can be treated with EDDY1.

As an example of a physical situation, the electromagnetic blunting problem studied in Chapter 4 is considered. For the case of the stainless steel strips the skin depth is calculated to be 11.7 mm and in the case of the titanium it is 18 mm. The thickness of the stainless steel strips is 0.965 mm while the titanium strips are 1.4 mm thick. Therefore, the induced field in both cases will be felt through the entire depth.

The magnetic Reynold's number can be calculated using the appropriate specimen thickness in each case. In both the stainless steel and titanium tests the Reynold's number is approximately 0.3. Hence, for the electromagnetic blunting problem, the induced field does not appear to have a significant influence. Based on these calculations then, neglecting the edge terms is of no consequence in the analysis of these problems in one-dimension.

To summarize, implementation of the full expression for B does not appear warranted in light of the preceding discussion. The edge terms are shown to be of consequence only in the nonlocal case and to have a maximum influence of only about five percent. Nevertheless, it is recommended that later studies explore situations where the edge effects are significant (e.g., the 2D case) and include them in computer programs for such cases.

3.4 VERIFICATION OF TRANSPORT CURRENT CAPABILITY IN EDDY1

The main focus of this section is a series of tests done to verify the accuracy of EDDY1. Before the description of these checks, several related changes made to EDDY1 are briefly described. While these changes are worthy of mention, they are not major modifications such as those described in section 3.3.

3.4.1 RELATED CHANGES TO EDDY1

The output of the revised program shows the boundary conditions and indicates whether a pure transport current case exists. In addition, the real and imaginary $[K_{12}]$ matrices and the modified load vector for both the nonlocal and local solutions are printed.

Changes were also made to the results section. In summary, these are:

1. The local solution is indicated as purely imaginary rather than real as before. From equation (3-4) one can see the local solution must be imaginary. The local form of this equation is obtained by dropping the second and third terms on the right hand side. This results in the following equation for the local problem:

$$-[S] \{\phi\} = i\{R\} \quad (3-31)$$

To satisfy this equation the values of the stream function must be negative and imaginary.

2. In the stream function and eddy current solutions the sign of the "modulus" was changed to be concurrent with the sign of the imaginary part. The solutions' orientation is generally dominated by the imaginary component and hence, the sign of these values was changed to more clearly express this bias. In each heading, "modulus" was changed to read "resultant" to better describe the meaning of this value.
3. Measurement of the phase angle is now from the standard excitation which is negative and purely imaginary. This characteristic of the excitation is evident in the right hand side of equation (3-4) after multiplying thru by -1.

4. The output now contains text which defines "resultant" and indicates the standard excitation is negative and imaginary.

3.4.2 DESCRIPTION OF THE CHECKS

Verification of the program was approached in three ways. First, the solution and new parts of the "stiffness" matrix were compared with hand calculated values for a three-element problem. Second, a "verification grid" was used to check the results from a series of problems against the expected response. Finally, for a DC transport current situation, the induced magnetic field was determined three ways: by experiment, from the program, and from an analytical expression. The distribution of B from each of the three methods was then compared. This last check applied only to the local solution. These three aspects are described in the following three subsections.

3.4.2.1 Comparision with Hand Calculation

The matrix terminology used below follows that of equation (3-3). The S and P components of the $[K_{12}]$ matrix for a three-element problem were calculated by hand. The matrices computed by the program were found to agree with these values exactly. To confirm the placement of the Q terms into their correct location in $[K_{12}]$, the S and P components were added to the program's $[Q_{12}]$ matrix. As expected, the resulting matrix was found to agree with $[K_{12}]$ of the program. This was also checked

in the ten-element problem. These checks are valid for all ranges of Reynold's numbers (i.e., for local and nonlocal problems).

In addition, the local stream function solution was computed by hand and found to match the program solution.

3.4.2.2 Verification Grid

A series of checks outlined in Figure 3.7 was run for both three- and ten-element problems. These checks revealed several errors which were corrected. The final version was made to satisfy all these checks.

Shown in horizontal rows in this figure are the three stages of the program which were examined. At the first level, the local solution was checked using a low Reynold's number. For this case the local and nonlocal solutions should be identical; hence, in the second row of verifications the nonlocal solution was checked for agreement with the local solution for low R. The third level examined in the program was the nonlocal solution for high Reynold's number.

At each of these three steps in the verification, the following four individual cases were run:

- (a) the original program
- (b) the new program with zero boundary conditions for the stream function, i.e., the induced current case

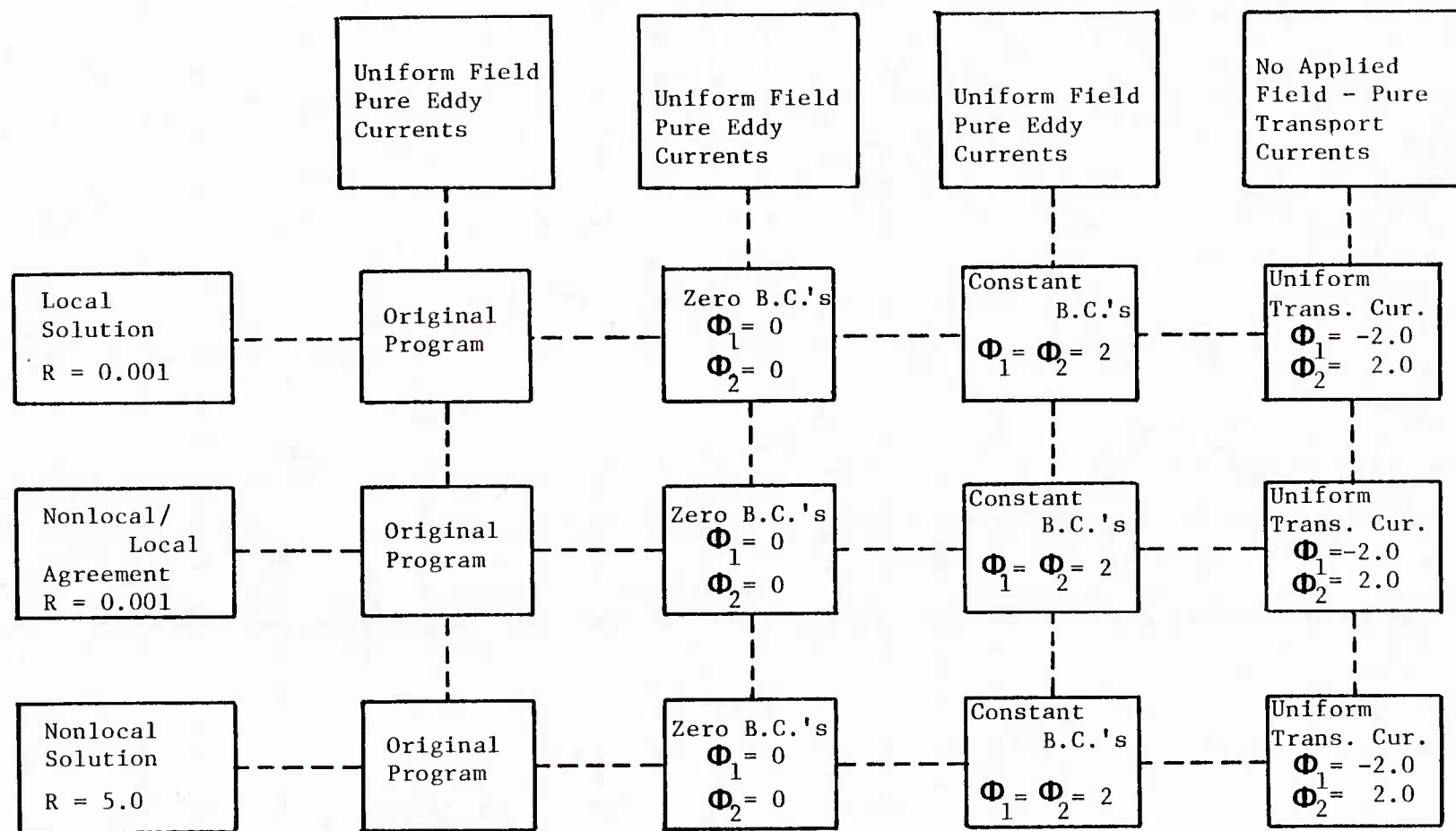


Figure 3.7 Verification Grid for EDDY1

- (c) the new program with constant, equal values of the stream function on the boundary, i.e., another version of the induced current case
- (d) the pure transport current case, i.e., equal magnitude but opposite sign boundary conditions on opposite edges of the plate

Each of these problems corresponds to a column in Figure 3.7. Considering verification in the horizontal direction, the results using zero boundary conditions were found to agree exactly with those of the original program. Furthermore, the results from the constant boundary values case were found to equal the original program's results with the constant superimposed. Finally, the stream function in the pure transport current case was checked. To do this a uniform transport current was applied by specifying $C_3 = -C_1$. In the local problem, the analytical solution is relatively simple, and, therefore, the results were easily shown to be correct. For this case the current solution is same as the applied current which is $I = (C_3 - C_1) / 2l$. In the high R case the stream function distribution was found to be symmetric as expected due to the symmetry of the problem. All these points were satisfied with the new program.

3.4.2.3 Comparison of the Induced Field

The component of the induced field perpendicular to the plate was determined at the surface of the plate in three different ways. First, an analytic expression for B was developed by superposition. The magnetic field between two current filaments was found analytically and then used to cancel out the reverse edge currents implied in the one dimensional version of equation (2-12). The condition associated with the latter equation is that of Figure 3.4(b). Second, based on a local solution with EDDY1, the B distribution was computed from the currents over the width of the plate using a current filament approximation. The current in each element, computed by the program, was treated as a concentrated filament at the centroid of the element. At each point on the surface of the plate, the contributions computed from the Biot-Savart Law of all the current filaments were superimposed. For both of the techniques just described, a small computer program was written to perform the repetitive calculations. The third case involved experimental measurement. A DC current was applied along a flat strip, and the actual induced field was measured along a transverse of the strip using a gaussmeter.

These three methods were used to compute the B for three levels of current, 25, 50, and 75 amperes. Excellent agreement was found for all three cases as shown in Figures 3.8, 3.9, and

3.10. The distributions computed by the analytical method and from EDDY1 are so close that they are shown by the same curve in these figures.

Also included in these figures is the induced field calculated analytically without correcting for the reverse edge currents. This provides another insight on the influence of these edge terms. The expression used here is equation (2-12) which was originally proposed in Reference 19. In Figures 3.8, 3.9, and 3.10 this curve is referred to as the "uncorrected analytical" solution to indicate that the reverse edge currents have not been cancelled out. From these curves one can see that the edge currents have a substantial effect on the induced magnetic field near the edge of the plate. This observation for the induced field is a paradox to the corresponding observation made in Section 3.3.3.2 and Figure 3.6 which indicates that the edge current effect on the current distribution is insignificant. To summarize, the reverse edge currents appear to have considerable influence on the induced magnetic field in the plate but have only a minor effect on the resulting current distribution.

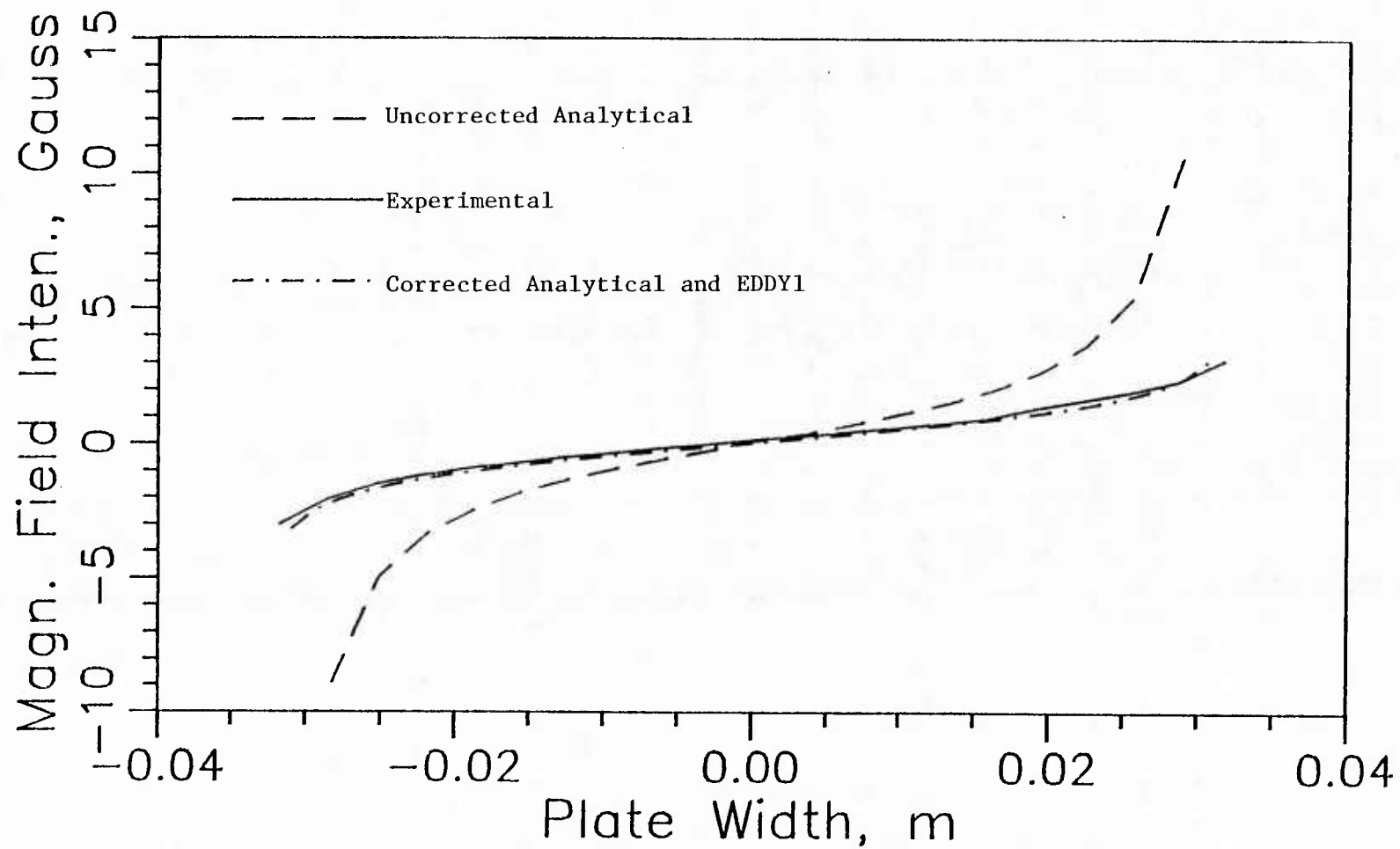


Figure 3.8 Comparison of Induced Magnetic Field Distributions for a DC Current Strip with $I = 25$ Amps.

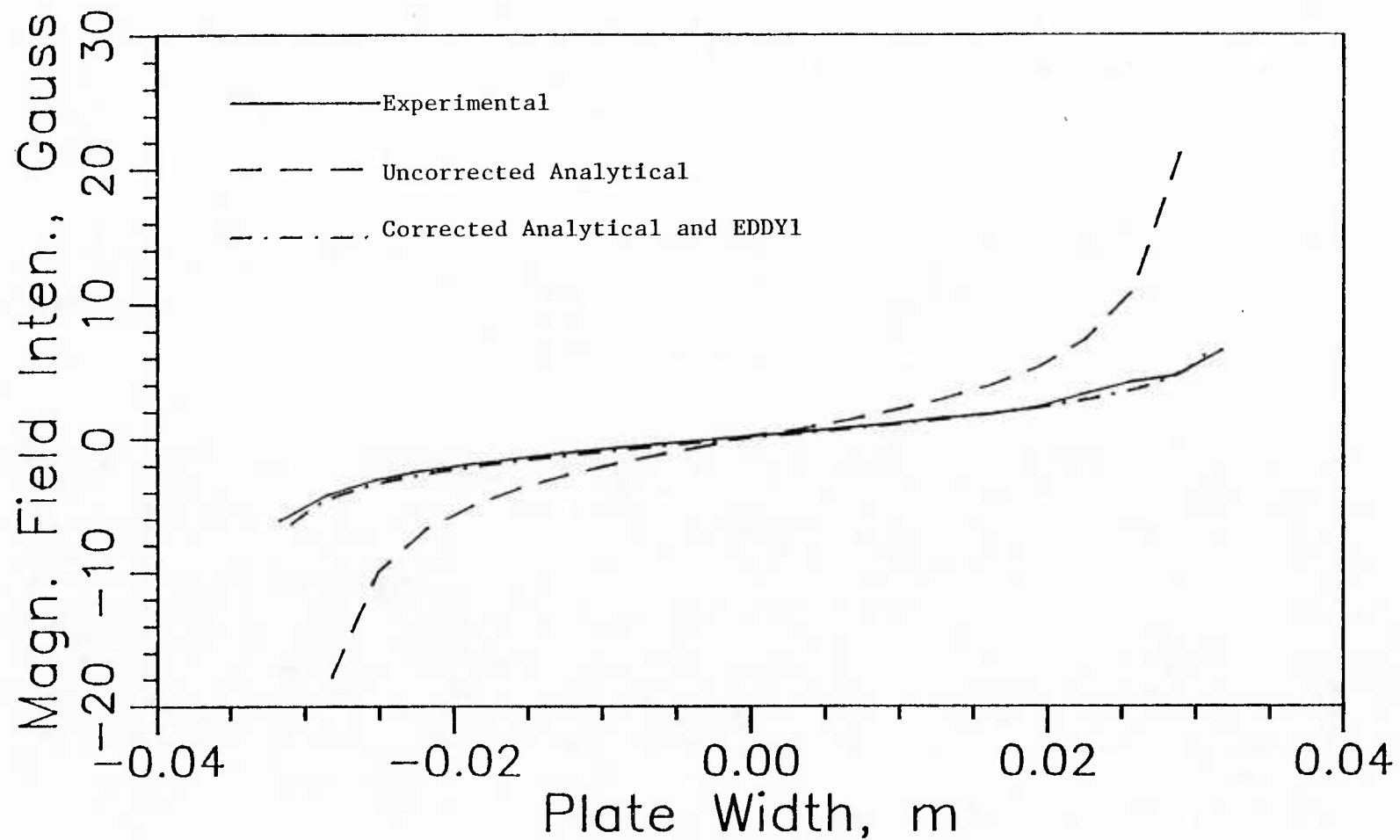


Figure 3.9 Comparison of Induced Magnetic Field Distributions for a DC Current Strip with $I = 50$ Amps

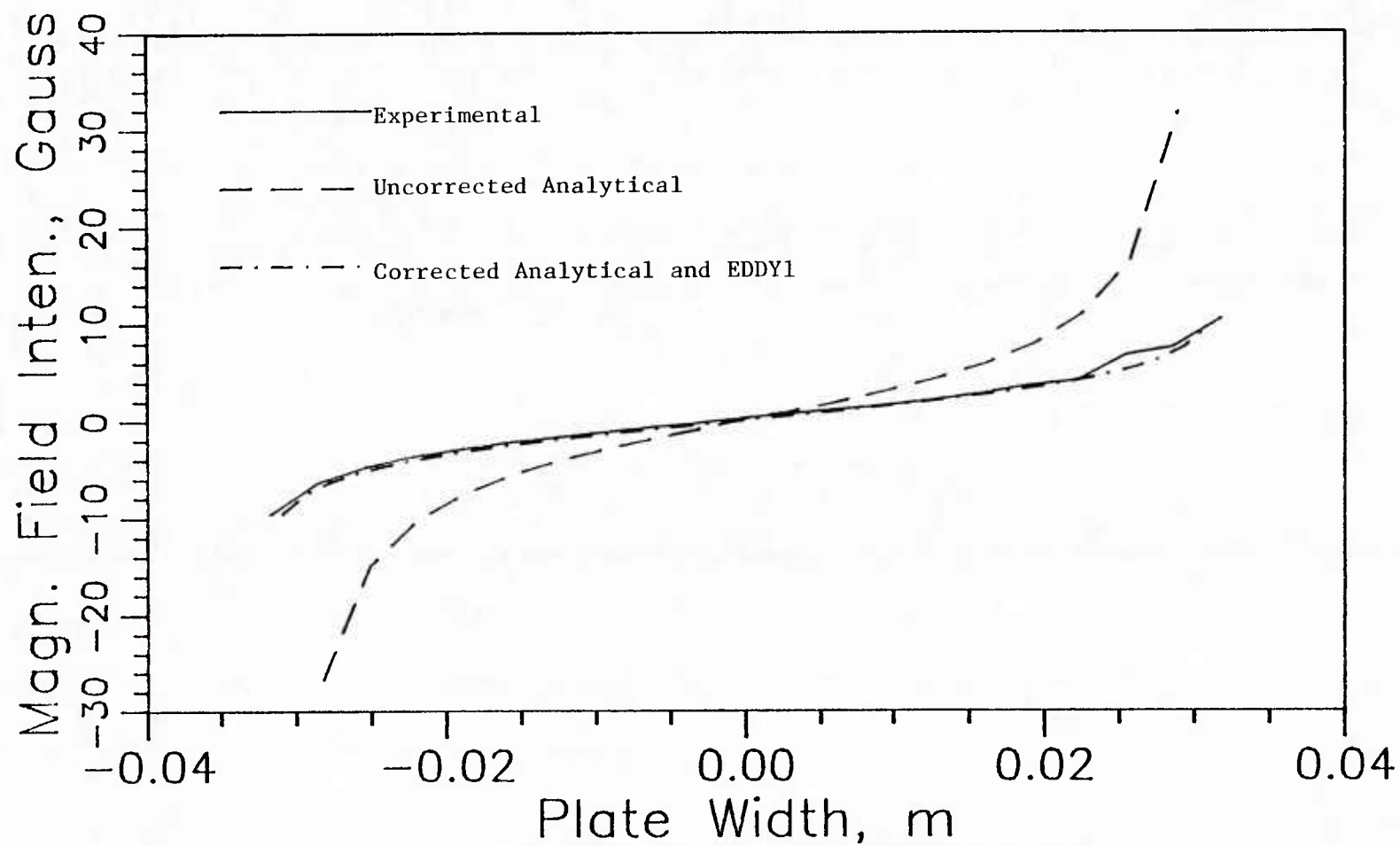


Figure 3.10 Comparison of Induced Magnetic Field Distributions
for a DC Current Strip with $I = 75$ Amps

CHAPTER 4

ELECTROMAGNETIC CRACK-TIP BLUNTING

The subject of this chapter is the blunting of fatigue cracks by electromagnetic effects. Use of the term "blunting" here indicates the formation of a hole by melting at the tip of the crack. The hole tends to causes a redistribution of stress which decreases the large stresses at the crack tip. From a mathematical standpoint, this alleviates the stress singularity at the crack tip provided the hole is smooth.

Much of the following discussion recounts the experimental work done in this study. The first section describes the various apparatus and procedures used in the different phases of experimentation. An individual section is then devoted to the results for each of the two materials used: stainless steel 304 and titanium alloy Ti-6Al-4V. A final section in this chapter presents a discussion of the experimental results. The succeeding chapter considers analytical studies of the tested configurations.

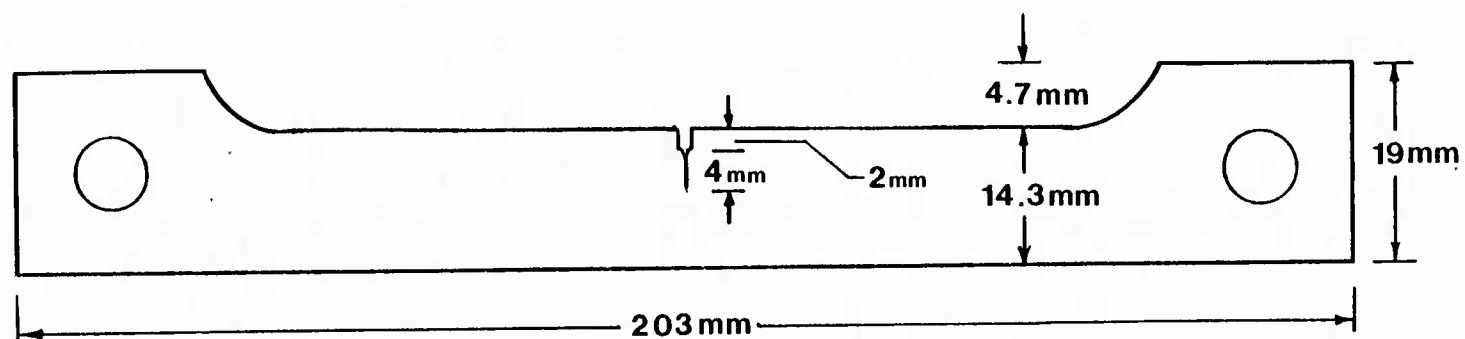
4.1 BASIC TESTING APPARATUS AND PROCEDURE

The equipment and procedure for three general phases of the experiments are described here. First, the process used to generate specimens with fatigue cracks is outlined. Second, the technique of producing holes at crack tips using electromagnetics is described. This section is followed by a description of the methods used to analyze the blunted samples. A fourth section reports on the work done to study the effects of heating on the metals.

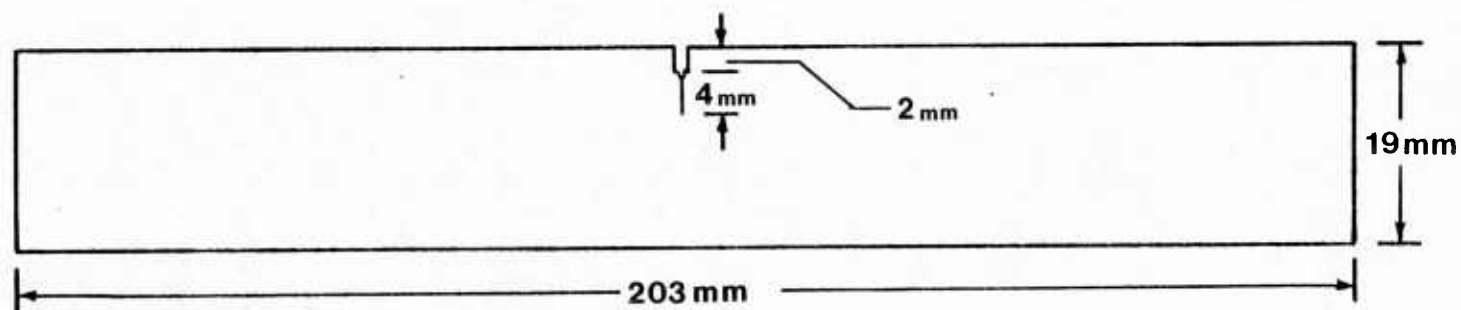
4.1.1 FATIGUE CRACK GENERATION

In the fatigue cracking procedure an MTS hydraulic loading system is used to place a cyclic load on the specimens. Before being placed into the fatigue apparatus, each specimen is machined to a standard geometry for that material. These standard specimen geometries are shown in Figure 4.1 for both stainless steel and titanium.

To cause the crack to initiate at the center of each specimen, a two millimeter slot is cut into the side of each specimen as shown in Figure 4.1 to concentrate the stress at the desired cross section. Furthermore, to create a specific point at which the crack is to begin, a notch is placed at the end of each slot with a razor blade.



(a) Stainless Steel 304 Specimen Geometry



(b) Ti-6Al-4V Specimen Geometry

Figure 4.1 Standard Specimen Geometries

A cyclic loading frequency of twenty Hertz is used in all cases. For each metal some preliminary experimentation is performed to determine the range of load which produces a crack in a reasonable amount of time. For titanium alloy with a six millimeter crack the load limits are 750 and 1750 pounds for the duration. However, the limits for the stainless steel are set at 200 and 800 pounds initially, and then lowered to 100 and 700 pounds after the crack begins. This is done to slow the rate at which the crack propagates.

To insure that the total crack length and remaining uncracked material are the same in all of the specimens, a score line is placed exactly six millimeters from the notched edge on each specimen. During the cyclic loading process the crack is carefully observed under a microscope and stopped once the score line is reached.

In the case of the stainless steel the ductility of the metal allows the crack to be seen easily under the microscope once the cyclic loading is stopped. The titanium crack, on the other hand, is relatively difficult to discern because of the material's brittle nature. To monitor the crack accurately in the titanium it is necessary to halt the cyclic load and apply a static load sufficient to open the crack to its full length.

4.1.2 THE ELECTROMAGNETIC BLUNTING OPERATION

The blunting operation consists of creating a hole at the tip of a crack to decrease the concentration of stress at that point. Figure 4.2 depicts the basic apparatus for the procedure described below. The hole is produced by attaching the ends of a specimen to a 20kJ capacitance storage bank. By passing a current pulse through the specimen, current is concentrated at the crack tip. When the current density is sufficient, melting occurs as a result of Joule heating. For a particular specimen the amount of melting depends on the size of the current pulse. A hole is formed because the magnetohydrodynamic forces act on the molten metal to force it out of the crack-tip region. Figure 1.1 shows a typical hole that results in stainless steel.

Different hole shapes result, depending on the material type and the degree to which the fatigue crack provides infinite resistance. In other words, the surfaces of the crack can be close enough in some cases so that the current can jump across the gap. The result is incomplete hole formation and melting along the crack. This effect is especially evident in titanium. The brittle nature of this metal results in very tight cracks because little permanent deformation occurs during the cracking procedure.

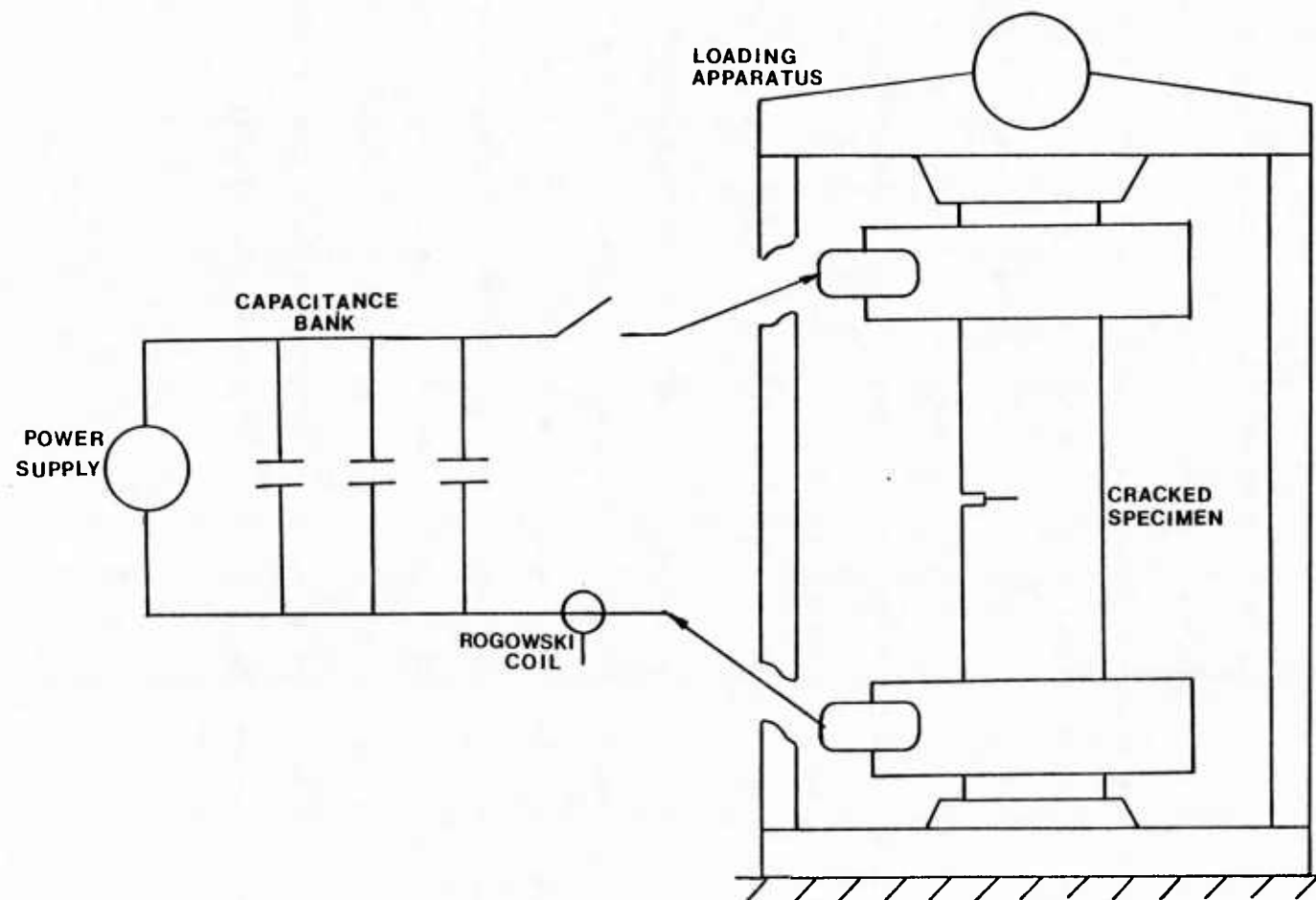


Figure 4.2 Electromagnetic Blunting Apparatus

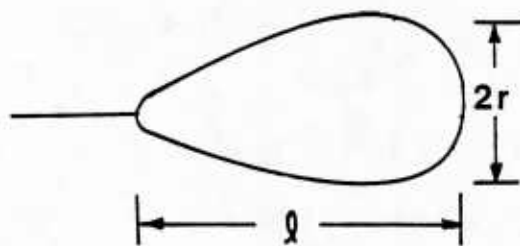
To overcome these difficulties associated with titanium, the specimen is placed in tension during the current pulse. As shown in Figure 4.2, a loading machine is set up in conjunction with the capacitance bank to do this. By placing the specimens under load, the fatigue crack is opened sufficiently to prevent the current from jumping across it.

The special grips shown in Figure 4.2 are designed to permit application of the charge to the specimen in the loading machine. Also, insulation of the loading machine is required to prevent the current from travelling through it rather than through the specimen.

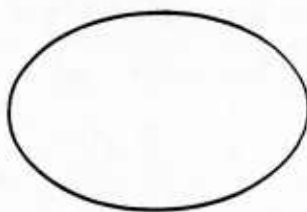
To measure the size of the current pulse, a Rogowski coil is placed around one of the capacitance bank leads, and its signal is monitored on an oscilloscope. Photographs were taken of the resulting scope images of voltage versus time. By integrating this signal over time one obtains the "size" of the current pulse in terms of total amperage.

4.1.3 THE ANALYSIS OF BLUNTED SAMPLES

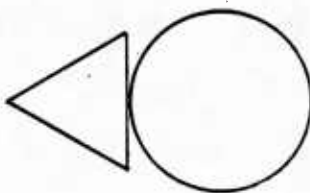
After the specimen has been blunted, careful measurements are taken of the hole length, hole width, and remaining strip width. As shown in Figure 4.3(a), the hole width, $2r$, is taken as the dimension in the longitudinal direction of the strip. The other dimension is the hole length, ℓ , which is measured in the



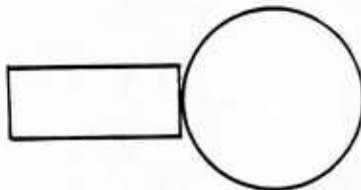
(a) Typical Teardrop Shaped Hole



Ellipse



Circle-Triangle



Circle-Rectangle

(b) Configurations for Equivalent Hole Diameter

Figure 4.3 Blunted Hole Geometries

transverse strip direction. For most specimens the hole length is the longer of the two dimensions. In addition, the width of the remaining material is measured to calculate the ultimate stress on the net section. These measurements are made on both faces of the specimen and then averaged to obtain a value over the thickness.

The hole dimensions data are now used to calculate two quantities useful in comparing results. First, a value of effective crack-tip radius, r , is defined as half of the hole width (measured parallel to the long direction of the specimen). This parameter is determined directly from the hole dimensions. It provides a useful measure of relative hole size and a measure of the curvature in the melted hole. The effective crack-tip radius is used to present nearly all of the experimental results in this chapter.

A second quantity used in comparing results is the equivalent circular hole diameter which is based on the melted area of the specimen. This value is computed as a measure of total melted area and is defined as the diameter of a circular hole which would have a melted area equal to that of the actual specimen. The area of the melted regions can be approximated as the area of a known shape or the combination of several known shapes. It was found that four configurations can be used to cover essentially all of the melted geometries that arise. These shapes are a circle, an ellipse, a circle-triangle combination, and a circle-rectangle combination. The last three configurations are shown in Figure

4.3(b). Formulas for the equivalent circular diameter were developed by equating one of these areas to the area of a circle and solving for its diameter. The equivalent circular hole diameter is used only to present hole size as a function of current in Figure 4.5.

In some cases photographs are also taken as a record of the blunted geometry. A typical photograph showing a magnified view of a blunted stainless steel sample is given in Figure 1.1.

The final step is the testing of the strips for ultimate strength. A 10,000 pound United testing machine was used to pull the specimens directly to failure and to record the maximum load attained.

4.1.4 STUDIES ON THE EFFECT OF HEATING

Blunting has the benefit of reducing the degree of stress concentration at a crack tip. However, in this process the possibility of undesirably affecting the material properties by heating also exists. Therefore, the effect of the melting on the region surrounding the hole is studied to supplement the experimental work.

This problem is addressed in two ways in this study. First, a group of stainless steel specimens is blunted by drilling holes rather than melting them. The results of the ultimate strength tests on these are presented in section 4.2.2. The second

approach to this problem is to analyze the grain structure in the melted regions. This study is preliminary rather than a full metallurgical treatment of this problem. A more detailed examination of the effects of heating on titanium and stainless steel as it pertains to this problem is recommended.

To study this problem from a metallurgical viewpoint, a series of specimens, both titanium and stainless steel, are obtained in the heated (blunted) and unheated (unblunted) conditions. The next step is to mount the critical area of each specimen into a disk to allow ease in handling. Following standard metallurgical procedures, these mounted specimens are polished using a series of grits which become progressively finer in size. The specimens are polished to a final grit size of 0.05 microns. Some specimens are then etched with Kroll's reagent [33] to make the grains more distinct. At this stage the mounted specimens are examined under a microscope and photomicrographs are taken to record the various grain structures.

4.2 STAINLESS STEEL 304

This section presents the results of tests done on stainless steel 304 specimens. Figure 4.1(a) shows the geometry of the stainless steel specimens, all of which are of a thickness 0.965mm. One side of the strips is milled down 4.7 mm to create a higher current density in this section while maintaining

sufficient material at the ends to attach the leads of the capacitance bank.

Since fatigued samples are time consuming to obtain and limited in quantity, a preliminary group of specimens containing only razor notches is useful at the outset to develop a reliable blunting procedure. In these specimens, melted holes from the electromagnetic blunting procedure are observed at the end of the razor notches. It should be noted that a slightly different geometry is used for these tests than that given in Figure 4.1(a). The width of the milled section is 13.8 mm as opposed to 14.3 mm.

Three sets of stainless steel specimens are tested to ultimate strength. The first series of strips contain fatigue cracks which are blunted electromagnetically. A second group is blunted by drilling a hole rather than melting, to provide a basis for comparison of the heating effect. In this set holes are drilled at the tip of the razor notches for the uncracked specimens and at the tip of the fatigue cracks in the cracked specimens. Finally, a third group is blunted electromagnetically in the presence of either an external magnetic field or a stream of nitrogen gas for cooling. These specimens are tested to observe the influence of a magnetic field or a cooling jet on the formation of a blunting hole.

The results of testing done in fatigue cracked specimens, drilled hole specimens, and special effect specimens are presented in the following three sections. A fourth section expresses the important points gleaned from the tests on stainless steel.

4.2.1 FATIGUE CRACKED SPECIMENS

Figures 4.4, 4.5, 4.6, and 4.7 present the results of experiments done on stainless steel specimens containing fatigue cracks. The first figure shows the effective crack-tip radius plotted versus applied current. By performing a linear regression analysis on the logarithms of this data, one obtains the logarithmic curve shown in Figure 4.4. The high degree of scatter in this relationship is indicated by the low correlation coefficient of 0.65.

Linear regression of logarithms is used again to express the relationship between the equivalent circular diameter and current in Figure 4.5. As previously mentioned, the equivalent circular diameter is based on the melted area of the specimen and hence is a better measure of the total amount of melting than the effective crack-tip radius. This data also exhibit large scatter and has a correlation coefficient of 0.65.

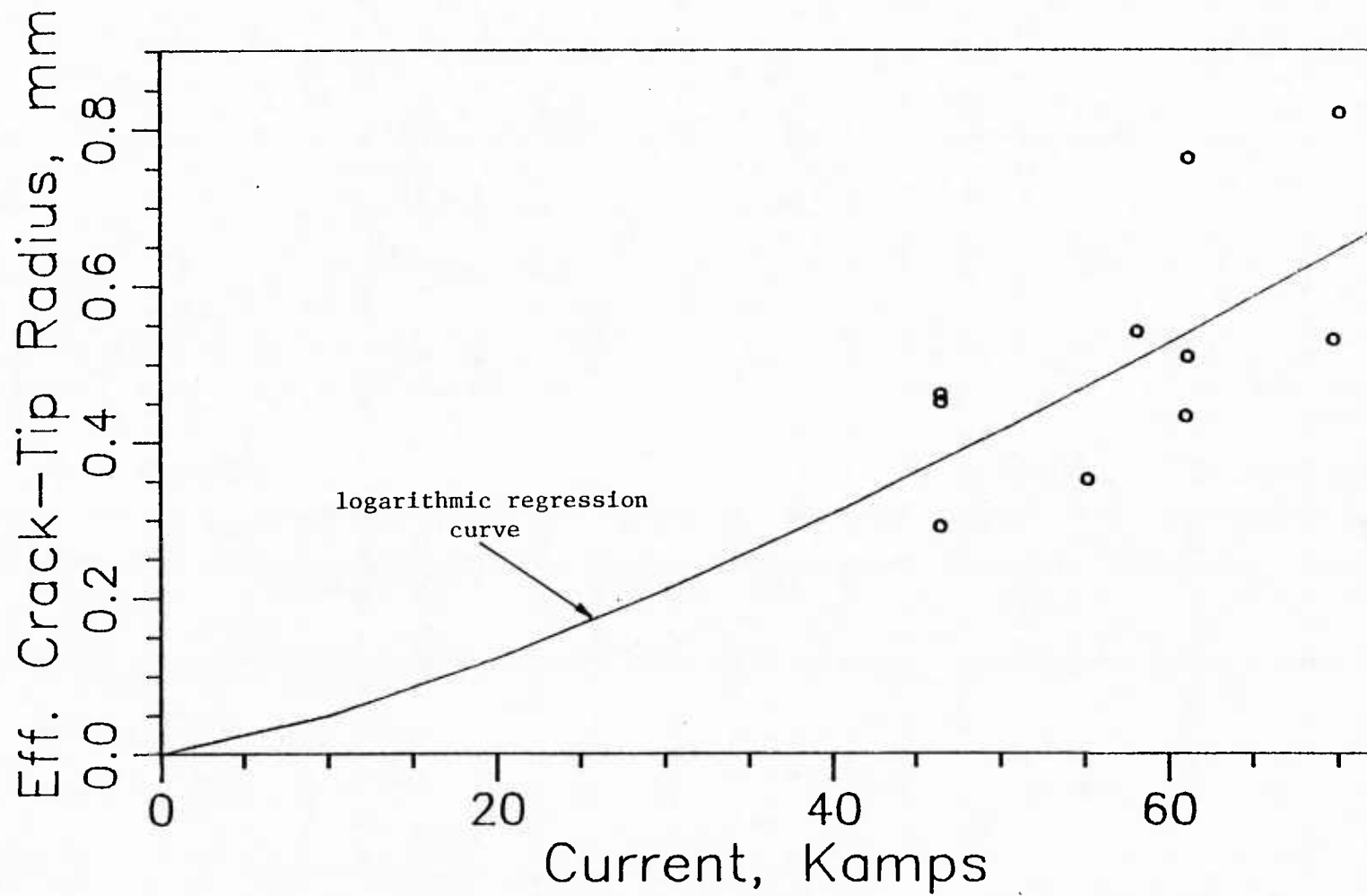


Figure 4.4 Effective Crack-Tip Radius vs. Current in SS304

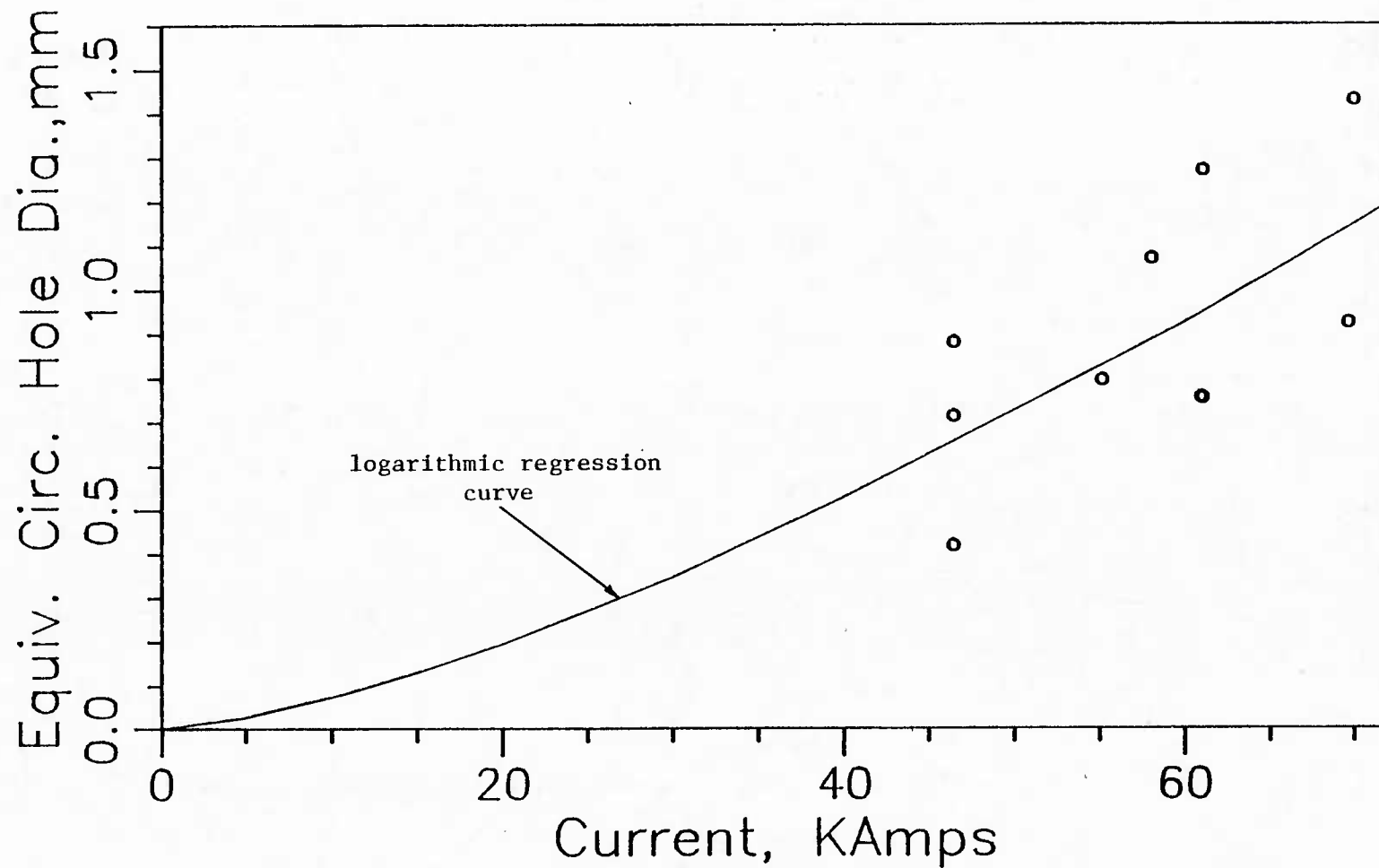


Figure 4.5 Equivalent Circular Hole Diameter vs. Current in SS304

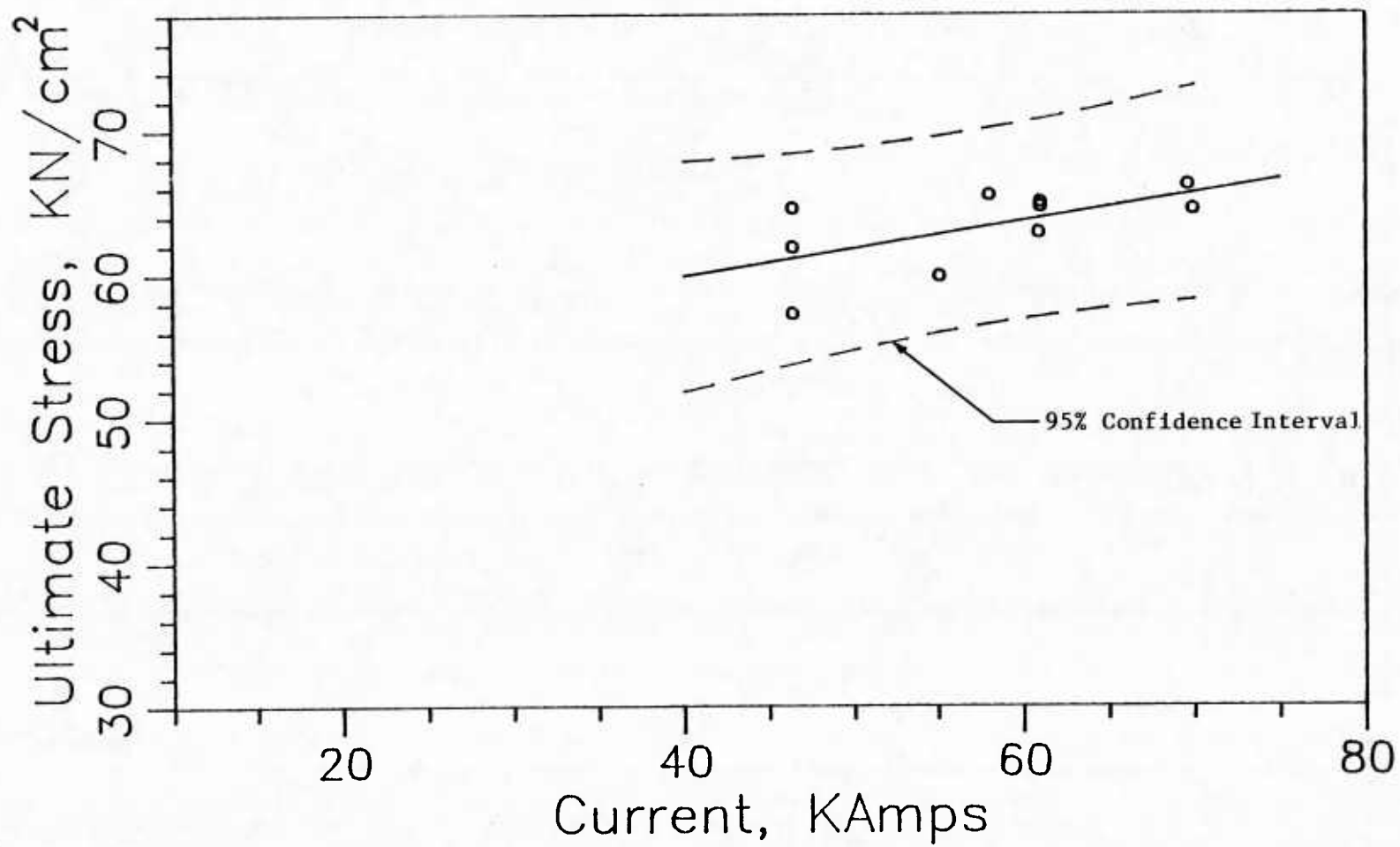


Figure 4.6 Ultimate Stress vs. Current in SS304

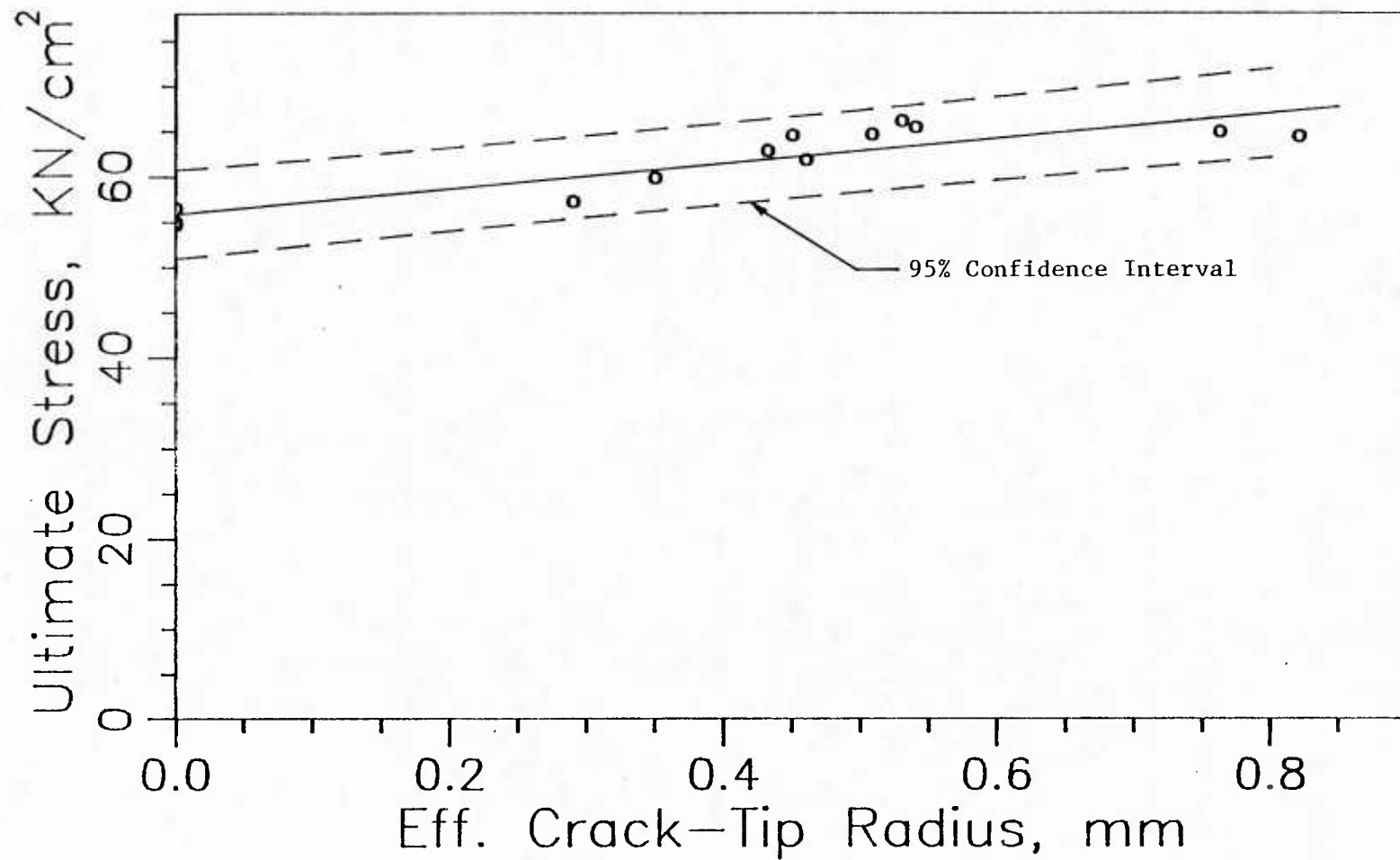


Figure 4.7 Ultimate Stress vs. Effective Crack-Tip Radius in SS304

In Figures 4.6 and 4.7 the ultimate stress is given as a function of the applied current and effective crack-tip radius respectively. Ultimate stress is computed by dividing the specimen's maximum load resistance by the remaining cross sectional area (net section). Direct linear regression is used to determine the mathematical relationship between these quantities. Considerable scatter is apparent in the applied current data. However, greater consistency is shown in the data of ultimate stress versus crack radius. The correlation coefficients are 0.61 and 0.89, respectively.

In addition, a 95% confidence interval is established for the last two graphs using the procedure of reference 25. These limits indicate that for a given current or crack radius, the ultimate stress of 95 out of every 100 specimens will lie in this range. Figures 4.6 and 4.7 show these confidence limits.

4.2.2 DRILLED HOLE SPECIMENS

As indicated earlier, this study recognizes that heating of the metal during electromagnetic blunting can have a significant effect on the properties of the material. With respect to the fracture resistance or ultimate strength of the material, this effect could be a positive or negative influence.

To examine the effects of electromagnetic heating on the remaining metal, a group of specimens are blunted by drilling a

hole as opposed to melting one. Both razor notched and fatigue cracked specimens are used with the hole being drilled at the tip in each case. The strips are then tested to failure load as before, and the ultimate stress on the net section is computed. In Figure 4.8 the ultimate stress of the razor notched samples is plotted versus hole diameter. The same graph for the fatigue cracked strips is given in Figure 4.9. Both of these figures indicate an increase in strength as the size of the hole used for blunting becomes larger.

Comparison of Figures 4.7 and 4.9 shows the relationships to be almost identical. Based on linear regression analysis of each set of data, the slope of the two curves is found to differ by only five percent. Furthermore, the disparity between y-intercepts is less than one half of one percent. The similarity between these two curves supports the notion that electromagnetic heating of the metal has very little or no influence on the static strength of the specimens. While the data seem to indicate no significant effect at present, a more thorough study of this area is recommended. Such a study should include a full metallurgical examination of the melted zone as previously mentioned.

4.2.3 SPECIAL EFFECTS

In addition to the main sequence of tests, several specimens are also tested to observe the influence of cooling and of a magnetic field during the blunting process. Results from experiments in these two areas are presented individually in the

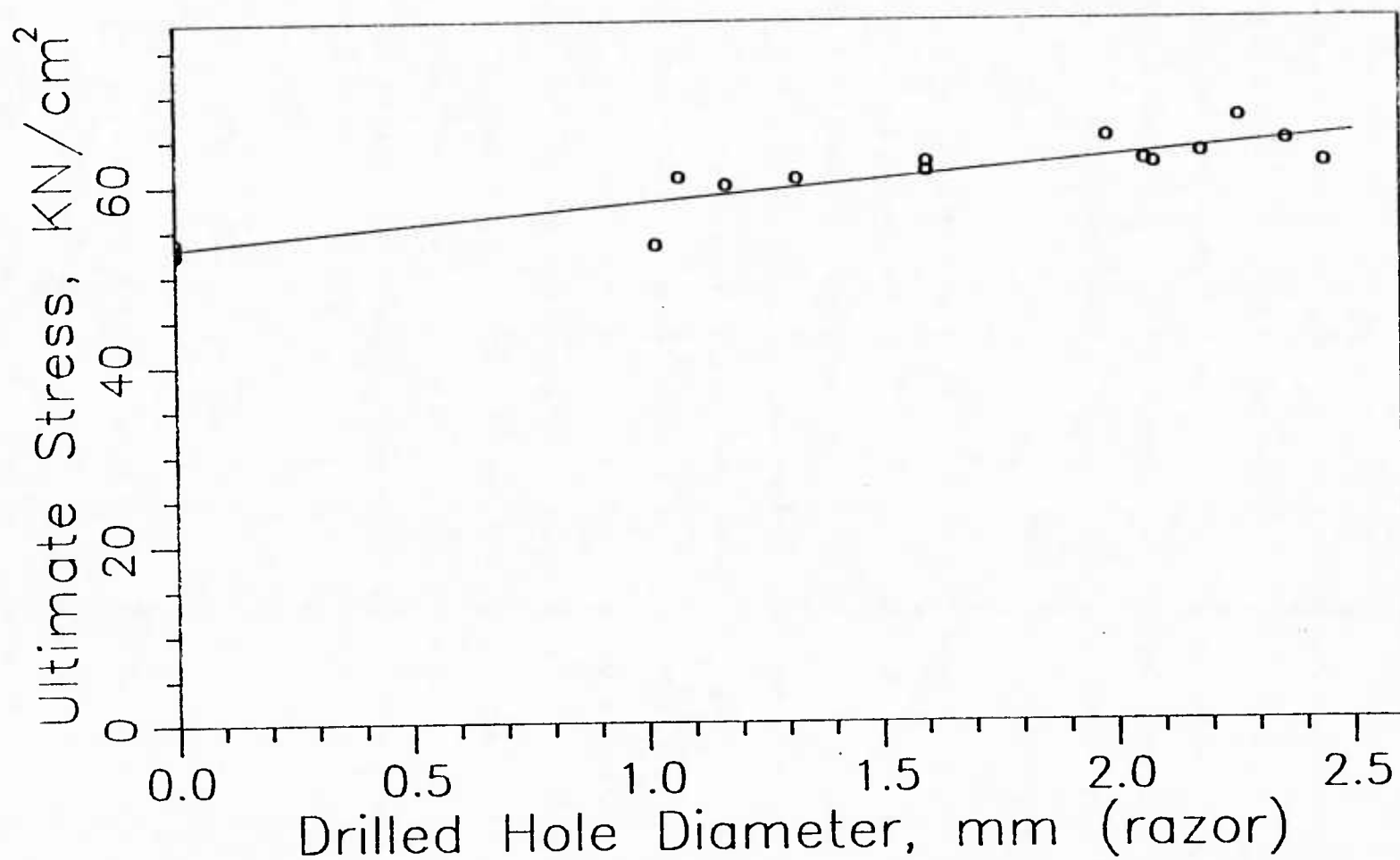


Figure 4.8 Ultimate Stress vs. Drilled Hole Size in SS304 Razor Notched Specimens

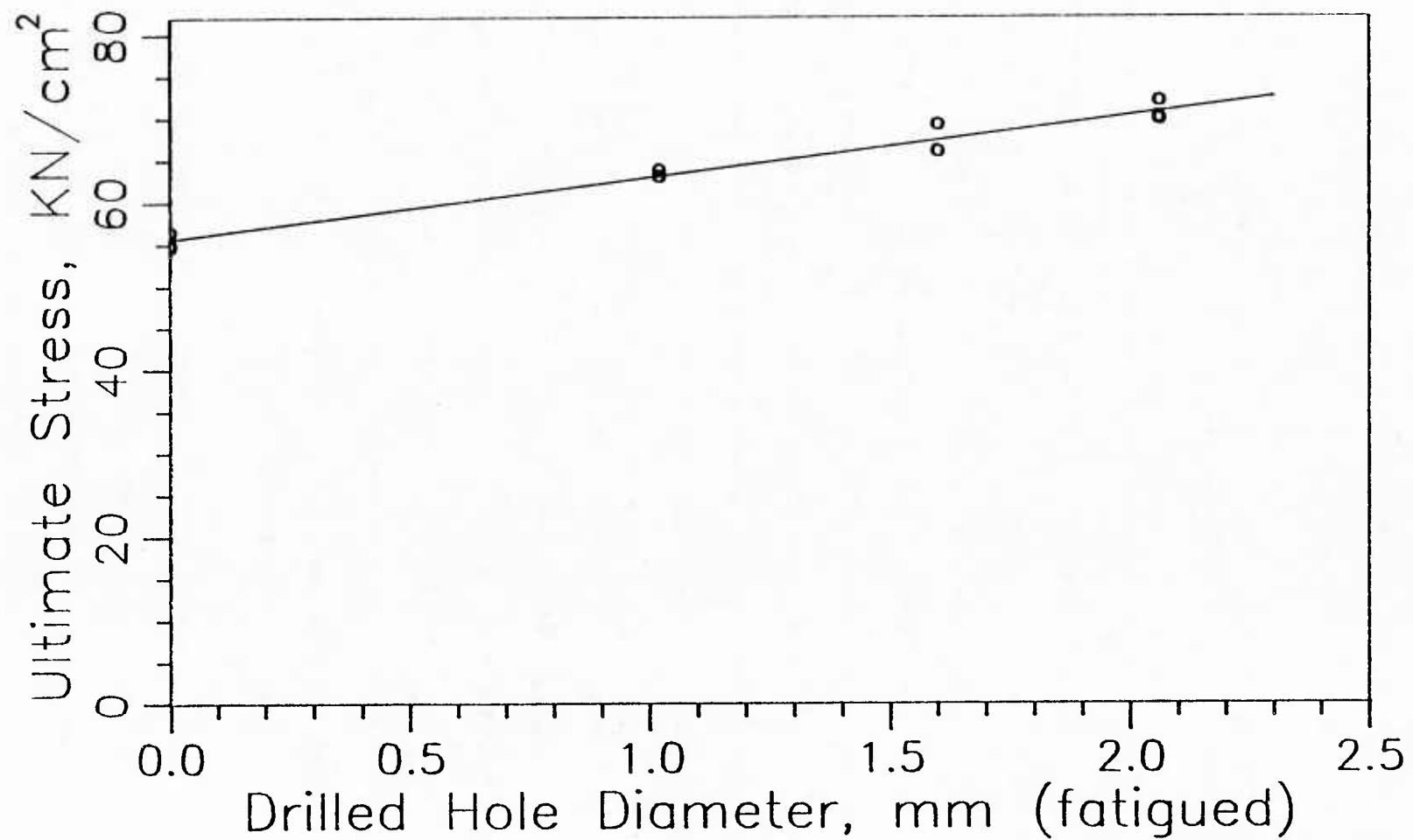


Figure 4.9 Ultimate Stress vs. Drilled Hole Size in SS304 Fatigue Cracked Specimens

two following two subsections. Figure 4.10 shows the data from these special tests superimposed on the curve from Figure 4.4 for reference.

4.2.3.1 External Magnetic Field

This group of tests is performed to investigate the effect of an external magnetic field on the displacement of the molten metal. Four specimens were exposed to a 7500 gauss magnetic field during application of the current pulse. The magnetic field is positioned perpendicular to each sample, and after two tests the direction of the field is completely reversed for the remaining two. Figure 4.10 indicates the direction of the applied magnetic field in each case. These two orientations are referred to as "direction 1" and "direction 2".

Results from these experiments are indicated in Figure 4.10. The magnetic field has a significant effect on the hole diameter. For these quantities the direction of the magnetic field is especially important. In the case of direction 1 the effective crack-tip radius is decreased about 40 percent as shown in Figure 4.10. The same quantity is increased about 80 percent by application of the magnetic field in direction 2.

On the other hand, the ultimate stress appears to be influenced by the magnetic field only in terms of the size of the hole produced. Testing of these strips for ultimate stress yields data which fall well within the 95 percent confidence limits of Figures 4.6 and 4.7.

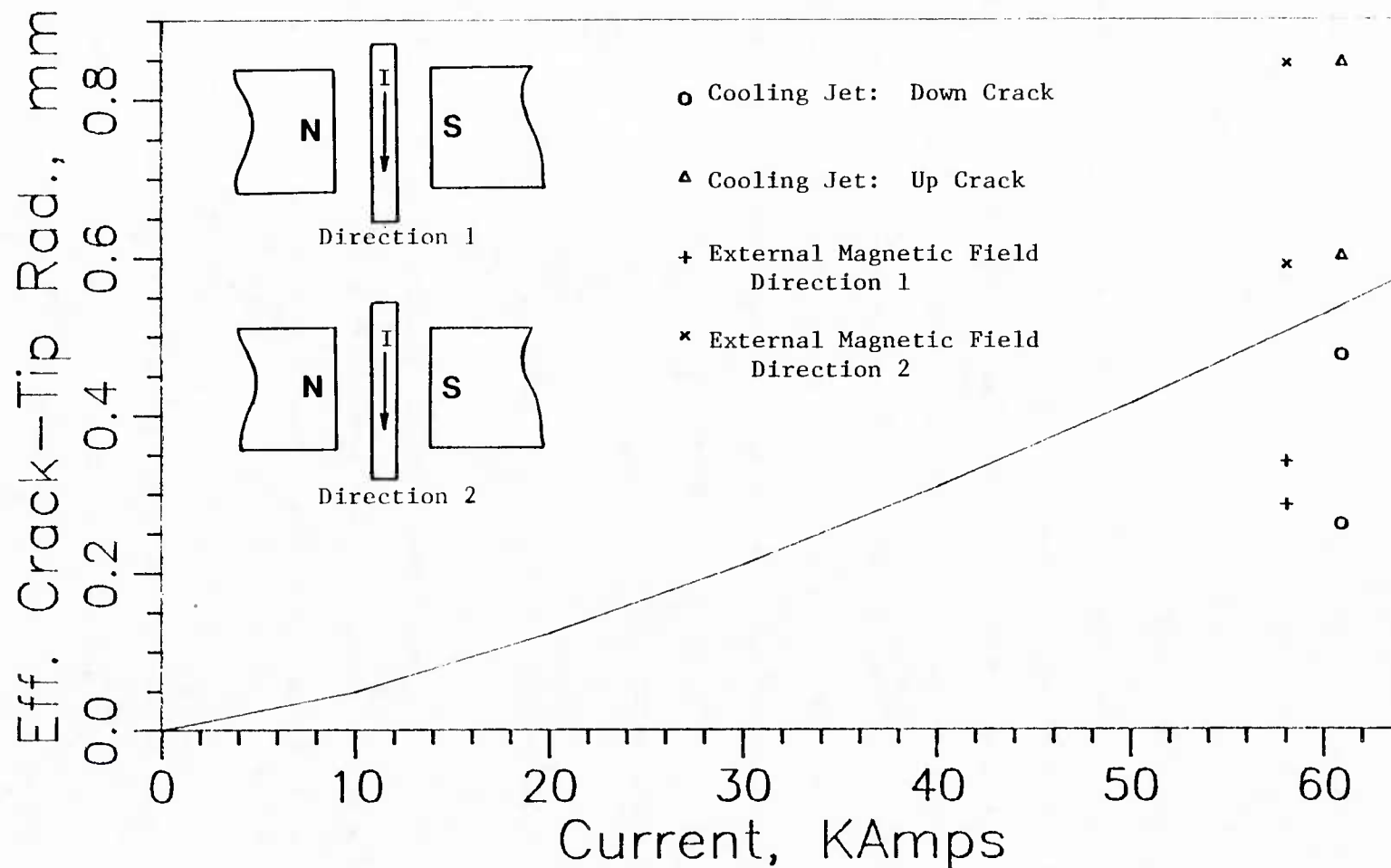


Figure 4.10 The Effect of an External Magnetic Field and a Cooling Jet on Effective Crack-Tip Radius in SS304

4.2.3.2 Nitrogen Gas Cooling

To observe the effect of cooling during the blunting process, a stream of nitrogen gas is directed along the crack. Two strips are tested with the gas jet running into the crack opening (down the crack) and one strip was tested with the jet focused on the uncracked edge (up the crack). The stream of gas had a predictable influence on the shape of the melted zone. Flow up the crack tends to elongate the hole and make it narrower, whereas the flow down the crack makes the hole rounded and squat and pushes it farther into the strip. In the data, the only noticeable effect of the gas jet is in the diameter of the hole. Figure 4.10 shows about a 60 percent reduction in effective crack-tip radius for flow up the crack and a 15 percent reduction for flow down the crack. The ultimate load data on these samples fit well with the previous tests.

4.2.4 DISCUSSION OF STAINLESS STEEL 304 TEST RESULTS

This section summarizes the results of the tests done on stainless steel 304. Furthermore, it describes the rationale used in selecting titanium as the next material to be studied.

In this study, some variability appears in the overall results of the blunting process. Wide scatter is considered to be typical in fatigue data. The relationships involving ultimate stress seem to show very little scatter while those entailing current or voltage show considerable variance.

For the fatigue cracked specimens one can see from Figure 4.7 that the greatest increase in strength realized is 19 percent. The razor notch specimens are found to exhibit similar behavior to that of the fatigue cracked specimens. This makes them valuable substitutes for the fatigued samples which are more difficult to obtain. However, the razor notches have their own significance for simulating stress risers in actual structures as well.

For the experiments with stainless steel, some of the conclusions regarding the drilled hole, magnetic field, and nitrogen cooled specimens have already been pointed out in the preceding discussion. These are summarized below.

Based on a comparison of drilled hole and melted hole results in section 4.2.2, the electromagnetic heating appears to have no appreciable effect on the ultimate strength. Also, section 4.2.3 points out that a magnetic field or a cooling jet affect the size of the hole and consequently the ultimate stress. However, these special effects have no effect on the ultimate strength independent of hole size.

The gain in load carrying capacity of the stainless steel strips suggests that even larger increases may be exhibited by other materials. In particular, a material for which the plastic zone around the crack tip is small is of interest because the electromagnetic blunting process may actually eliminate the plastic zone. If the area of plastification is smaller than the melted hole, then all of the yielded material would be removed from the specimen by blunting.

The concept of a small plastic zone can be examined further by considering the formulas available for computing plastic zone size. These expressions are of the general form:

$$p = n \left(\frac{K}{\sigma_y} \right)^2 \quad (4-1)$$

in which p is the plastic zone size, K is the stress intensity factor, σ_y is the yield strength of the material, and n is a constant. Various values of n have been proposed by different researchers. Hahn and Rosenfield [30] suggest that n be taken as $\pi/8$.

The accuracy of p as a true measure of the plastic zone size is questionable. Many factors such as work hardening and large strain effects are not included in these simple models [13]. Calculation of the plastic zone size is considered again in Section 5.3.1 where it is used to distinguish between large and small-scale yielding.

For this part of the study, Equation (4-1) is valuable for comparing the yielding behavior in different materials. Specifically it can be used to predict the type of material in which the plastification is small in the vicinity of the crack tip. Figure 4.11 shows this relationship plotted for a range of plastic zone sizes. One can easily see that the yielded region will be small in a situation involving a high yield strength and a low stress intensity factor.

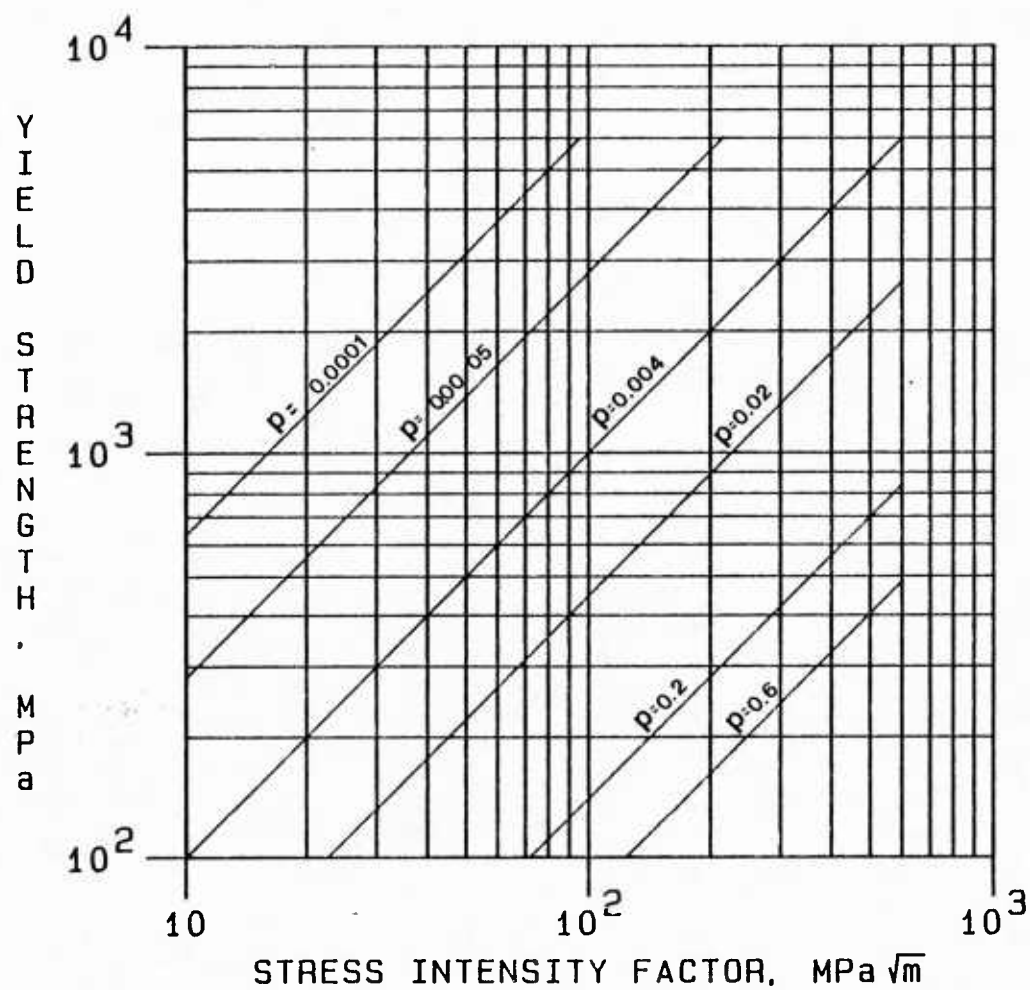


Figure 4.11 Plastic Zone Size, p , as a Function of Stress Intensity Factor, K , and Yield Strength, σ_y , in Plane Stress

Clearly, to obtain a small plastic zone, a material with a high yield strength is desirable. However, a similar generalization is not so straightforward in the case of the stress intensity factor. The reason is the stress intensity factor is not solely a material property in the case of the test specimens. Nevertheless, for the purposes of drawing conclusions, the critical stress intensity factor may be used for K in equation (4-1). A more detailed discussion of critical stress intensity factors as they apply to the test strips is presented in Sections 2.1.3 and 5.3. To summarize, a material with a high yield strength and a low critical stress intensity factor is desired for the zone of yielding to be small in the vicinity of the crack tip.

The type of properties of interest here are exhibited by brittle materials. In metals of this type, little yielding occurs prior to material separation because the yield stress is very near to the ultimate stress.

With these ideas in mind the titanium alloy Ti-6Al-4V is chosen. This metal has an ultimate stress of 895 MPa and a yield stress of 825 MPa [19]. The corresponding values for stainless steel are 550 MPa and 310 MPa [19], respectively. The titanium has a 63 percent higher ratio of yield to ultimate stress.

The next section reports on the tests done on Ti-6Al-4V.

4.3 TITANIUM ALLOY (Ti-6Al-4V) SPECIMENS

The results of testing done on Ti-6Al-4V is the topic of this section. Unlike the stainless steel specimens, the titanium specimens are not milled down on one side. Figure 4.1(b) shows the geometry used. The thickness of the material is 1.4 mm.

Three series of titanium specimens are blunted. First, a pair of razor notched samples without cracks are blunted. Next, several strips containing fatigue cracks are put through the process unloaded. These specimens show that, when the crack is not sufficiently open, holes occur along the crack rather than at the tip. This is caused by the current jumping across the crack in certain places. A third series of specimens are then blunted while under load to open the crack to avoid the problem of incomplete hole formation. This problem is especially evident in brittle materials such as titanium because the small amount of plastic deformation causes the crack to be tight when unloaded. Figure 4.1(b) does not show the holes used to attach the capacitance bank leads at the ends of the unloaded samples. Such holes are not required in the case of the loaded strips because different grips are used in this situation.

Only two razor notched specimens of titanium are blunted. The purpose of these is to provide an introduction to the effect of the electromagnetic process on the titanium alloy. A 5 kV

charge is applied to both these samples. The ultimate stress of these two specimens is fifty percent greater than the ultimate stress of the two unblunted specimens which are tested.

Experimentation continued with the fatigue cracked strips blunted while unloaded and then with the cracked strips blunted while loaded. Individual attention is given to each of these two groups.

4.3.1 UNLOADED FATIGUE CRACKED SPECIMENS

Using the same procedure as used for stainless steel, a group of unloaded titanium specimens containing fatigue cracks are blunted. The melted area in these tests suggests that better holes might be obtained by placing the strips in tension.

Results from this series are presented in Figures 4.12, 4.13, and 4.14. In the first of these figures, the effective crack-tip radius is plotted versus current. A linear regression analysis of this data is shown by the solid line in this figure which has a correlation coefficient of 0.91.

Figure 4.13 expresses the relationship between ultimate stress on the net section and the applied current. The variability of these results is evident in this figure and in the low correlation coefficient of 0.50 for the linear regression curve.

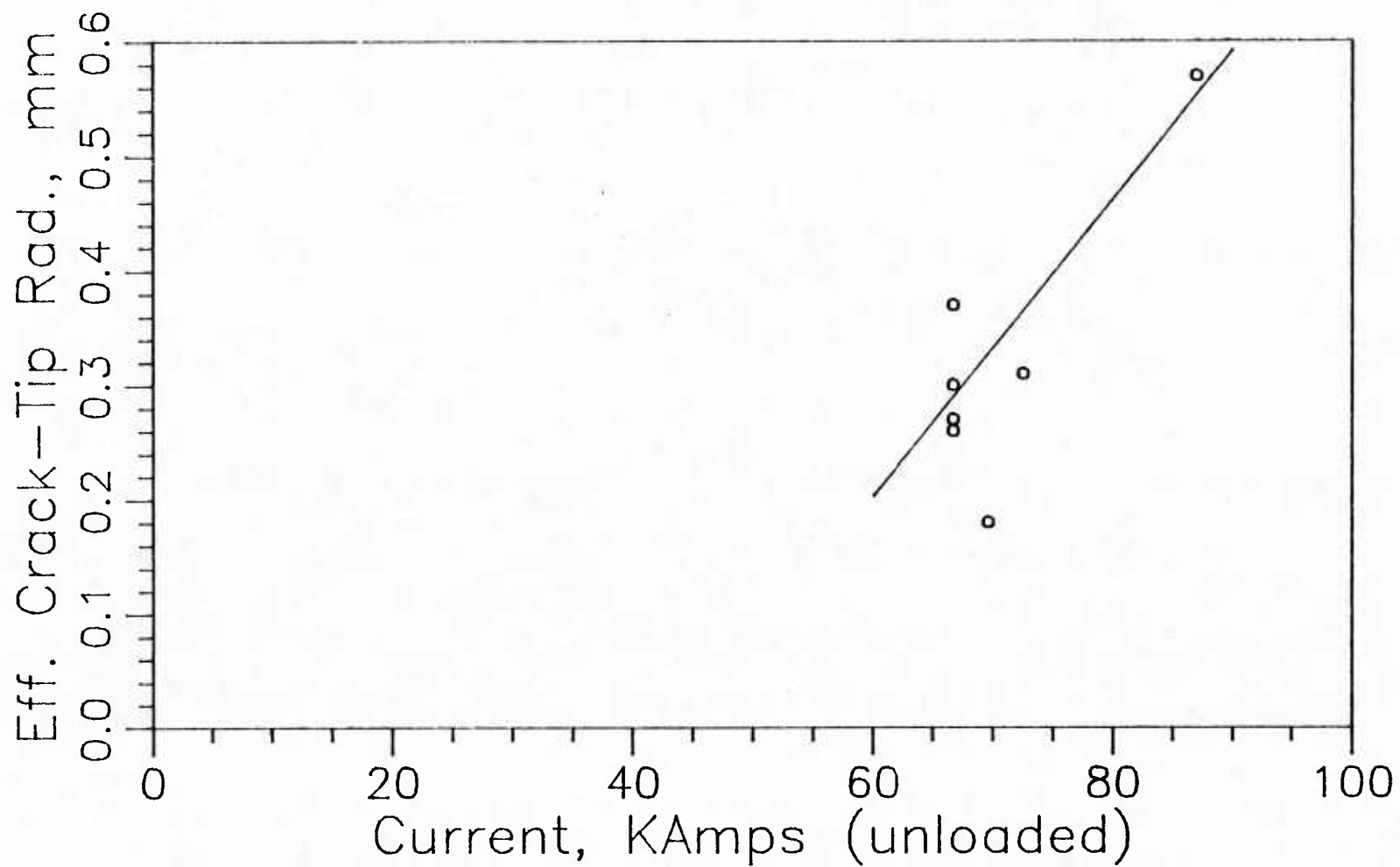


Figure 4.12 Effective Crack-Tip Radius vs. Applied Current in Unloaded Ti-6Al-4V

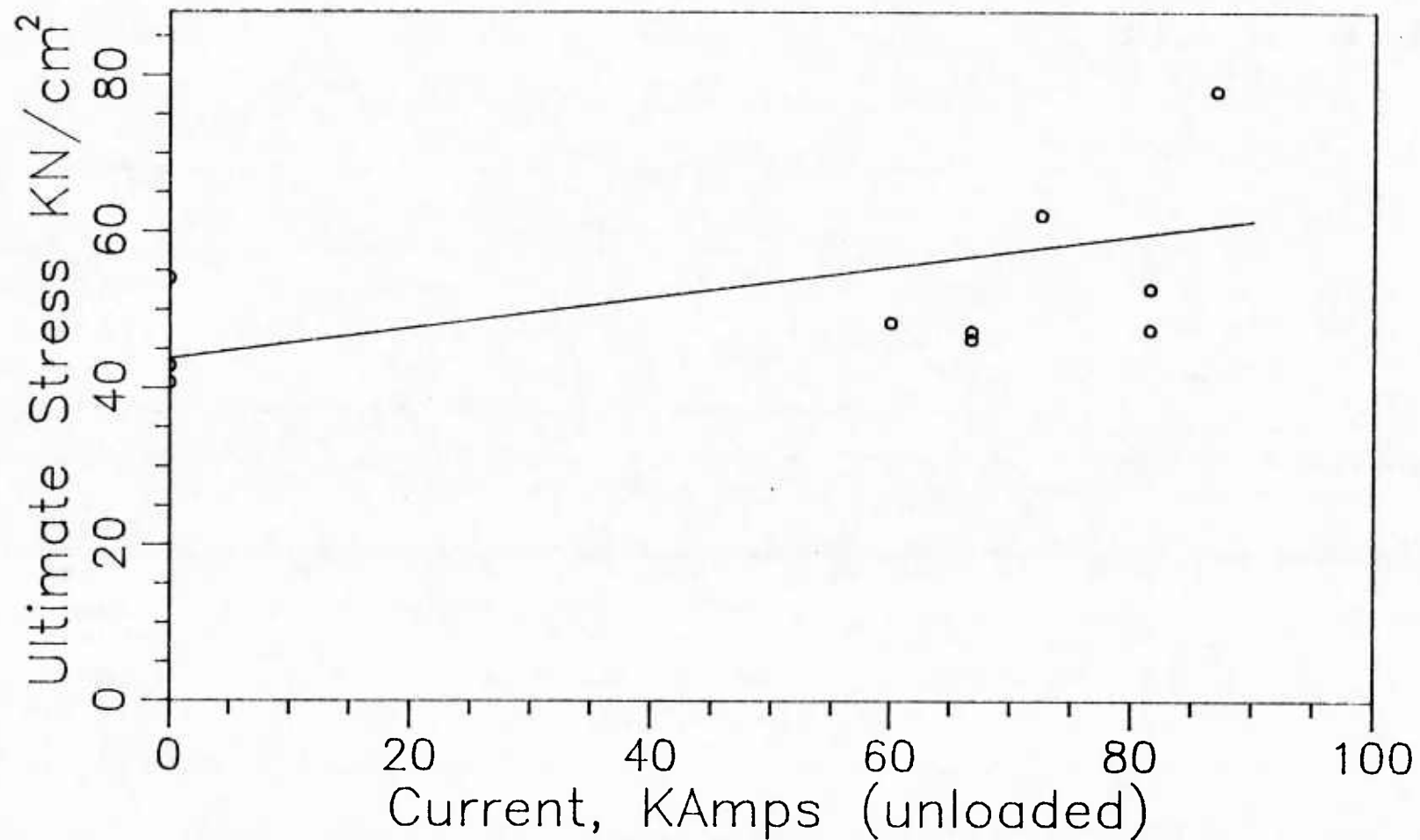


Figure 4.13 Ultimate Stress vs. Applied Current in Unloaded Ti-6Al-4V

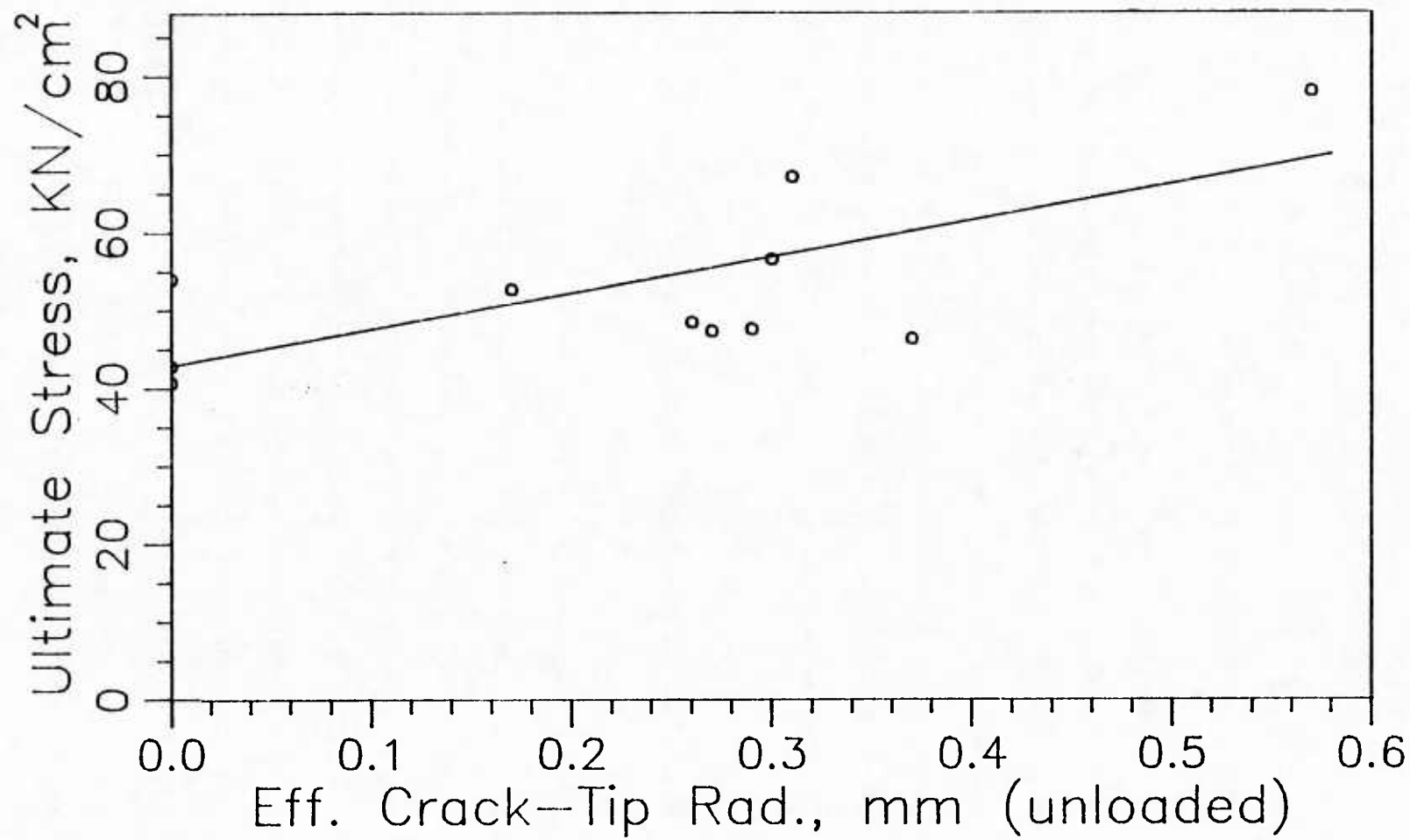


Figure 4.14 Ultimate Stress vs. Effective Crack-Tip Radius in Unloaded Ti-6Al-4V

Lastly, in Figure 4.14 the ultimate stress on the net section is plotted as a function of crack radius. The linear regression curve has a correlation coefficient of 0.78 which shows that some scatter is apparent in the data. The largest increase in strength exhibited by any one of these samples is over 70 percent.

Collecting a large number of accurate data points was difficult with this group of specimens because of the incomplete hole formation problem described in section 4.1.2. In many cases the melting occurred along the crack rather than at the crack tip which made the samples unusable. However, by opening the crack under tensile load the melting was forced to occur at the tip. The next section presents the data compiled using this technique.

4.3.2 TENSILE LOADED FATIGUE CRACKED SPECIMENS

As mentioned at the end of the last section, the blunting procedure developed here is a direct result of the difficulties experienced with the last set of titanium samples. Application of the current pulse to a sample in the loading machine requires special grips to be designed and manufactured. Insulation of the loading machine is also required.

Two approaches are taken with this group of specimens. In the first case the size of the current pulse is held constant while the applied load on the specimen is varied. By examining the holes from this set of tests, a value of applied load is found

which consistently forces the hole to occur at the crack tip. The value selected is 700 pounds. With the load fixed at this value, a second set of results is obtained over a range of applied voltages. The outcome of the first series of tests is depicted in Figures 4.15, 4.16, and 4.17. Each figure contains a solid line representing the results of a linear regression analysis for that data.

In Figure 4.15 the effective crack-tip radius is plotted as a function of applied load. The correlation coefficient is 0.86 which indicates a reasonable degree of consistency in this relationship. To produce a significant blunting effect a minimum hole size is necessary. Hence, one can see from Figure 4.15 that an applied load of at least 700 pounds is required to create a reasonably sized hole of radius 0.3 mm. A value of 700 lb is also suggested by general visual comparison of the blunted regions in the samples themselves.

The strips were tested to ultimate load as before. Figure 4.16 shows the variation of ultimate stress with applied load during the melting. Ultimate stress is plotted as a function of crack radius in Figure 4.17. Some scatter is evidenced in each case and the correlation coefficients are 0.61 and 0.80, respectively.

All specimens in the second group are blunted while under an applied load of 700 pounds. The size of the applied voltage ranges from 2.5 to 5.0 kV. In Figure 4.18 the graph of crack

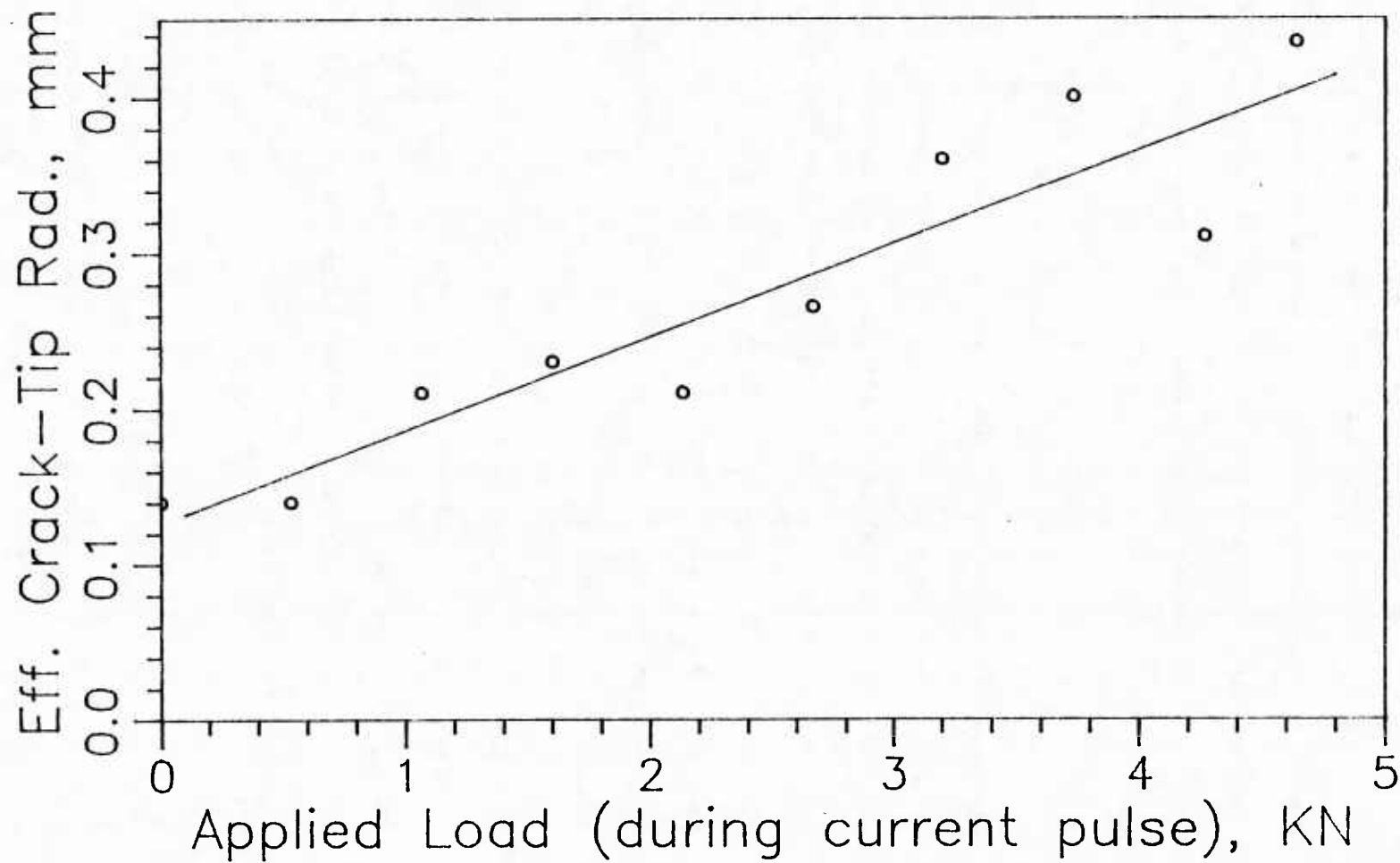


Figure 4.15 Effective Crack-Tip Radius vs. Applied Load in Ti-6Al-4V at 4KV

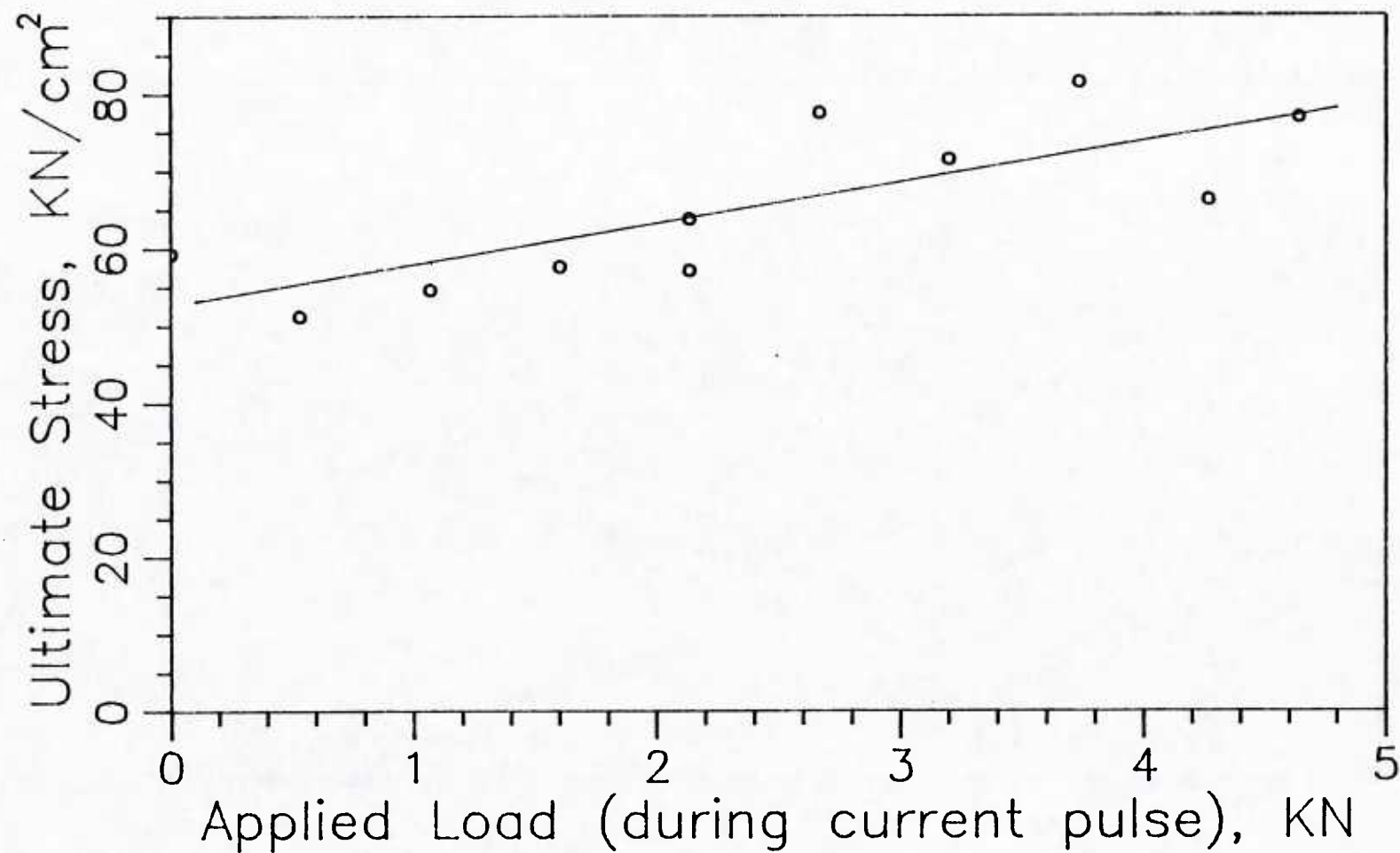


Figure 4.16 Ultimate Stress vs. Applied Load During Current Pulse in Ti-6Al-4V at 4 KV

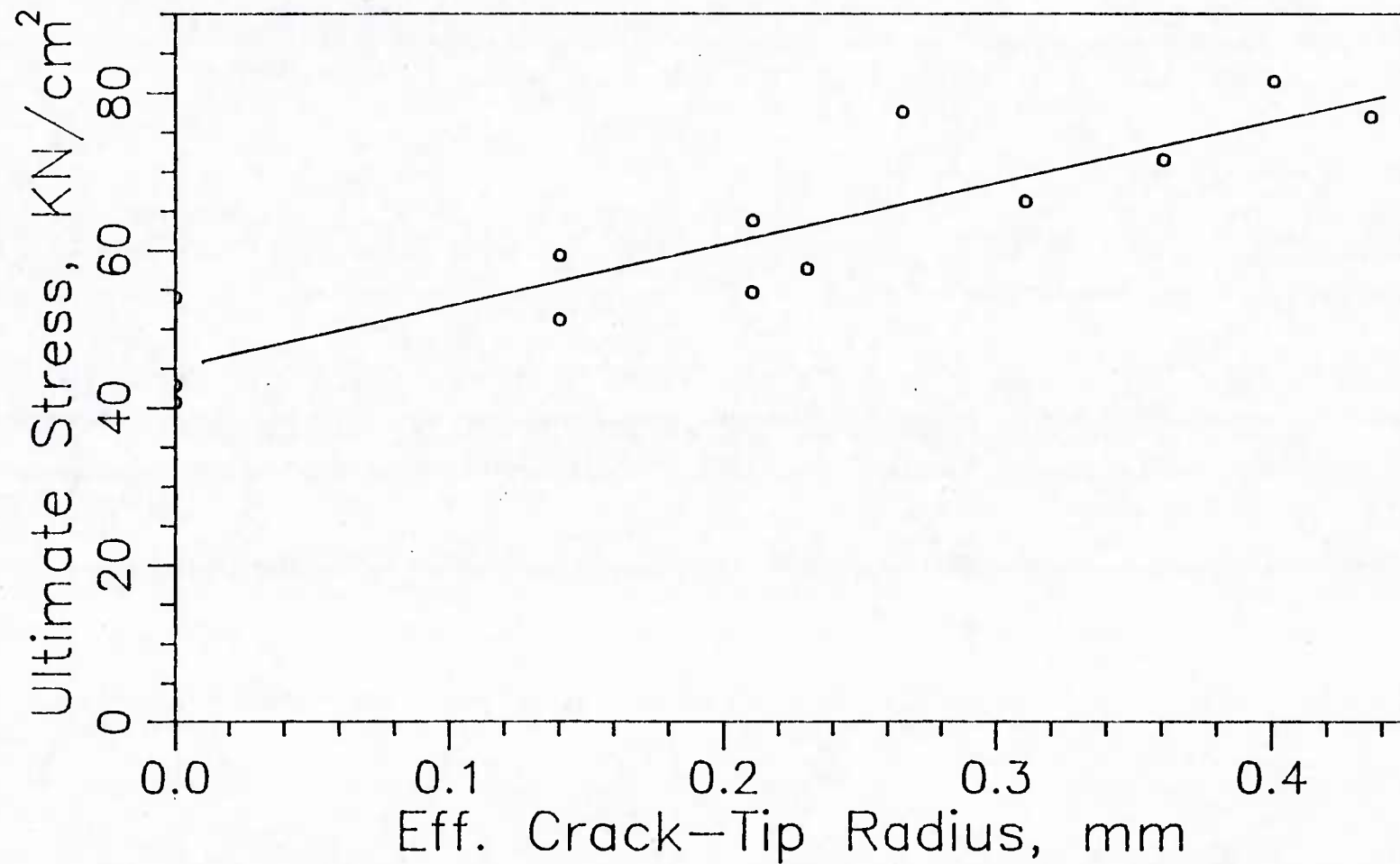


Figure 4.17 Ultimate Stress vs. Effective Crack-Tip Radius in Ti-6Al-4V Specimens Under Varied Load at 4 KV

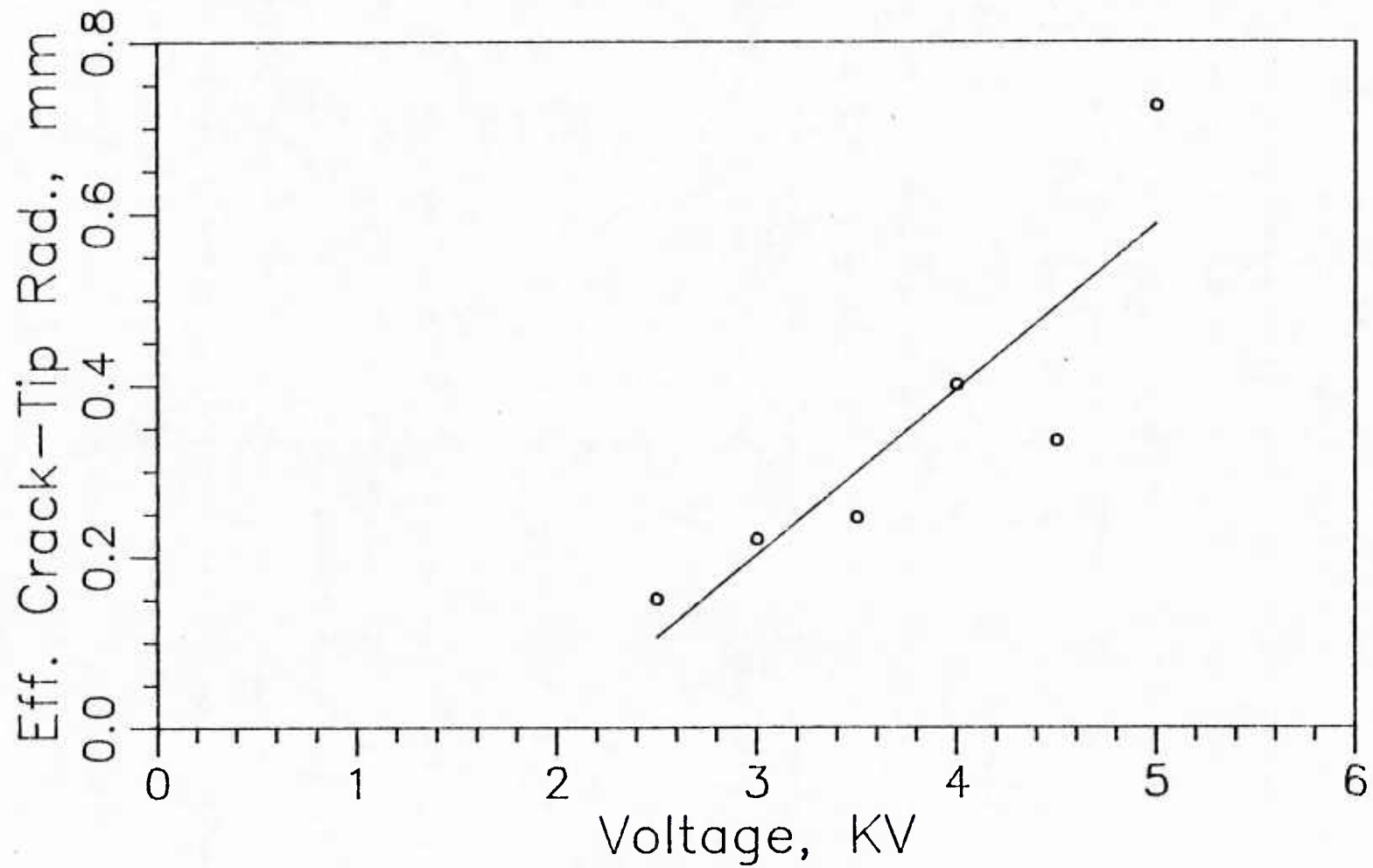


Figure 4.18 Effective Crack-Tip Radius vs. Voltage in Ti-6Al-4V Under a Constant 700 lb Load

radius versus applied voltage is shown. Ultimate strength tests are performed on these strips and the relationship between ultimate stress on the net section and effective crack-tip radius is shown in Figure 4.19. Both of these Figures show linear regression curves for which the correlation coefficients are 0.77 and 0.31, respectively. A large amount of scatter resulted in especially poor agreement in the second figure. Additional sampling points are necessary to define this relationship more accurately.

From Figure 4.17 one can see that a maximum increase in ultimate strength of over 78 percent is possible by loading the specimens. The second series of loaded specimens also indicates an increase in ultimate stress of over 78 percent as shown in Figure 4.19.

4.3.3 DISCUSSION OF Ti-6Al-4V TEST RESULTS

This section concludes the chapter by pointing out the highlights in the titanium data and comparing these results to the results from stainless steel.

Some of the conclusions from the titanium experiments have already been drawn in the preceding discussion. For example, the need for a 700 lb tensile load on the titanium specimens to force melting to occur at the crack tip was discussed in section 4.3.2.

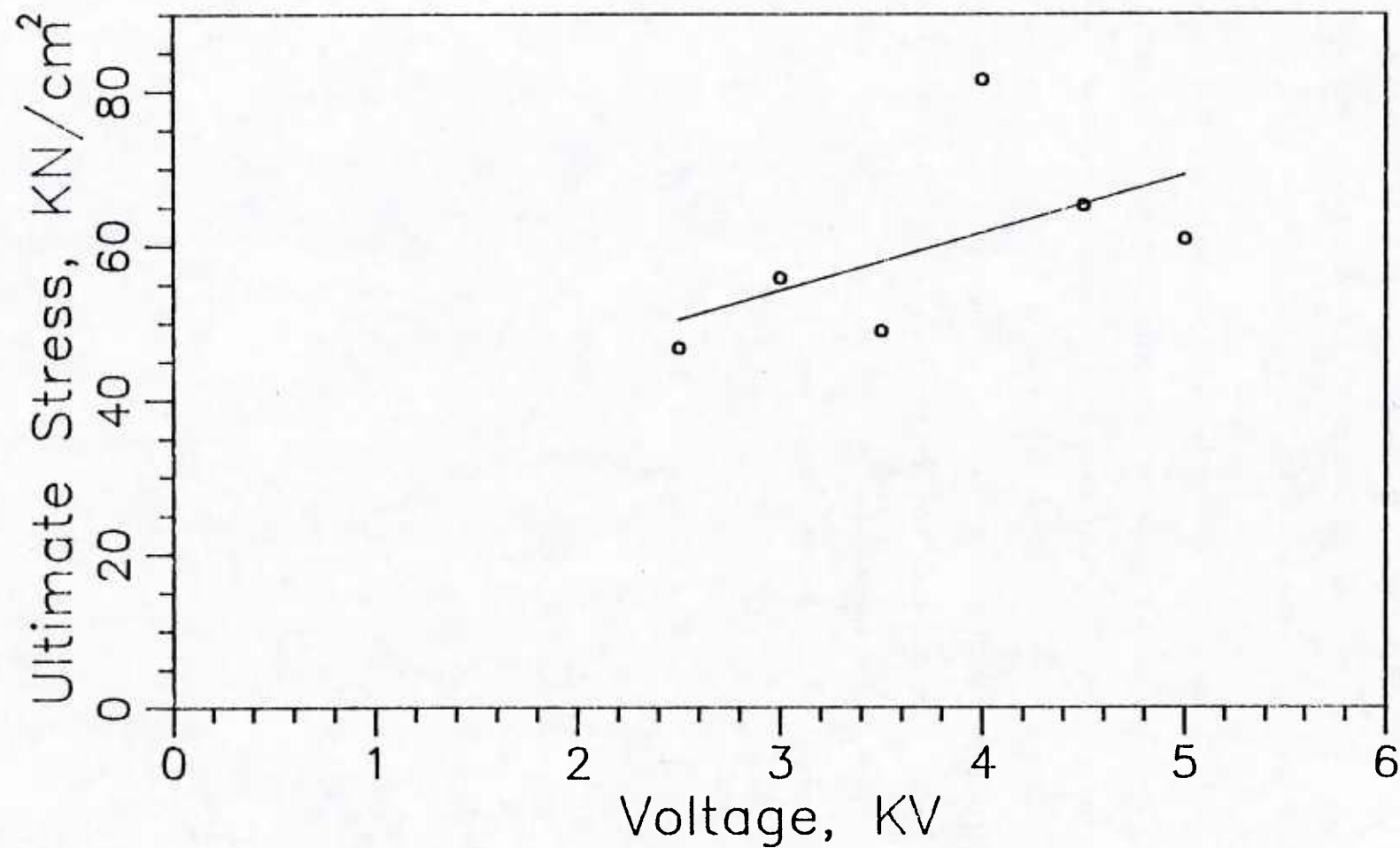


Figure 4.19 Ultimate Stress vs. Voltage in Ti-6Al-4V Under a Constant 700 lb Load

To summarize for the titanium, Figure 4.14 shows a maximum increase in ultimate stress of 70 percent in the unloaded titanium samples. The largest improvement in the loaded specimens is over 78 percent as indicated by Figure 4.17.

Tests confirm the notion that a brittle material such as Ti-6Al-4V will show greater gains in strength than a ductile material such as stainless steel 304. As a comparison, the linear regression curves for stainless steel, unloaded titanium, and loaded titanium are shown together in Figure 4.20. Clearly, the curves for titanium are steeper than that of stainless steel. The slope of the loaded titanium samples is over 460 percent greater than the slope for stainless steel 304.

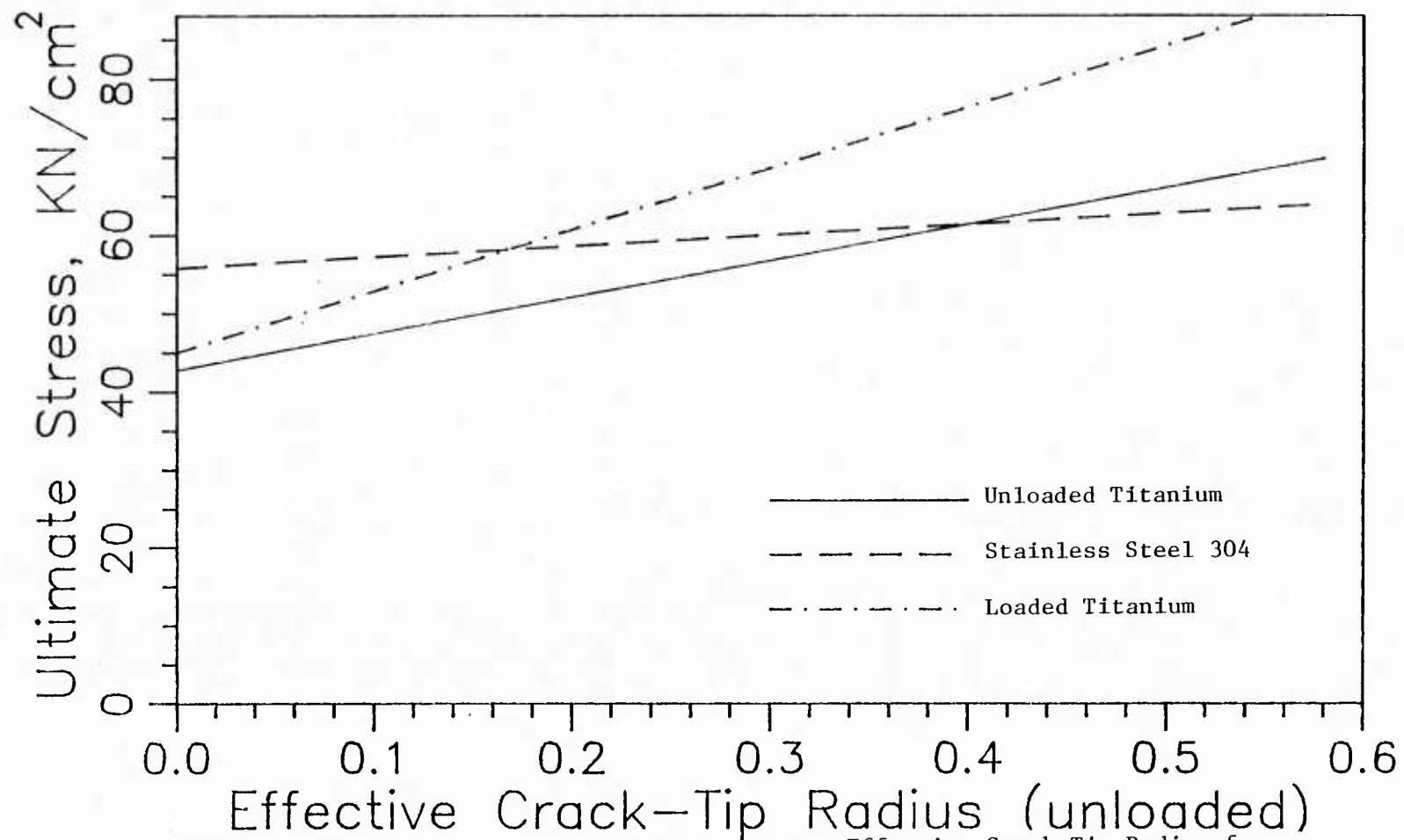


Figure 4.20 Comparison of Ultimate Stress vs. Effective Crack-Tip Radius for Stainless Steel 304, Unloaded Ti-6Al-4V, and Loaded Ti-6Al-4V

CHAPTER 5

STRESS ANALYSIS OF TEST SPECIMENS

The state of stress in the electromagnetically blunted specimens is examined in this chapter. Stress concentration solutions and finite element analysis are used to study the stresses. An equivalent stress intensity factor approach is then applied to the results of Chapter 4 to express that data in a new format.

5.1 STRESS CONCENTRATION FACTORS

The value of stress concentration factors in the stress analysis of nonsingular disturbances was pointed out in section 2.1. Although stress concentration factors cannot be utilized to

describe the crack situation, they are applied to the blunted case. They also are useful in section 5.3 in extending the stress intensity factor approach to the blunted geometry.

Stress concentration factors can be determined in several ways. Results of photoelastic studies and analytical solutions are considered in this study. Values for many different geometries are widely tabulated. Solutions, however, have not been developed for the configuration shown in Figure 2.1(a). Based on the earlier rationalization, the geometry in Figure 2.1(c) may be used in place of the actual geometry without a significant loss in accuracy.

Testing the specimens discussed in Chapter 4 for ultimate capacity involves application of a uniform load at the ends of the strip. This condition is equivalent to the situation shown in Figure 5.1(c). Solutions for this geometry are available for a load applied along the centerline of the remaining area, Figure 5.1(a), but not for a load applied along the centerline of the entire strip. To develop a useable analysis, therefore, it is necessary to superimpose the solution for a load along the specimen centerline, Figure 5.1(a), and the solution for an applied end moment, Figure 5.1(b). The end moment is the product of the load and e , the eccentricity of this load from the centerline of the net section.

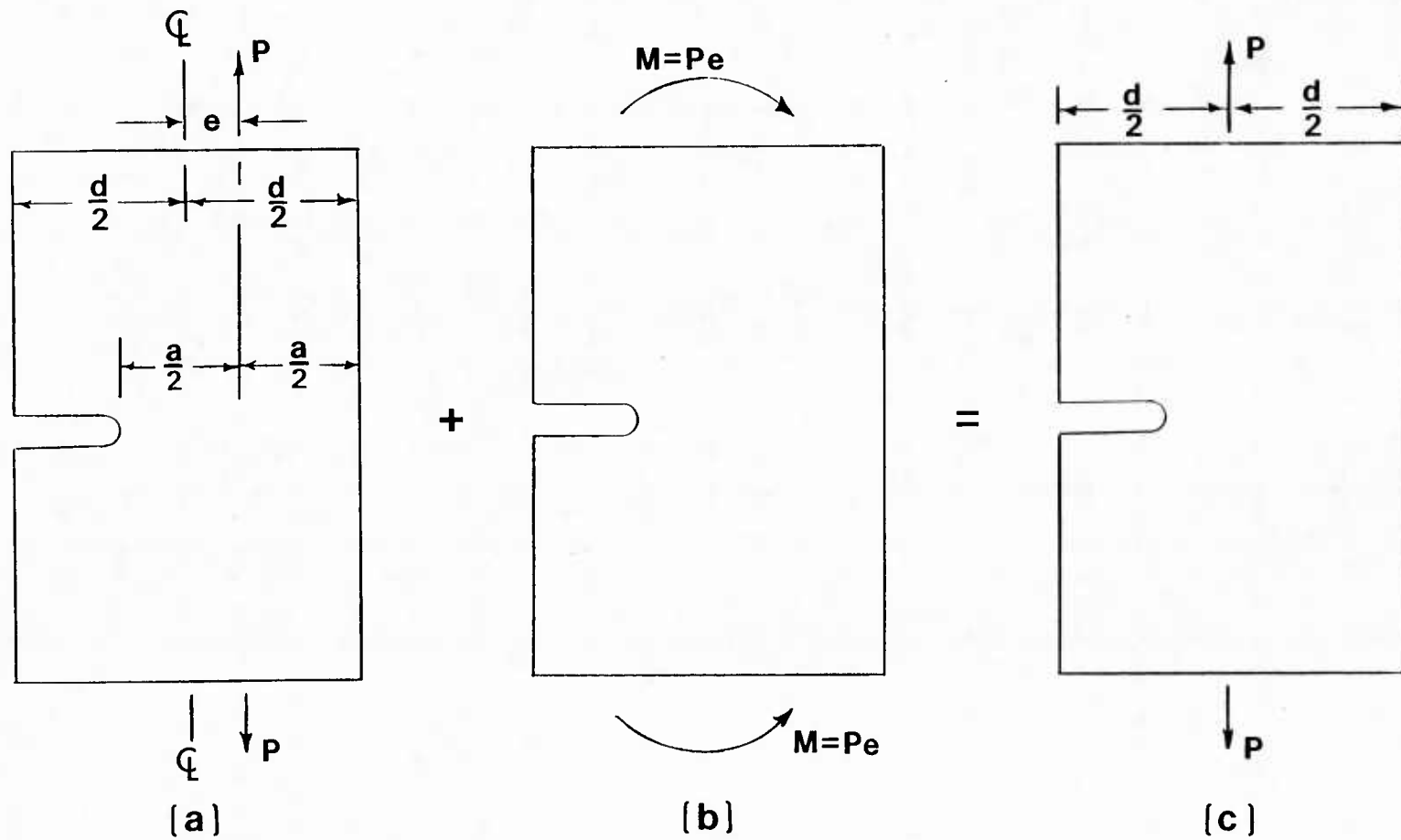


Figure 5.1 Superposition of Stress Concentration Factor Solutions for a Flat Test Specimen with a Single Edge Notch

For a concentrated load applied along the centerline of the net section, Neuber [3] presents an analytical solution for the stress concentration at a hyperbolic or elliptical notch. These solutions are only an approximation for the U shaped notch under study. Photoelastic studies of the circular notch were conducted by Cole and Brown [26]. These results are used to determine the stress concentration factors for the configuration in Figure 5.1(a).

In general, the configuration tested by Cole and Brown is the same as the problem at hand. However, the range of sizes considered in that study does not cover completely the range of samples considered in the experiments of Chapter 4. Therefore, by performing a logarithmic regression of Cole and Brown's results, the analysis was extended to include the necessary geometries. The curve which was developed is shown in Figure 5.2.

To complete the superposition of Figure 5.1, the stress concentration factors for an end moment applied to a strip containing a U-notch are required. Peterson [27] summarizes the results of a photoelastic analysis of this configuration conducted by Leven and Frocht [28]. As before, the range of sizes considered in the study does not cover all the possible sizes of test pieces in Chapter 4. Figure 5.3 shows the curve obtained from a logarithmic regression used to extend the analysis to the required geometries.

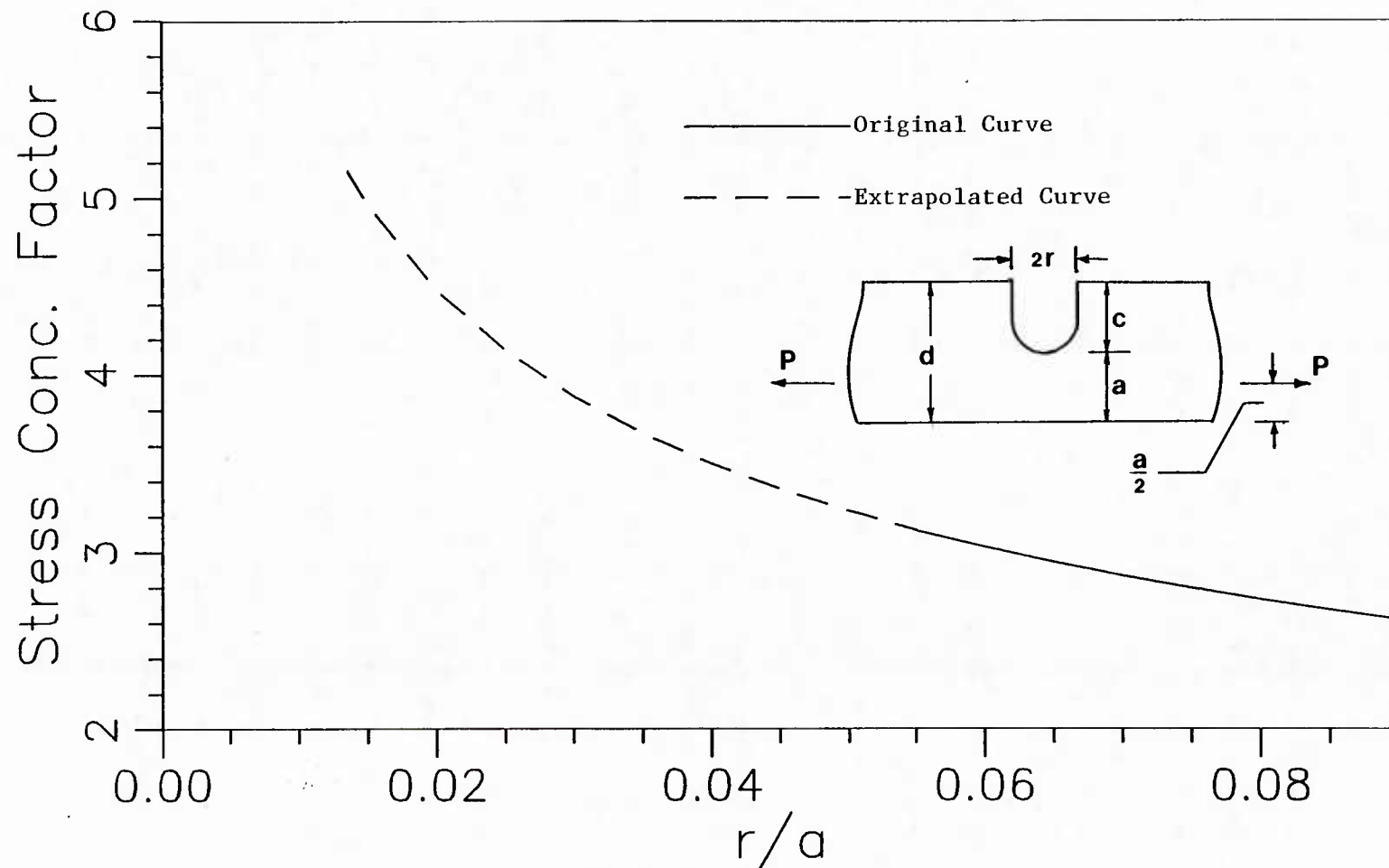


Figure 5.2 Logarithmic Extrapolation of Stress Concentration Factor vs. r/a for a Flat Tension Bar with a U-Notch (Cole and Brown)

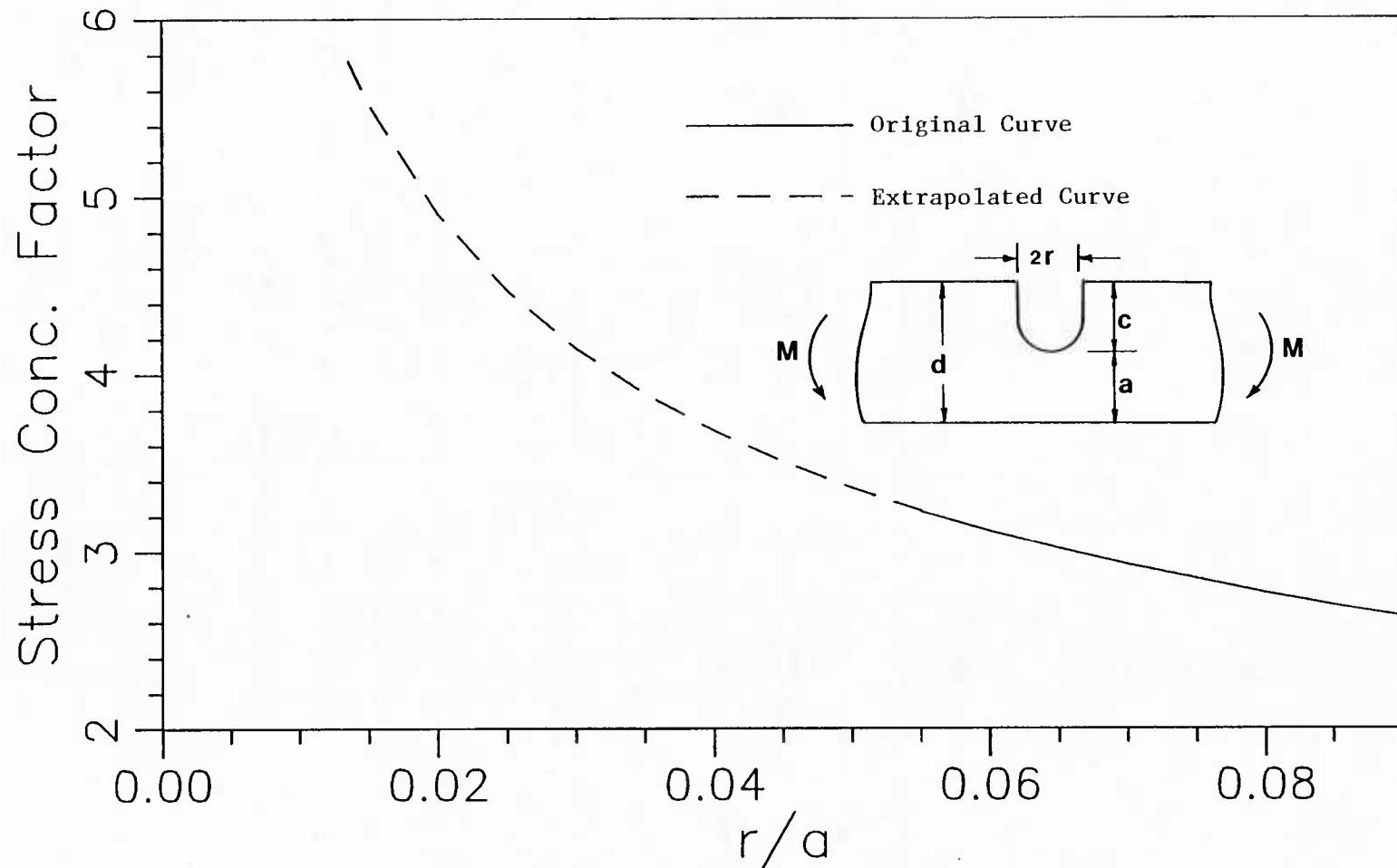


Figure 5.3 Logarithmic Extrapolation of Stress Concentration Factor vs. r/a for Bending of a Plate with a U-Notch (Leven and Frocht)

To combine the stress concentration factors for configurations 5.1(a) and 5.1(b), the maximum stress in each case at the tip of the notch is summed. The maximum stress for case (a), $(\sigma_a)_{\max}$, is expressed in terms of its stress concentration factor K_a and the nominal stress on the net section:

$$(\sigma_a)_{\max} = K_a \sigma_{\text{nom}} = K_a \frac{P}{ha} \quad (5-1)$$

in which P is the concentrated load, h is the thickness, and a is the width of the strip at the narrowest section. The dimensions are shown in Figure 5.1. For case (b) the corresponding expression for the maximum stress, $(\sigma_b)_{\max}$, is based on the peak stress considering a moment, M , applied to the net section:

$$(\sigma_b)_{\max} = K_b \sigma_{\text{nom}} = K_b \frac{6M}{ha^2} = \frac{6Pe}{ha^2} \quad (5-2)$$

in which K_b is the stress concentration factor for configuration 5.1(b). The moment is taken as the product of the concentrated load, P , and the eccentricity, e . From the geometry of Figure 5.1 the eccentricity can be written as $(d-a)/2$.

Equations (5-1) and (5-2) are now added together to get an expression for the maximum stress in the desired situation, $(\sigma_c)_{\max}$. By substituting for e and rearranging, one has:

$$(\sigma_c)_{\max} = \frac{P}{ha} \left[K_a + K_b 3[(d/a) - 1] \right] \quad (5-3)$$

The next step is to substitute in the expressions for K_a and K_b which are obtained by logarithmic regression. These relationships are given in Figures 5.2 and 5.3. Furthermore, the peak stress is put in terms of a single stress concentration factor, K_c , by dividing by the nominal stress, P/ha :

$$K_c = \frac{(\sigma_c)_{\max}}{\sigma_{\text{nom}}} = [1.1074 (r/a)^{-0.357} + C(r/a)^{-0.414}] \quad (5-4)$$

in which

$$C = 2.91[(d/a) - 1] \quad (5-5)$$

Finally, equation (5-4) expresses the stress concentration at the end of a notch in a flat strip due to a concentrated load applied along the centerline of the full section. The concentration is given in terms of a stress concentration factor based on the nominal stress on the net section. A check on equation (5-4) is provided at the end of the next section when this approach is compared to the finite element method.

5.2 FINITE ELEMENT ANALYSIS

One virtue of the finite element method is its ability to analyze a variety of problems. In Chapter 3 the finite element method is used to compute electric currents, but in this section it is applied to the stress analysis of the test strips [29].

By taking advantage of the symmetry of the problem, the configuration to be analyzed is reduced to that shown in Figure 5.4. In particular, the important sizes to be considered are a , r , and d as shown in Figure 5.4. The width of the samples, d , is a constant, 19mm, and the other dimensions are expressed as ratios, a/d and r/d . To provide a comprehensive study, the full range of dimensions is taken from the specimens of Chapter 4. The upper and lower limits for a/d are found to be 14.44 and 11.97, while r/d ranges from 0.038 to 0.009. In each case, the range of ratios is covered by choosing the intermediate values shown in Table 5.1.

Three different aspects of the problem are used to summarize the analysis. First, in Figure 5.5, the variation of maximum stress, σ_y , along a radius at $\theta=0$ is shown for one representative geometry. In this case one can observe the stress gradients are very steep near the crack-tip. Similar distributions are found for other sizes. The stresses here are based on a uniformly applied load of unity as shown in Figure 5.4. Second, the tangential stress distribution around the circumference of the hole in each geometry is given in Figures 5.6, 5.7, 5.8, 5.9, and 5.10.

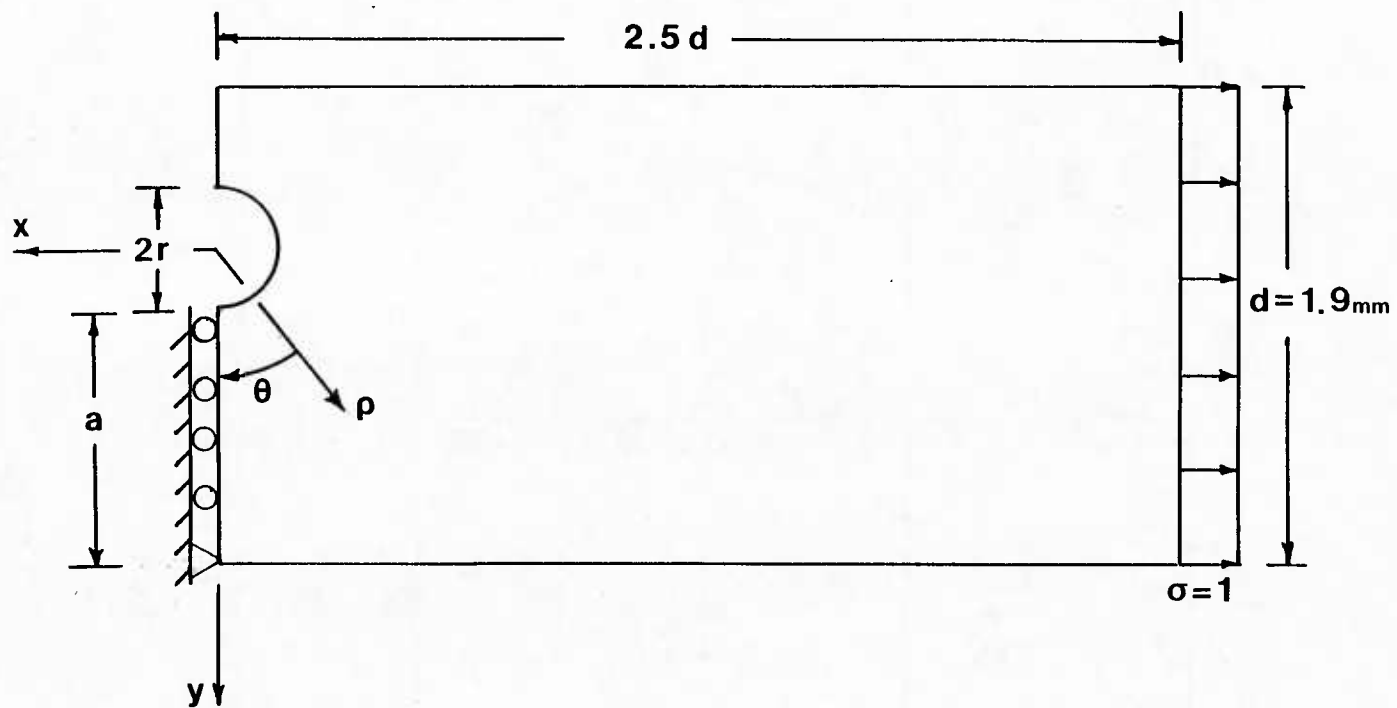


Figure 5.4 Test Specimen Configuration Used in Finite Element Stress Analysis

a/d	r/d
0.63	0.009
0.67	0.016
0.72	0.017
0.76	0.027
	0.038

Table 5.1 Representative Geometries for Finite Element
Stress Analysis of Blunted Crack Configuration

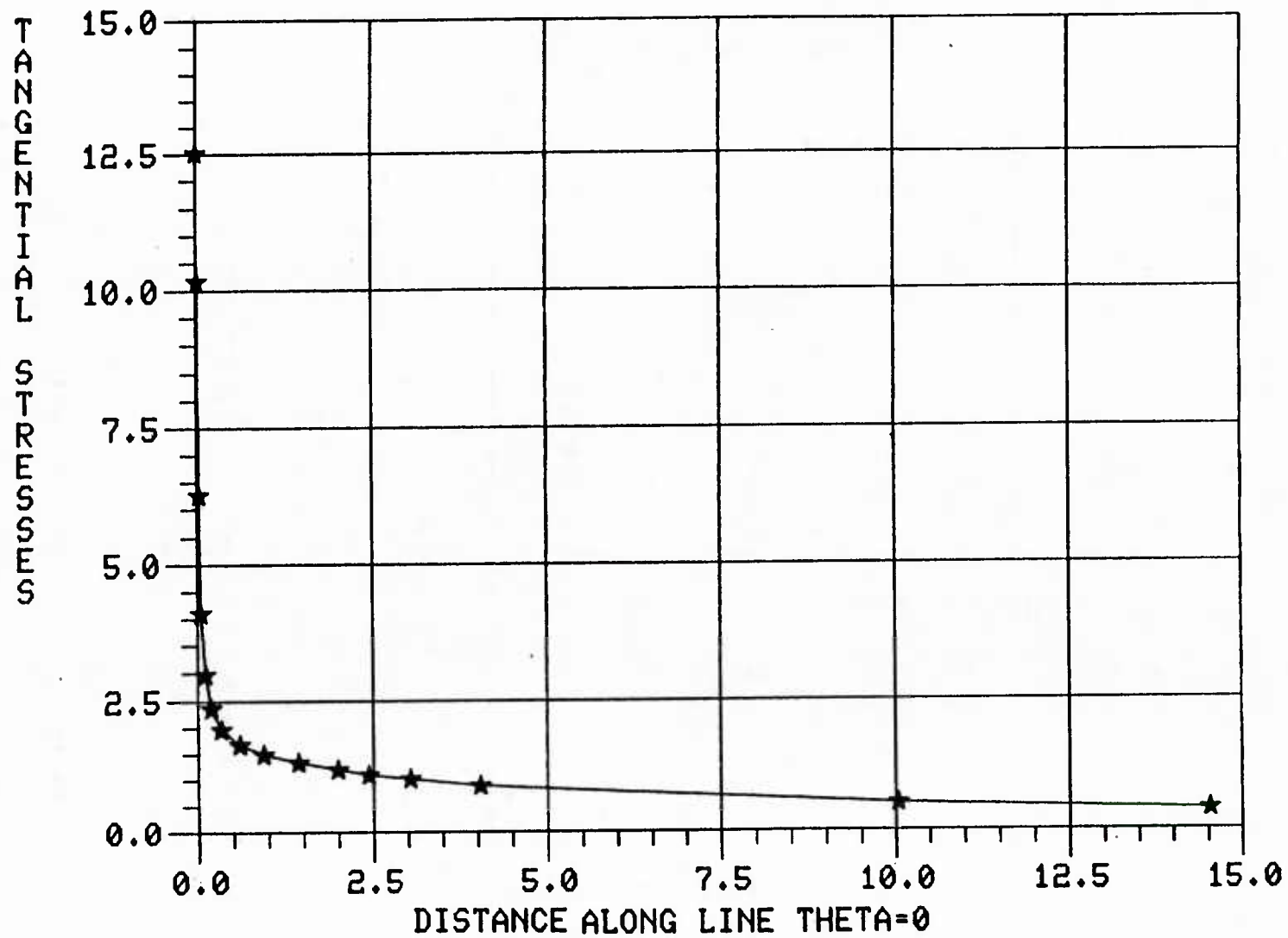


Figure 5.5 Variation of Maximum Normal Stress σ_y Along $\theta=0$, $r/d = .009$, $a/d = 0.76$

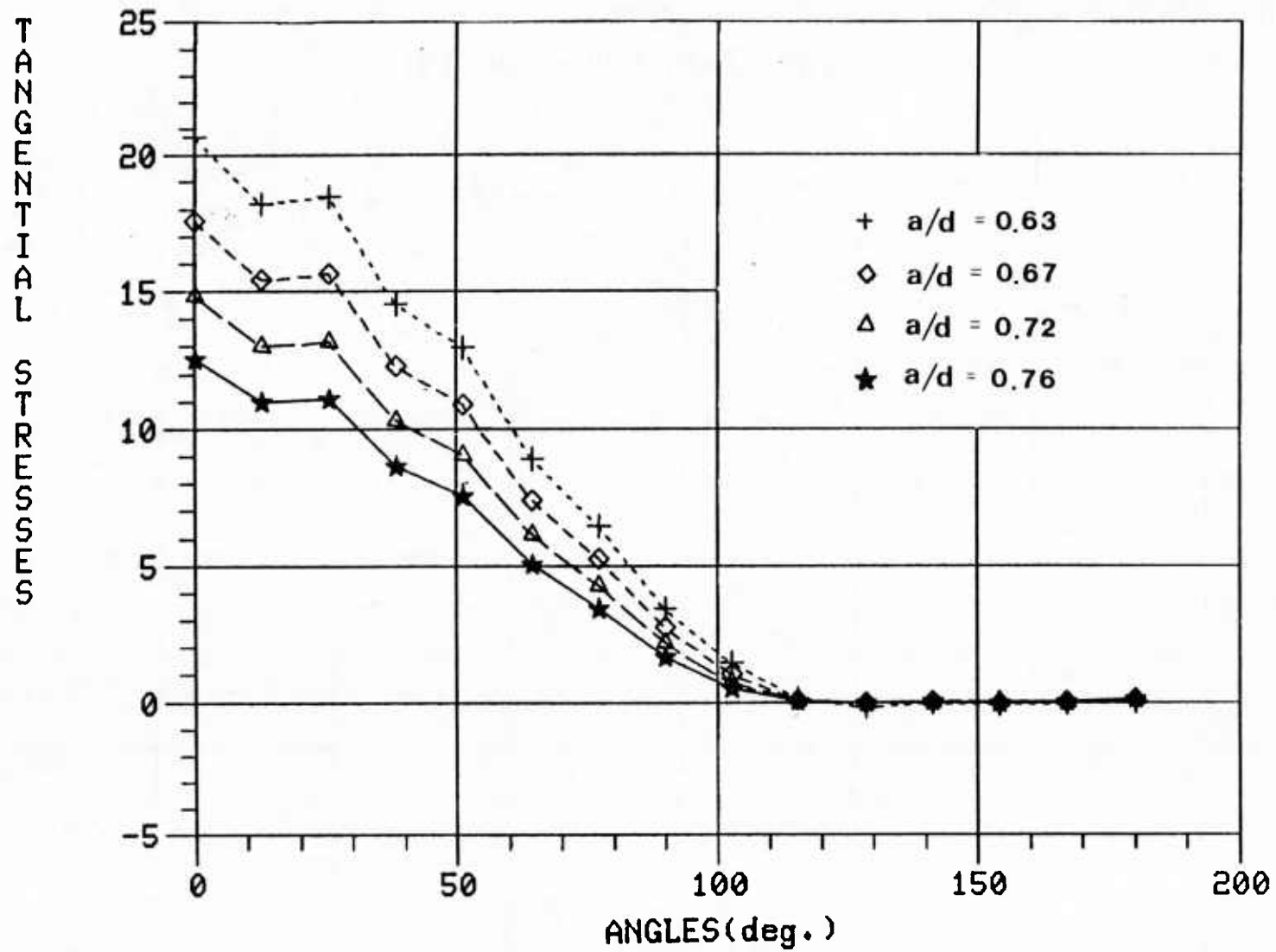


Figure 5.6 Variation of Tangential Stress Around Blunted Hole for $r/d = 0.009$

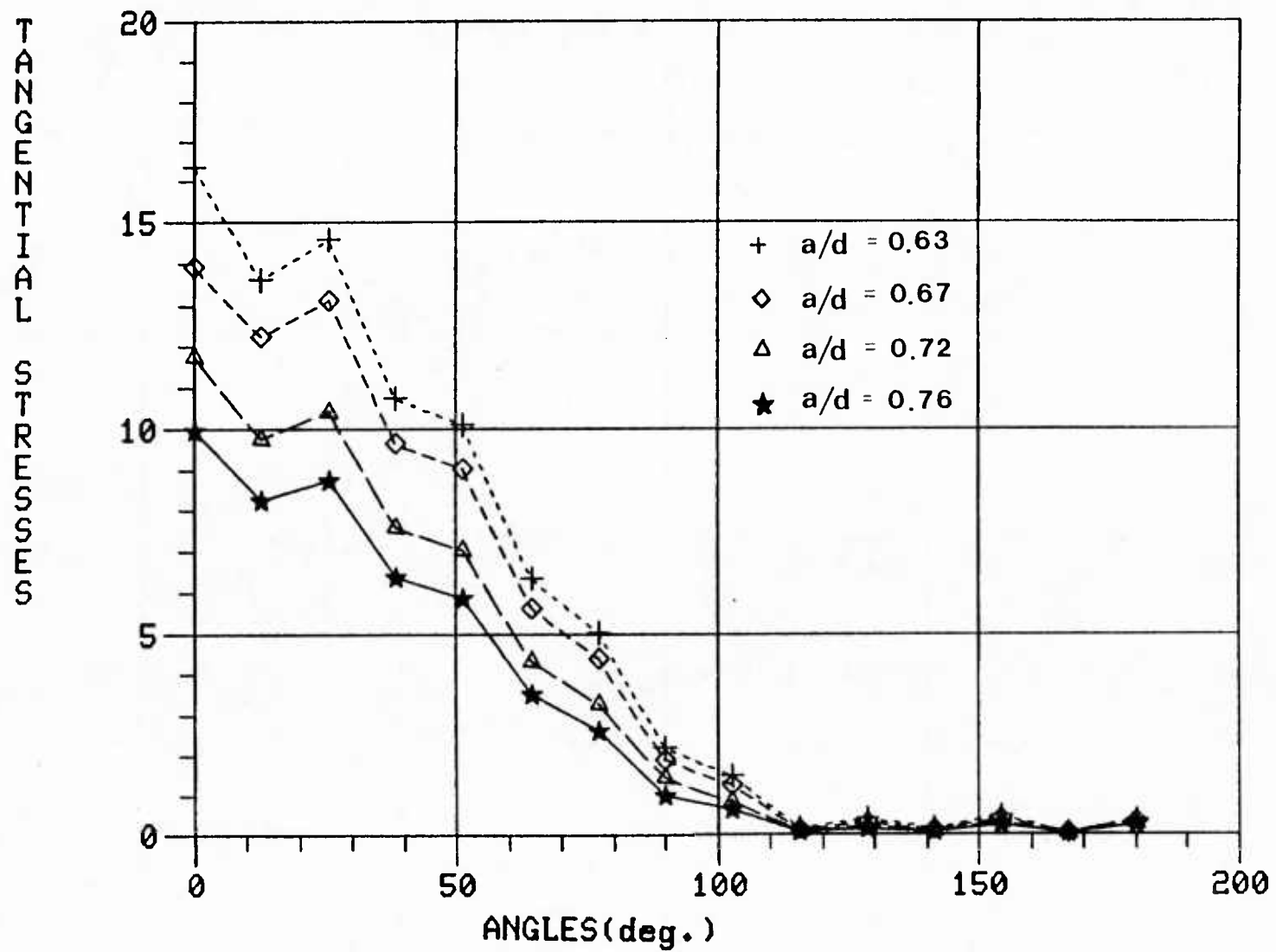


Figure 5.7 Variation of Tangential Stress Around Blunted Hole for $r/d = 0.016$

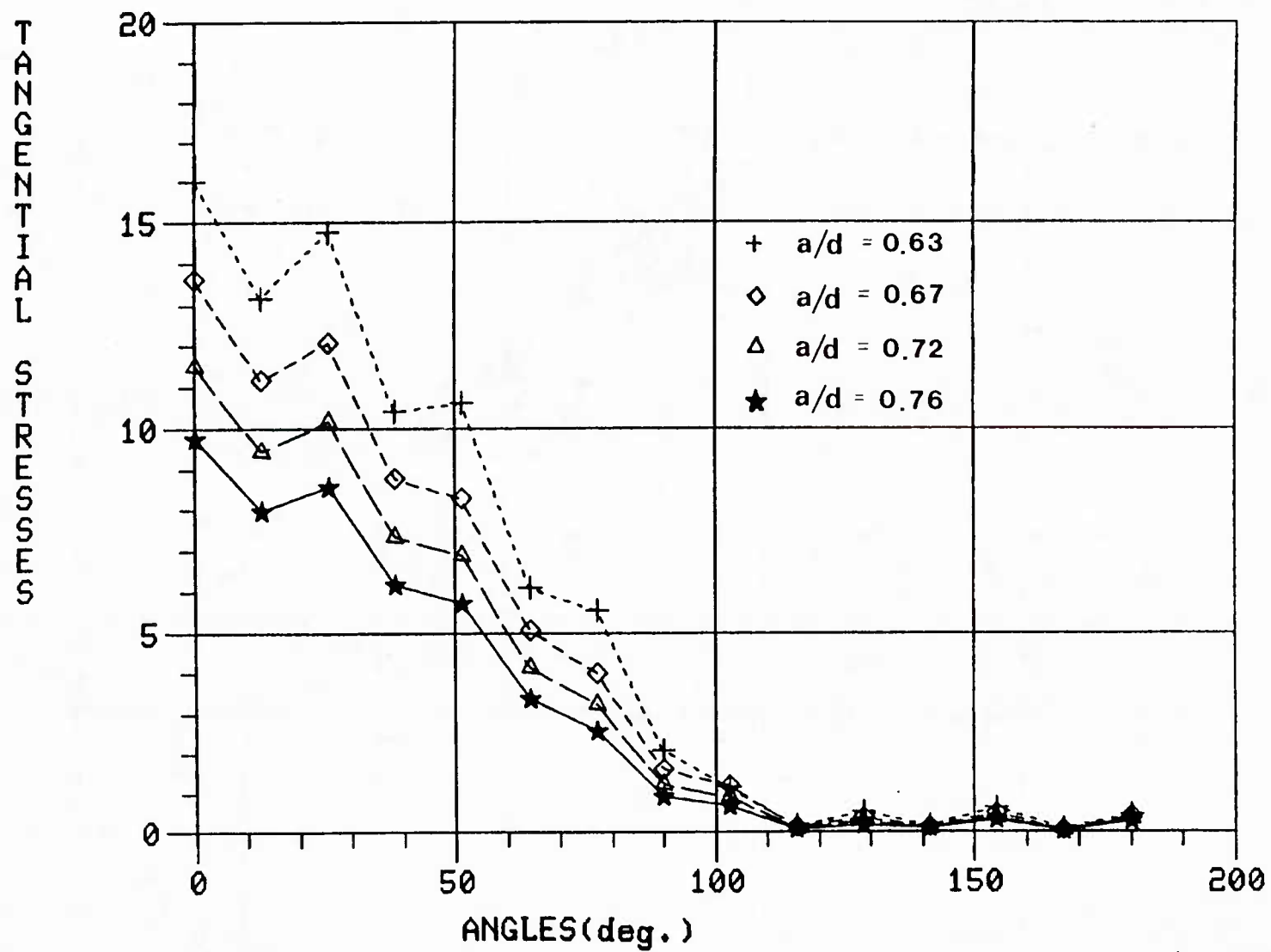


Figure 5.8 Variation of Tangential Stress Around Blunted Hole for $r/d = 0.017$

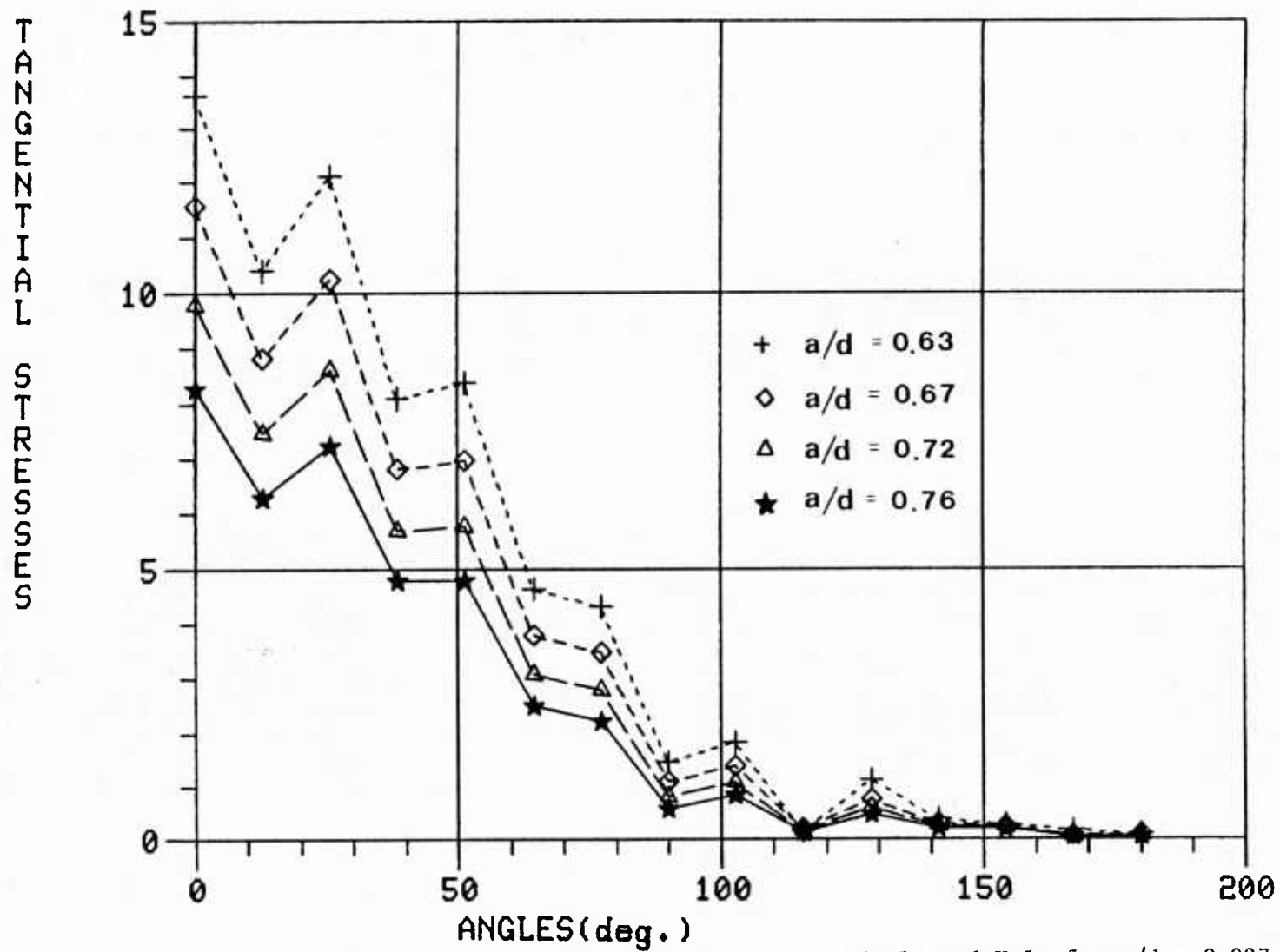


Figure 5.9 Variation of Tangential Stress Around Blunted Hole for $r/d = 0.027$

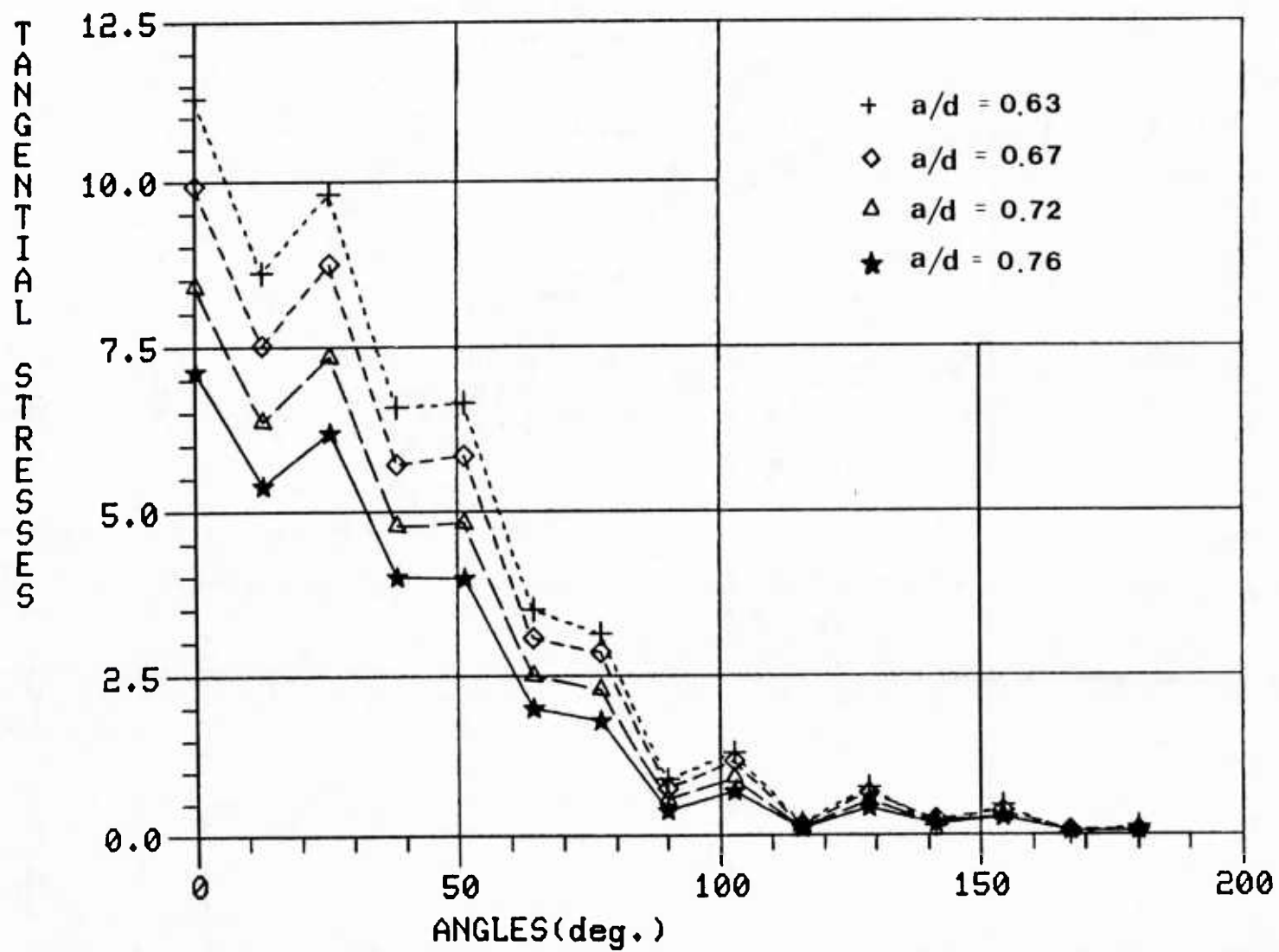


Figure 5.10 Variation of Tangential Stress Around Blunted Hole for $r/d = 0.038$

Third, the results are presented in terms of the stress concentration factor at the end of each notch. The stress concentration factors in Figure 5.11 are based on the full section while those in Figure 5.12 are computed for the net section. In these figures the stress concentration factor is plotted over the full range of r/d for each value of a/d .

For comparison with the results of the previous section, the stress concentration factors based on net section for $a/d=0.63$ are plotted in Figure 5.13 versus r/d . This graph shows values determined from both finite element analysis and equation (5-4). The factors from finite element analysis are 12 to 20 percent less than the corresponding value from section 5.1.

These results indicate the stress concentration increases as the notch becomes deeper and as the radius of curvature decreases. This supports the conclusion in Chapter 2 that as the radius goes to zero the notch becomes a crack and the stress concentration factor goes to infinity in the limit.

The stress concentration factor approach cannot fully describe the desired range of specimen geometries for the electromagnetic blunting problem because this approach is not applicable to the limiting case of the cracked specimen. Moreover, stress concentration factors cannot be used to explain the increase in load capacity in the blunted samples over the

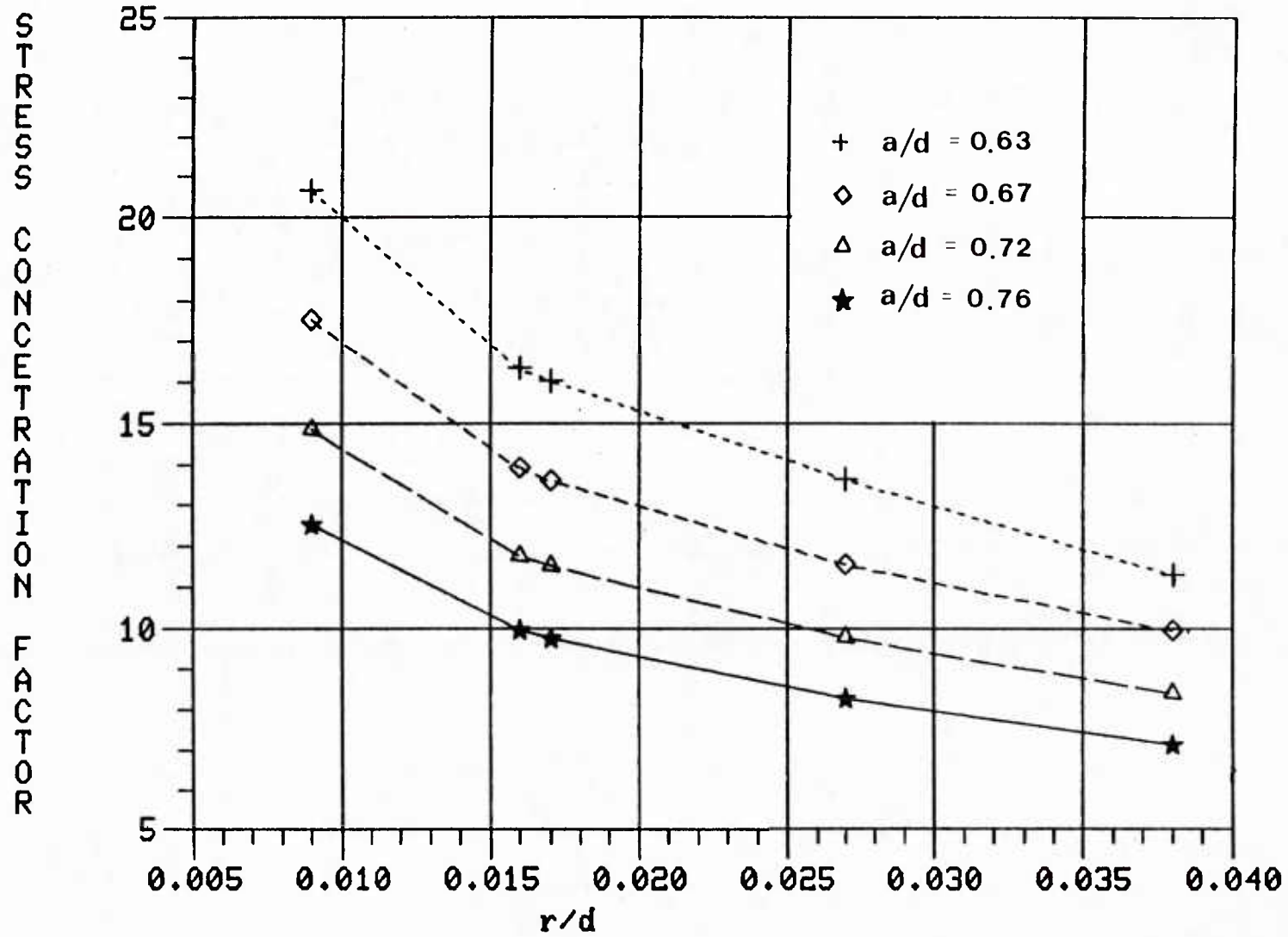


Figure 5.11 Stress Concentration Factors Based on Full Section

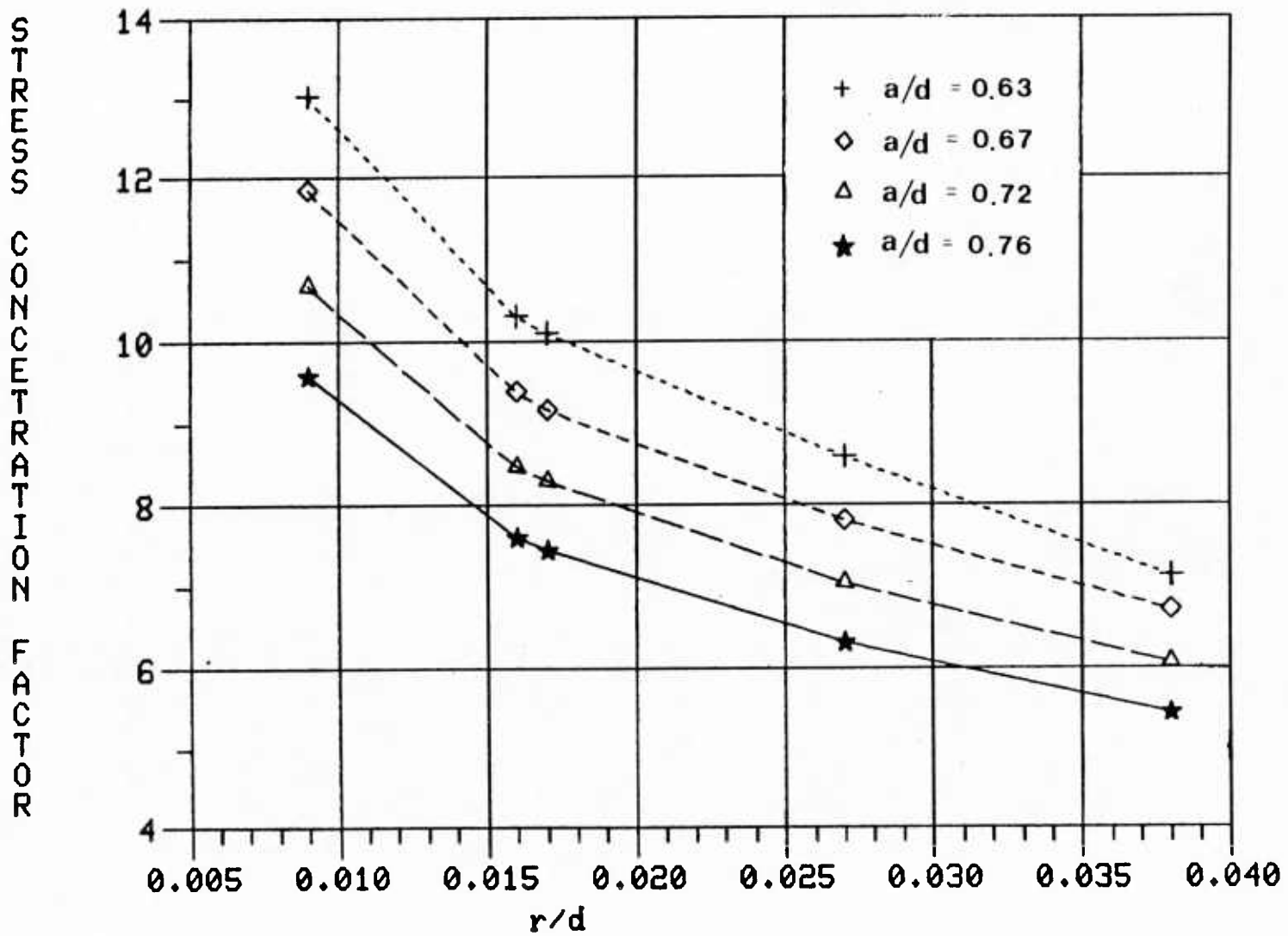


Figure 5.12 Stress Concentration Factors Based on Net Section

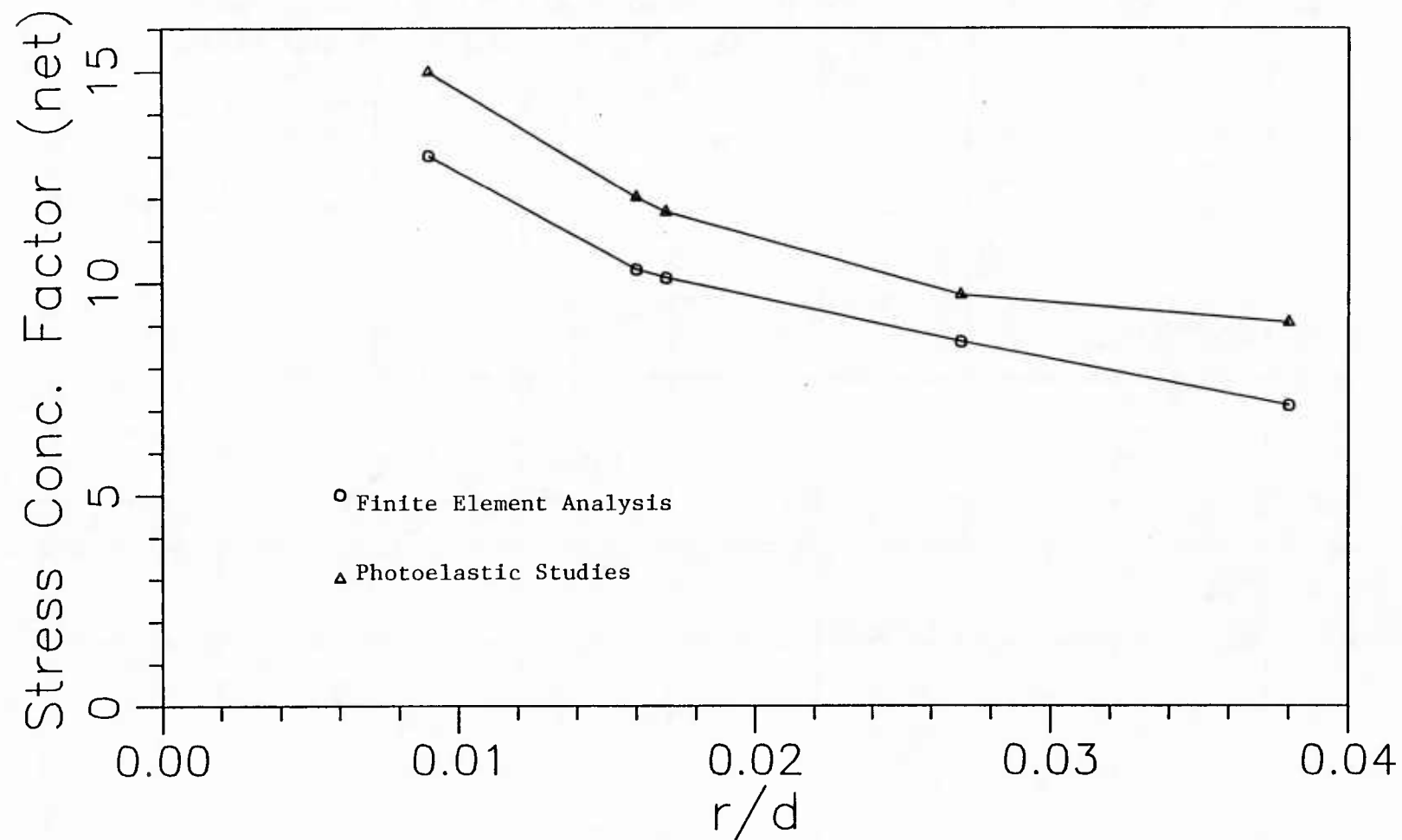


Figure 5.13 Comparison of Net Section Stress Concentration Factors from Finite Element Analysis and Photoelastic Studies (Eqn. 5-4) for $a/d = 0.63$

unblunted samples. Therefore, a more inclusive approach involving stress intensity factors is proposed in the next section.

5.3 STRESS INTENSITY FACTORS

Stress intensity factors are widely used in the analysis of cracks. Further, with certain assumptions these factors can be used to analyze the blunted test specimens from the experiments of Chapter 4. However, this study recognizes that stress intensity factors do not apply directly to the blunted case. Section 2.1.3 emphasizes this point. The reasons for this are discussed in more detail later in this section. First, however, the stress intensity factor approach is used for the cracked geometry where it is directly applicable.

5.3.1 STRESS INTENSITY FACTOR FOR THE UNBLUNTED CASE

Although the stress intensity approach is valid here in terms of the singular behavior in the cracked strip, one must also consider the restriction of small-scale yielding. Section 2.1.3 points out that most of linear elastic fracture mechanics is developed for plane strain situations. The important characteristic of plane strain here is that the plastic region at the crack-tip is generally small. For a plane stress situation such as the test strips, the plastic zone may not be small.

Section 2.1.3 also notes the inconsistent usage of the terms "plane stress" and "plane strain" in fracture mechanics literature. As an alternative to the generalizations offered by these terms, more specific methods have been developed to determine whether small-scale yielding exists. These techniques generally involve calculating the size of the plastic zone and comparing it to the "least dimension" of the structure. The least dimension refers to the distance extending from the crack-tip to the nearest boundary.

Calculation of the plastic zone size was discussed in Section 4.2.4 as a method of choosing a material in which the yielded region would be small. The latter section pointed out that calculating this quantity is uncertain because many factors which influence it are not included in a general model. The suggested method of computing plastic zone size is presented here as it was in Section 4.2.4.

Expressions used to estimate the plastic zone size, p , are of the form:

$$p = n(K/\sigma_y)^2 \quad (5-6)$$

in which K is the stress intensity factor and σ_y is the yield stress of the material. As before, n is taken to be $\pi/8$ for plane stress following the suggestion of Hahn and Rosenfield [30]. This

relationship is plotted for a wide range of values in Figure 4.11. For the specimen dimensions under consideration, the value of p was found to exceed the limit required for small-scale yielding as given in Reference 30.

Without the condition of small-scale yielding the accuracy of the stress intensity factor is sacrificed as indicated in Section 2.1.3. However, the latter section also points out that the stress intensity approach can be used successfully for comparison of various situations which is its main purpose in this study.

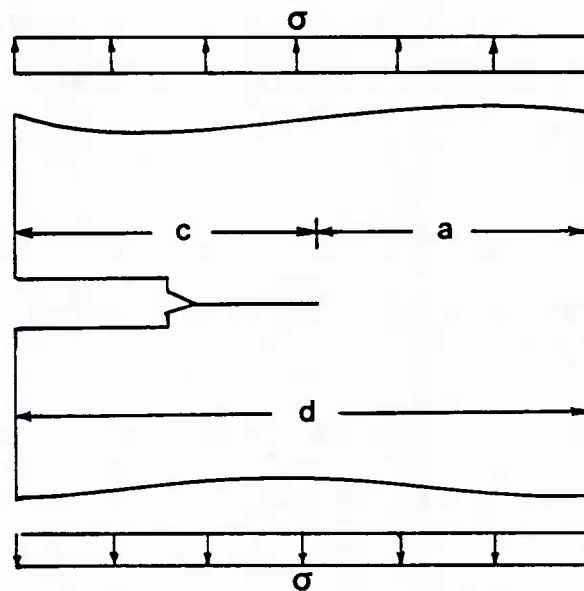
The value of K_I for the fractured strip can be computed in any one of the ways noted in Section 2.1.3.3. An analytical expression for K_I based on elasticity is given by Hellan [29] for this case. For the dimensions shown in Figure 5.14(a) this equation is:

$$K_I = \sigma \sqrt{\pi C} f(c/d) \quad (5-7)$$

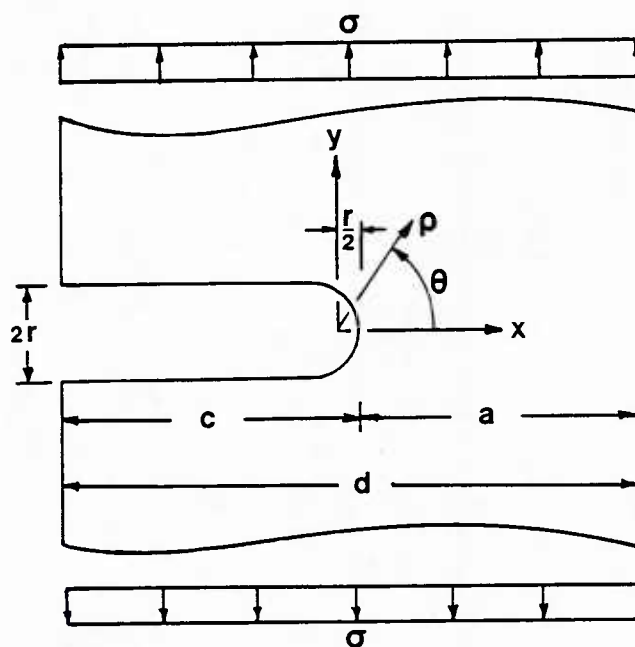
in which

$$f(c/d) = [1.12 - 0.23(c/d) + 10.6(c^2/d^2) - 2.17(c^3/d^3) + 30.4(c^4/d^4)] \quad (5-8)$$

In these formulas c is the crack length and σ is the stress applied at infinity.



(a) Fractured Test Strip Geometry



(b) Blunted Test Strip Geometry

Figure 5.14 Test Specimen Geometries for Computing K_I and K_Q

For the titanium specimen shown in Figure 4.1(b) the stress intensity factor at the moment of incipient crack propagation is computed to be $74.1 \text{ MPa}\sqrt{\text{m}}$. In equation (5-7) c is taken as 6mm and the applied stress is the failure load on the full section.

Since this value of K_I is computed using the ultimate stress, it is considered to be the critical stress intensity factor, K_{Ic} , for this situation. The discussion of critical stress intensity factors in Section 2.1.3.4 indicates that this plane stress value should be much higher than the plane strain value. The tabulated plane strain value, or fracture toughness, is $74.6 \text{ MPa}\sqrt{\text{m}}$ for Ti-6Al-4V [15]. The difference between the experimental value and the tabulated value is less than one percent.

Two explanations are offered here as to why the plane stress value was not observed to be greater than the fracture toughness. First, in reality, the situation may actually be one of small-scale yielding. The reason for this is the yield stress (825 MPa) and ultimate stress (895 MPa) in Ti-6Al-4V are relatively close in contrast to stainless steel with a yield point 310 MPa and an ultimate stress of 550 MPa. The yield and ultimate strength differ by 78 percent in stainless steel, while they are within 7 percent for the titanium alloy. This observation implies that the Ti-6Al-4V fractures soon after it reaches the yield point. This tends to produce a small plastic zone in any situation except one in which a shallow stress gradient exists. It is shown in Figure 5.5 that the elastic stress gradients are

very steep around the blunted crack-tip. Hence, one can infer that the plastic zone in Ti-6Al-4V is small.

The second explanation, on the other hand, asserts the opposite. The plastic zone size is considered to be large which causes significant redistribution of stress. This results in lower stress gradients. Based on these ideas the critical stress intensity factor for the test strip should actually be higher than the value computed by Equation (5-7). This explanation receives credibility when one considers the "effective crack size" correction proposed by Tada [13]. To provide for large-scale yielding, this method suggests that an effective crack size be used in calculating stresses and stress intensity factors instead of the actual crack length. The effective crack length is taken as the real crack length plus the size of the plastic zone, which is computed from Equation (5-6). In this manner K_{Ic} is recomputed to be $95.7 \text{ MPa}\sqrt{\text{m}}$.

Either of these explanations appear plausible. In the actual specimens, the situation is probably a combination of the two conditions described here.

5.3.2 STRESS INTENSITY FACTORS FOR THE BLUNTED GEOMETRY

This section explains why the stress intensity factors cannot be applied to the blunted geometry and then describes a similar method which can be used for such cases.

Failure can be predicted in a given fracture situation based on a comparison with a known critical crack condition. Therefore, in fracture studies it is necessary to compare the severity of a crack in a structure to other cracks. On a macroscopic level, cracks exhibit a stress singularity at their tip. Hence, a parameter is needed to compare the intensity of stress singularity in different cracks. This parameter is the stress intensity factor.

One can see that the stress intensity factor is valuable for studying cracks. However, difficulties arise when this approach is applied to the blunted situation because there is no longer a singularity at the tip. Thus, in a strict sense, the stress intensity factor cannot be used for nonsingular geometries.

The stress intensity factor approach can be applied to the case of deep slender notches, however, by selecting the origin of the coordinate system to be at a distance $r/2$ away from the notch tip [13]. A slender notch with this coordinate system is shown in Figure 5-14(b). The normal stress in the y-direction, σ_y , is now given by:

$$\sigma_y = \frac{K_I}{\sqrt{2\pi\rho}} \frac{r}{2\rho} \cos \frac{3\theta}{2} + \frac{K_I}{\sqrt{2\pi\rho}} \cos \frac{\theta}{2} \left[1 + \sin \frac{\theta}{2} \sin \frac{3\theta}{2} \right] \quad (5-9)$$

in which K_I is the same K_I as in equation (2-3b) and is computed in the same way. The above equation contains no singularity at

the notch tip as would occur at the tip of a crack in equation (2-3b).

Equation (5-9) and equation (2-3b) differ only by the additional term at the beginning of equation (5-9). This added term is significant only in the region immediately surrounding the notch tip. Blunting of a crack, therefore, is observed to reduce the stresses only in the immediate vicinity of the crack tip. At points away from the crack tip the distribution is the same in both cases.

For equation (5-9) to be valid the notch must be sufficiently deep and slender such that the stress field is very near to that of the singular distribution in the crack. The notch geometry under consideration for the test strips is not slender and deep enough for this method to apply directly. However, a quantity based on stress intensity concepts can be defined for use in comparing the blunted and unblunted geometries. The value to be used for this study is known as the apparent stress intensity factor and is denoted by K_q . Likewise, the terms "effective stress intensity factor" and "conditional stress intensity factor" are used to refer to this quantity.

For the test strip configuration, K_q is defined by equation (5-7) which is the corresponding stress intensity factor expression for the geometry containing a singularity. Hence, in the case of the unblunted specimen (e.g., zero effective crack-tip radius) the value of K_q is equal to K_I . With $f(c/d)$ given by

Equation (5-8) and the dimensions shown in Figure 5.14(b), one can write:

$$K_q = \sigma \sqrt{\pi c} f(c/d) \quad (5-10)$$

in which K_q is the "apparent stress intensity factor." It should be noted that equation (5-7), and hence equation (5-10) as well, is based on an elasticity solution using the boundary collocation method [31].

Equation (5-10) is used to compute the apparent stress intensity factor for each of the titanium samples tested in Section 4.3. In each case the applied stress, σ , is taken as the stress on the full section at failure. Therefore, the value determined for each test specimen is referred to as the critical apparent stress intensity factor or critical K_q .

Figure 5.15 shows the results of these calculations plotted versus crack radius. The solid line in this figure is obtained from a linear regression analysis. A reasonably close fit is indicated by the correlation coefficient of 0.84. One can see from this graph that blunting produces a maximum increase of close to 100 percent in critical K_q over the unblunted case. Furthermore, a 156 percent increase in critical K_q is observed over the whole range of values.

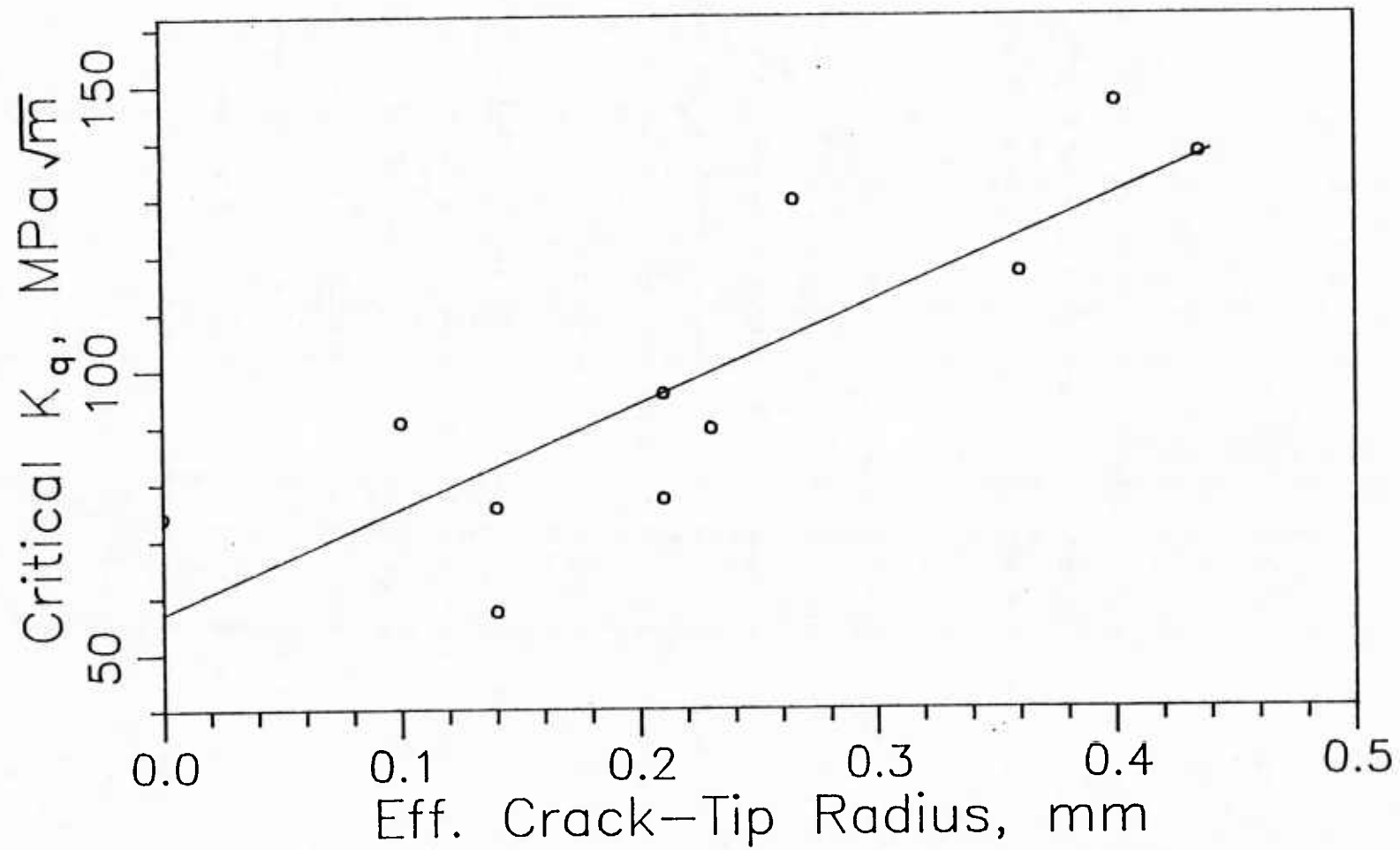


Figure 5.15 Critical Apparent Stress Intensity Factor Computed from Equation (5-10) vs. Effective Crack-Tip Radius in Ti-6Al-4V

Up to this point only analytical expressions have been used to compute stress intensity factors and K_q values. Section 2.1.3.3 indicates several other methods available for computing stress intensity factors. Likewise, these techniques can be extended to the calculation of apparent stress intensity factors as well. The stress concentration factor approach and finite element method mentioned in Chapter 2 are applied here to the blunted specimens. Computationally, the two approaches are the same since K_q is determined from a stress concentration factor in both cases. The difference, however, is that the stress concentration factor is determined by photoelasticity in one case and by finite element analysis in the other.

To develop a relationship between stress concentration factor and apparent stress intensity factor, consider the notch configuration in Figure 5.14(b). For this geometry the normal y-direction stress distribution, σ_y is given by equation (5-10). The maximum stress as given by this expression occurs at $\rho = r/2$ and $\theta = 0$. With these coordinates, equation (5-10) is set equal to the maximum stress in terms of the appropriate stress concentration factor. The resulting relationship can be solved for the stress intensity factor, K_I . This expression can then be used to calculate stress intensity factors, K_I , which for the blunted test strips correspond to the apparent stress intensity factors, K_q . The expression in this case is:

$$K_q = \frac{\sqrt{\pi r}}{2} K_c \sigma_{nom} \quad (5-11)$$

in which K_c is the relevant stress concentration factor, σ_{nom} is the average stress on the net section, and r is the crack radius. The critical apparent stress intensity factor based on the photoelastically determined stress concentration factor is plotted versus crack radius in Figure 5.16. The corresponding curve based on the stress concentration factor from finite element analysis is given in Figure 5.17. A linear regression analysis in each case resulted in the solid line shown in each figure. The correlation coefficients were 0.92 and 0.93, respectively, which indicate that fairly consistent values of K_q are obtained from these methods. In the case of the photoelastic stress concentration factors, the maximum increase in K_q is 132 percent while an increase of 150 percent is observed in the finite element related values of the critical apparent stress intensity factor.

To compare the three methods of calculating apparent stress intensity factors, the graph of critical K_q versus crack radius for each case are combined in Figure 5.18.

In summary, stress intensity factors are developed specifically to compare the severity of different stress singularities and, therefore, cannot be applied directly to the blunted geometries. This section, however, describes an equivalent approach for nonsingular geometries which uses apparent stress intensity factors. The latter method is then used to express the results of the electromagnetic blunting tests of Chapter 4.

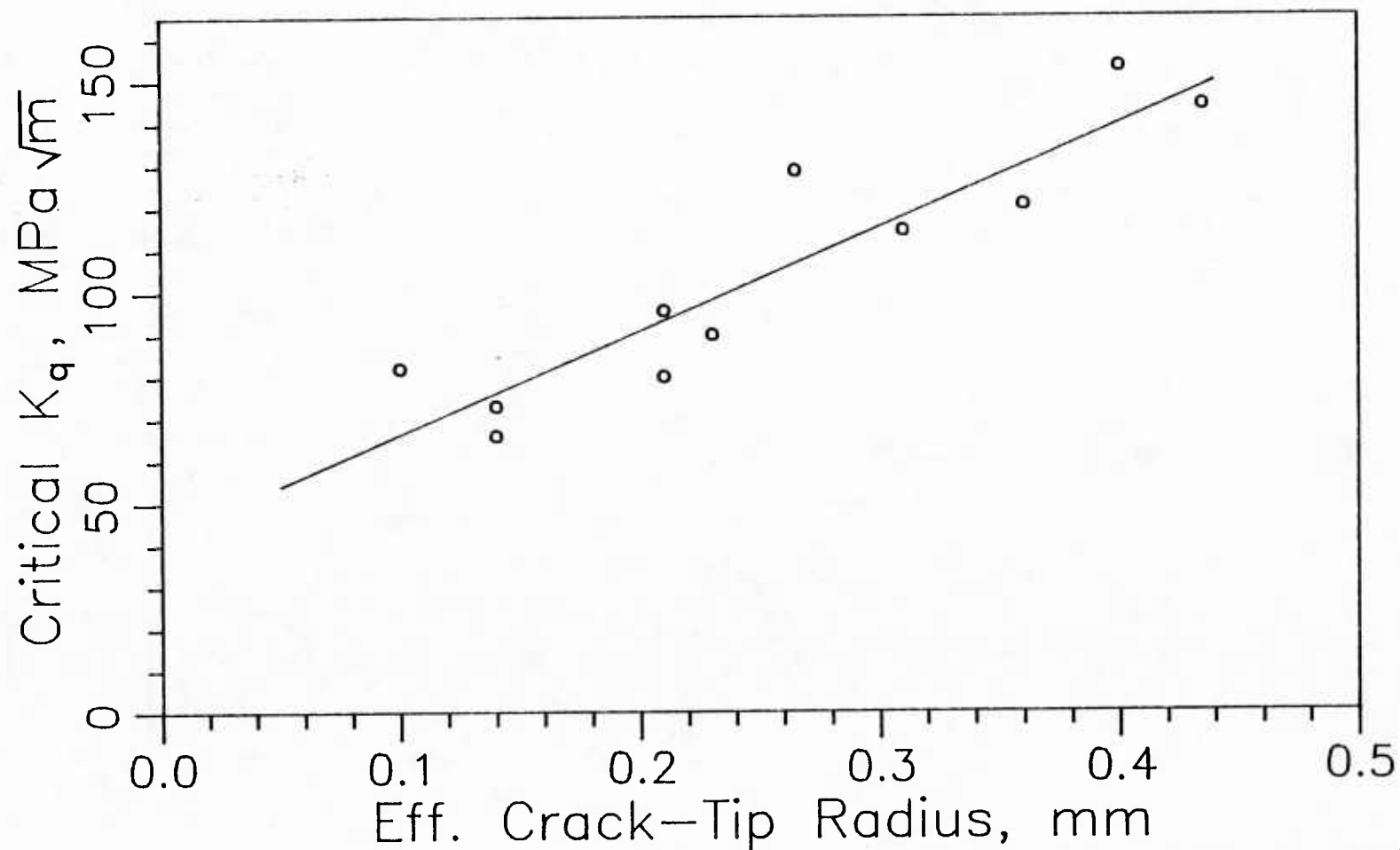


Figure 5.16 Critical Apparent Stress Intensity Factors based on Stress Concentration Factors from Photoelastic Studies vs. Eff. Crack-Tip Radius in Ti-6Al-4V

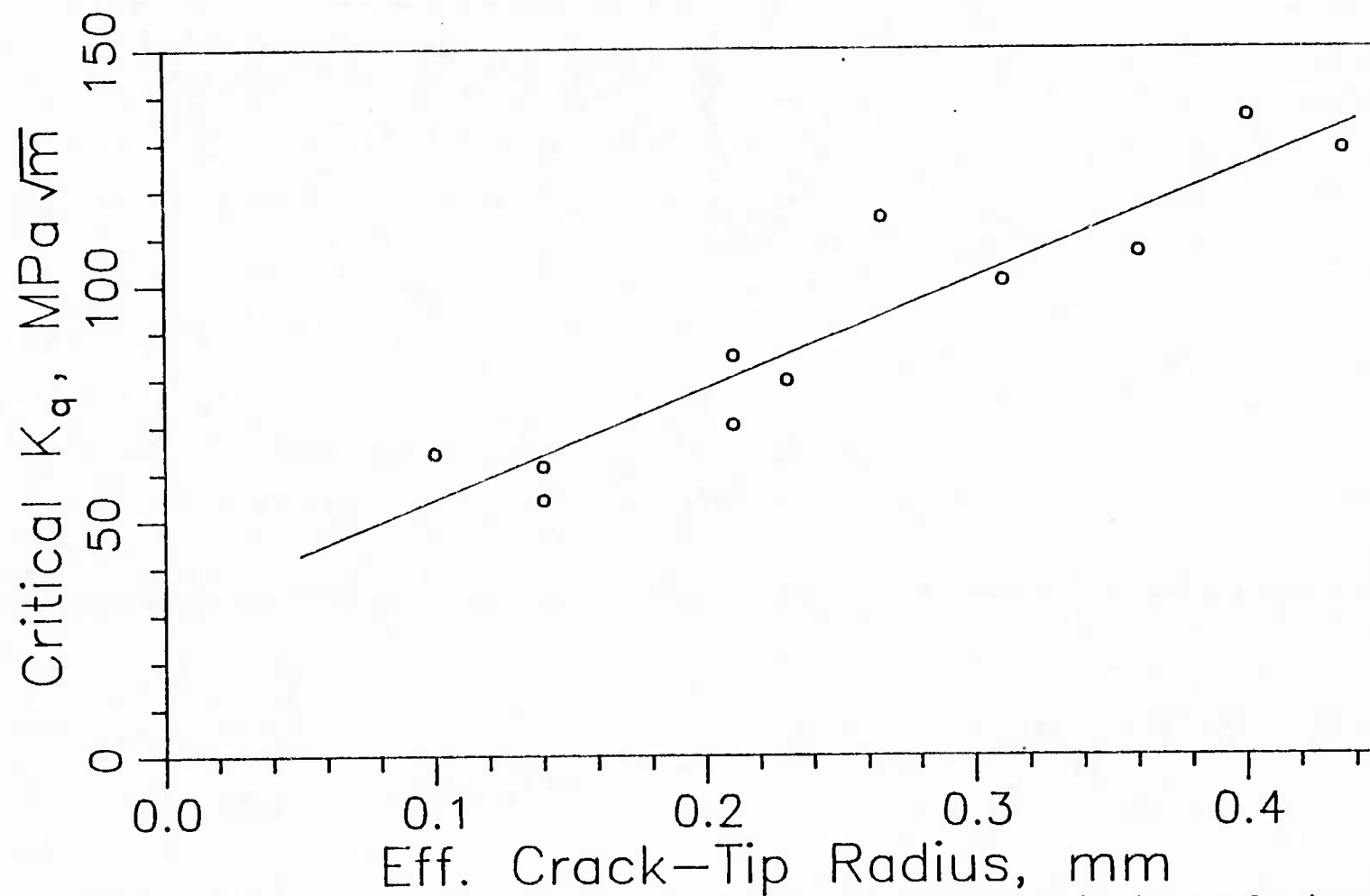


Figure 5.17 Critical Apparent Stress Intensity Factors for Ti-6Al-4V Test Specimens based on Stress Concentration Factors from Finite Element Analysis

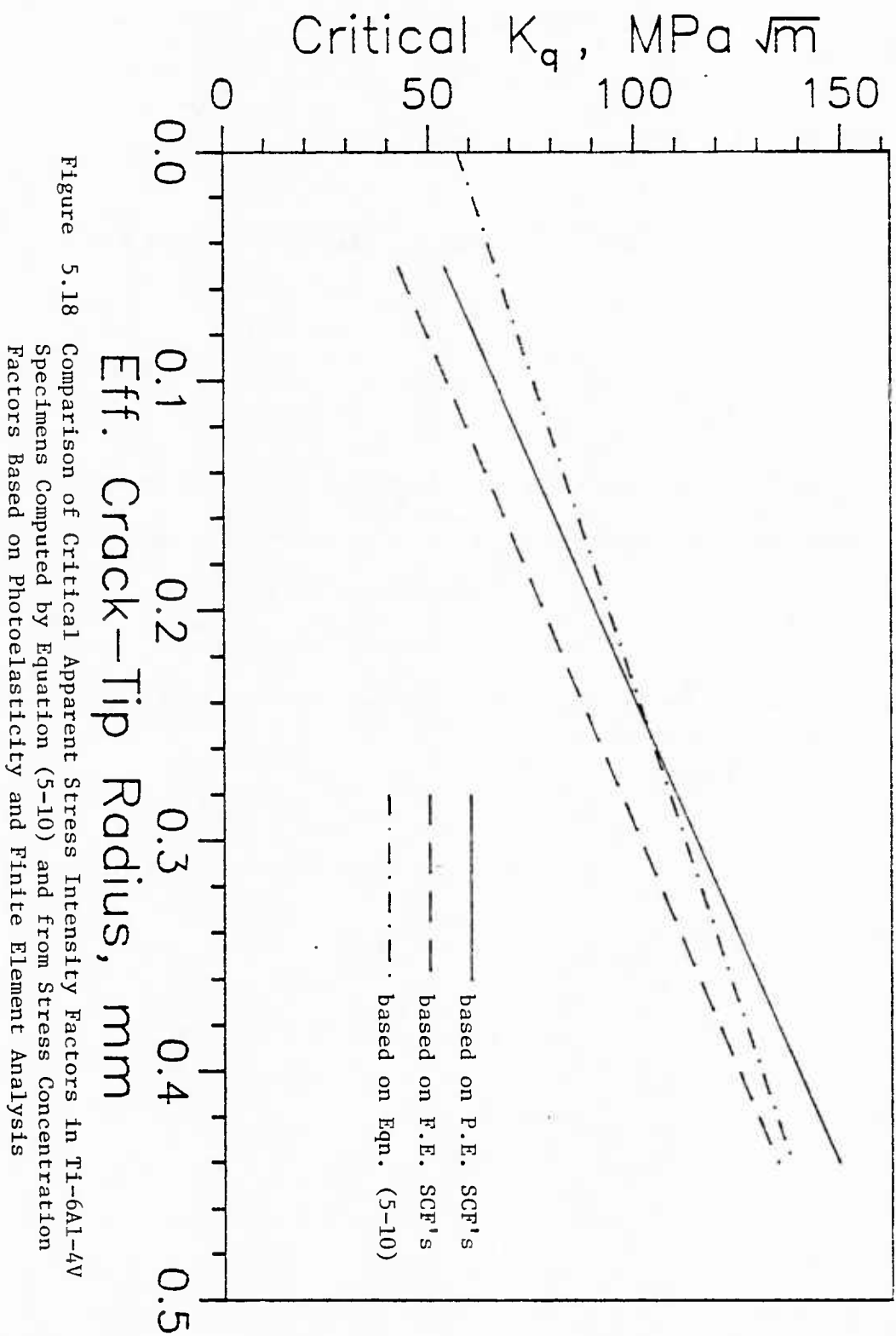


Figure 5.18 Comparison of Critical Apparent Stress Intensity Factors in Ti-6Al-4V
Specimens Computed by Equation (5-10) and from Stress Concentration
Factors Based on Photoelasticity and Finite Element Analysis

CHAPTER 6

CONCLUSION

In this study two problems in electromagnetics are addressed. First, existing programs for the analysis of eddy currents in thin plates are extended to include transport currents. Second, the electromagnetic blunting of fatigue cracks is investigated experimentally. A separate section containing a summary, conclusions, and further research is devoted to each of these topics.

6.1 NUMERICAL ANALYSIS OF ELECTRIC CURRENTS

Numerical analysis of electric currents, as it is considered in this study, is summarized in the first section below. This is followed by a description of the conclusions which can be drawn

from the work to date and a list of suggestions for further research.

6.1.1 SUMMARY

A procedure for including transport currents in the numerical analysis of electric currents in thin plates is developed and implemented. The method for analyzing transport currents is based on an extension of an original stream function solution for induced currents in thin plates. Finite element analysis is used to determine the value of the stream function over the plate. The expanded version of the program is capable of solving problems in which an external time-dependent magnetic field is or is not present. The proposed technique for admitting transport currents is presented in terms of necessary changes to the original formulation and changes to the finite element system of equations at the program level.

On the theoretical level, inclusion of transport currents involves changes to the governing integro-differential equation and changes to the boundary conditions. In the finite element solution of the problem, these modifications correspond to changes in the formulation and changes to allow nonzero boundary conditions.

By approaching the problem from a theoretical standpoint, one finds that the revised form of the governing relationship includes additional edge terms which are related to the nonzero value of the stream function on the edges. For simple configurations, an equivalent method for implementing the edge terms is proposed and shown to be acceptable for including their effect.

For the changes in boundary conditions, the finite element equations are rearranged to admit nonzero values at the edges. The revised system of equations requires the evaluation of a previously undetermined portion of the overall stiffness matrix, $[K_{12}]$.

The above changes are implemented in EDDY1 which is subsequently verified both experimentally and analytically. For the two-dimensional program, EDDY2, the necessary changes in the formulation are outlined and preliminary steps are taken in the program.

6.1.2 CONCLUSIONS

Transport currents are added to the numerical analysis of induced currents in thin plates by making the necessary changes in the formulation and in the boundary conditions. Two alternatives are available for implementing the correct formulation in the one-dimensional program. Either the additional terms can be included directly in the solution procedure, or an equivalent

magnetic field can be applied to the plate which represents the effect of these terms. Nonzero boundary conditions must be included by appropriately rearranging stiffness terms.

In the case of a one-dimensional plate, the edge terms represent an induced field generated by currents along the edges of the plate due to nonzero values of the stream function there. The effect of this induced field is felt only for high frequencies and influences the solution by only about five percent in these cases.

6.1.3 SUGGESTIONS FOR FURTHER RESEARCH

While the influence of the edge terms in the one-dimensional case is accounted for, the corresponding effect in two-dimensions remains to be studied. Based on an investigation of this case, a satisfactory method for including the edge effects should be developed. This case may require full implementation of the edge terms in the formulation. However, the possibility of developing an equivalent technique which is easier to implement, such as in the one-dimensional case, should be pursued. An open question is the posing of proper boundary conditions and edge terms along a portion of the edge across which current is flowing. For the local case, this question is trivial, but significant nonlocal effects make the variation of the stream function along such segments unknown.

In relation to the changes already made, a parallel development in graphics capabilities of these programs is advisable. The general features which would be useful include:

1. The ability to specify graphically the applied transport current (via nonzero boundary conditions) using the preprocessor.
2. A graphical display of the input transport current.
3. A graphical display of the current distribution in a plate resulting from an applied transport current as well as an applied magnetic field.
4. The new version of the program is currently limited to a maximum of 52 nodes by the size of $[K_{12}]$ and related matrices. This limitation would best be alleviated by using dynamic allocation for these arrays. However, the disadvantage is that the overall modifications would be less separate from the original program as a result.

In the two-dimensional case the transport current capability would be useful in analyzing the electromagnetic blunting problem described in the second part of this study. By modifying the programs in this way, one could then investigate the experiments analytically as well. The temperature distribution determined from the current solution would be especially useful for predicting the amount of current needed for melting holes at crack-tips in a material of a given type.

A synopsis of the experimental work done in this area is presented in the next section.

6.2 ELECTROMAGNETIC CRACK-TIP BLUNTING

This section first summarizes the experiments conducted on the electromagnetic blunting of fatigue cracks. Conclusions based on these results are drawn in the second section. In the last section, recommendations for additional study in this area are presented.

6.2.1 SUMMARY

To investigate the proposed method of crack-tip blunting, thin strips of stainless steel 304 and titanium alloy Ti-6Al-4V are used. These samples contain either a razor notch or a fatigue crack in one side. To blunt these stress risers, a current pulse is applied to each specimen which causes a sufficient current concentration at each crack tip to melt a hole. In some cases the Ti-6Al-4V strips are blunted while loaded in tension to prevent current from jumping across the crack. A series of the stainless steel samples is also blunted by drilling rather than melting a hole to study the effects of electromagnetic heating on the surrounding metal.

The hole dimensions in all of these specimens are measured. Each strip is then loaded to failure under static, direct tension and the ultimate stress on the remaining section is computed.

6.2.2 CONCLUSIONS

Based on the experimental results, there are two general observations which can be made that are of primary interest. The first is that blunting of a crack produces an increase in the static ultimate strength of the plate member containing the crack. In stainless steel the maximum increase is 19 percent while the corresponding increase in titanium is 78 percent. Second, in the context of the critical apparent stress intensity factors computed in Chapter 5, blunting produces an increase in fracture toughness.

More specific conclusions which can be drawn are:

1. For stainless steel, comparison of the electromagnetic and drilled hole results indicates that heating during the electromagnetic blunting procedure has no significant effect on the strength of the material.
2. An external magnetic field applied transversely to a strip during the blunting procedure influences the size of the hole which is created. The hole size increases when the external magnetic field amplifies the induced transverse magnetic field. Conversely, when the external magnetic field opposes the induced transverse field the resulting hole is smaller.

The external magnetic field is found to have no significant effect on strength characteristics other than the hole size. Based on these observations, an external field may be of use in creating larger holes for a fixed amount of current.

3. The nitrogen cooling jet is found to have an effect similar to that of the external magnetic field. Again, the ultimate strength is influenced only through the effect on the size of the hole produced. However, the degree of influence on hole size in the case of the nitrogen jet is much less than in the case of the external magnetic field. The cooling jet is observed to have a much greater effect on the shape of the hole rather than its size. By forcing the nitrogen into the crack, the hole is pushed farther into the specimen and the resulting shape is rounded and squat. Application of the jet in the opposite direction creates a narrower hole located nearer to the cracked edge.
4. During the initial testing of titanium the applied current is observed to jump across the crack, and this arcing results in incomplete hole formation. Subsequent tests show that a tensile load on the strips can open the crack enough to prevent this problem. In stainless steel this effect is not evident. This observation indicates the brittle nature of titanium and the smaller amount of plastification it exhibits in the vicinity of a crack.

5. For fatigue cracked specimens, many of the same conclusions are drawn from both the titanium and stainless steel results. Both metals show that larger holes are created by applying larger current pulses. Considerable scatter exists in the relationship between hole size and applied current. From the static ultimate strength tests in both metals one can see that ultimate stress increases as with increasing hole size and applied current. Specifically, a maximum increase in ultimate stress of 78 percent is possible in titanium strips under load. Even greater gains in strength may be possible by creating even larger holes. The slope decreases in Figure 4.17, however, which indicates a limit may be reached in the ultimate stress. Comparison of these relationships for both metals indicates that a greater increase in ultimate stress is possible with titanium. Since the size of the plastic zone in Ti-6Al-4V is small, the percentage of this yield region which is removed in the blunting procedure is greater. Hence, the relative proportion of yielded to unyielded material in the remaining cross section is less.
6. In titanium, other trends are evident in the data involving the load applied during the blunting process. An increase in applied load produces a larger hole size and, hence, a related increase in ultimate stress as well.

7. Conclusions regarding the changes in fracture properties as a result of the blunting process can be made from the data presented in Chapter 5. The interpretations of these results, however, must be drawn in the context in which they are developed. That is to say, the results can be used to predict the initiation of fracture in similar circumstances but their application to other situations is not valid because the critical value of K is highly situation-dependent. Hence, the critical value is affected by a number of factors which cannot be accounted for in a simple theory. With this in mind, the trends are expressed in terms of a value called "K conditional" or apparent stress intensity factor. Three methods are used to calculate this parameter which is denoted by K_q . Based on the analytical method, the blunting procedure is shown to increase the critical value of K_q nearly 100 percent over the value for the crack alone. The second and third procedures were based on stress concentration factors and, therefore, a K_q value for the unblunted case could not be computed. However, the average maximum increase in critical K_q for these two methods is found to be over 140 percent. Even greater gains in critical K_q may be possible by producing larger values of effective crack-tip radius.

6.2.3 SUGGESTIONS FOR FURTHER RESEARCH

The blunting of cracks explored in this study is only one of the many potential applications of electromagnetic phenomena to cracks. Several interesting possibilities for applying electromagnetic effects to damaged structures, other than blunting, are described later in this section. First, other facets of electromagnetic blunting which deserve further investigation are discussed.

1. Subsequent work should consider aspects of fracture behavior other than the ultimate stress and apparent stress intensity factor. For example, a study of the effect of blunting on the fatigue crack growth rate would be valuable.
2. Some of the recently proposed methods for fracture analysis of elastic-plastic situations may be useful in describing the results of these experiments. For the plane stress test strips these techniques may be especially valuable in light of the discussion of small-scale yielding in Section 5.3.1. Methods of analysis in elastic-plastic fracture mechanics have not been uniformly accepted, but Rolfe and Barsom [12] point out three which appear to hold promise: R-curve analysis, Crack-Opening Displacement (COD), and J-Integrals. The advantages and disadvantages of each of these approaches should be weighed in choosing the best methods for describing the experimental results.

3. Additional study should be devoted to the effects of external magnetic fields and cooling during the blunting process.
Other methods of cooling should be investigated. For example, immersing the specimens in a cooling medium during the blunting process may prove to have significant results.
4. By using the drilled hole procedure as in the case of stainless steel, the effect of heating during the blunting procedure should also be investigated in titanium.
5. Experiments should be conducted in other materials.
Particular consideration should be given to brittle materials since they appear to show the most promise based on the comparison of titanium and stainless steel in this study.
6. Brittle fracture and fatigue problems occur in structures under a wide variety of conditions. In many cases, the resistance of structural materials to fracture and fatigue is reduced by exposure to corrosive environments such as water, salt water, oil, temperature extremes, etc. Blunting cracks under these conditions may result in even greater gains in ultimate strength and fracture resistance than are shown in this study for controlled environments. Subsequent work, therefore, should include tests under different conditions which simulate a variety of corrosive environments.

Possibilities exist for applying electromagnetic effects to damaged structures other than the blunting considered in this study. Some of the areas which should be investigated are listed below.

1. By enclosing the crack with material on both sides, or in the case of an embedded three-dimensional crack, the molten metal may be forced into the crack rather than out of the body, resulting in a rewelded crack.
2. By closing the crack under load and using controlled melting, it may be possible to remelt the metal locally such that the two surfaces are fused together.
3. Although this study used transport currents to melt the material, induced currents may be used to achieve the same effect. In many cases, the induced current method may be more convenient because it does not require extensive attachments to the structure to apply the current. Moreover, it may be the only way to blunt or reweld in cases where the crack is inaccessible by other means.
4. Electromagnetic effects may be especially valuable in welded structures. Considerable possibilities exist for the use of such methods in repairing faulty welds.

REFERENCES

1. Cox, H.L., "Four Studies in the Theory of Stress Concentration," Aeronautical Research Council (London), Report 2704, 1953.
2. Inglis, C.E., Trans. Inst. Nav. Archit., Vol. 1, p. 219, 1913.
3. Neuber, H., Theory of Notch Stress, Edwards Brothers, Inc., Ann Arbor, Michigan, 1946, pp. 48, 49.
4. Timoshenko, S.P., and Goodier, J.N., Theory of Elasticity, McGraw-Hill, N.Y., 1970.
5. Savin, G., Stress Concentration Near Holes, Pergamon Press, N.Y., 1961.
6. Boresi, A.P., et al., Advanced Mechanics of Materials, third ed., John Wiley and Sons, N.Y., 1978.
7. Sih, G.C., (ed.), Mechanics of Fracture 5: Stress Analysis of Notch Problems, Noordhoff International Publishing, Alphen Aan Den Rijn, 1978, p. XIII.
8. Irwin, G.R., "Analysis of Stresses and Strains near the end of a Crack Traversing a Plate," J. of Appl. Mech., 1957, Vol. 24, p. 361.
9. Sih, G.C., et al., Prospects of Fracture Mechanics, Noordhoff International Publishing, Leyden, 1974, pp. 85-102.
10. Hayes, D.J., "Origins of the Energy Balance Approach to Fracture," A General Introduction to Fracture Mechanics, Mechanical Engineering Publications Limited, London, 1978.

11. Westergaard, H.M., "Bearing Pressures and Cracks," J. of Appl. Mech., Vol. 61, 1939, p. A49.
12. Rolfe, S.T., and Barsom, J.M., Fracture and Fatigue Control in Structures, Prentice Hall Inc., Englewood Cliffs, N.J., 1977, p. 31.
13. Tada, H., et al., The Stress Analysis of Cracks Handbook, Del Research Corp., Hellertown, P.A., 1973.
14. Cartwright, D.J. and Rooke, D.P., "Evaluation of Stress Intensity Factors," A General Introduction to Fracture Mechanics, Mechanical Engineering Publications Limited, London, 1978.
15. Properties and Selection: Stainless Steel, Tool Materials, and Special Property Metals, Metals Handbook, 9th ed., Vol. 3, American Society for Metals.
16. Yuan, K.Y., "Finite Element Analysis of Magnetoelastic Plate Problems," PhD Thesis, Cornell University, Department of Structural Engineering, 1981.
17. Yuan, K.Y., Moon, F.C., and Abel, J.F., "Numerical Solutions for Coupled Magnetomechanics," Cornell University, Department of Structural Engineering Report Number 80-5, February, 1980.
18. Moon, Francis, C., Magneto-Solid Mechanics, John-Wiley and Sons, Inc., New York, 1984.
19. Moon, F.C., "Problems in Magneto-Solid Mechanics," Mechanics Today, Vol. 4, Nemat-Nasser, S. (ed.), American Academy of Mechanics, Pergammon Press, New York, 1978.
20. Hara, K., "Improvement to a Two-Dimensional Eddy Current Finite Element Program (EDDY2)", Report submitted for CEE782 (Advanced Finite Element Analysis) class at Cornell University, Fall 1981.
21. Jackson, J.D., Classical Electrodynamics, John Wiley and Sons, New York, 1962, p. 40.

22. Abel, J.F. and Shephard, M.S., "An Algorithm for Multipoint Constraints in Finite Element Analysis," Intl. J. of Num. Meth. in Engr., 1979, pp. 464-467.
23. Desai, C.S., and Abel, J.F., Introduction to the Finite Element Method, Van Nostrand-Reinhold, pp. 188-194.
24. Halliday, D., and Resnick, R., Fundamentals of Physics, John Wiley and Sons, Inc., New York, NY, 1974, pp. 537-541.
25. Lapin, L.L., Probability and Statistics for Modern Engineering, Brooks/Cole, Monterey, CA, 1983, p. 334.
26. Cole, A.G., and Brown, A.F.C., "Photoelastic Determination of Stress Concentration Factors Caused by a Single U-Notch on One Side of a Plate in Tension," J. of the Royal Aeronautical Society, V. 62, 1958, pp. 597-598.
27. Peterson, R.E., Stress Concentration Factors, John Wiley and Sons, New York, N.Y., 1974, pp. 20-41.
28. Leven, M.M. and Frocht, M.M., "Stress Concentration Factors for a Single Notch in a Flat Bar in Pure and Central Bending," Trans. ASME, Vol. 74(2), 1952, p. 560.
29. Rajiyah, H., Khushefati, W., Aziz, R., and Khater, M., "Magnetomechanics Problem," Cornell University, CEE772, Finite Element Project, May 1984.
30. Hahn, G.T., and Rosenfield, A.R., "Sources of Fracture Toughness: The Relation between K and the Ordinary Tensile Properties of Metals," Applications Related Phenomena in Titanium Alloys, ASTM STP 432, 1968, pp. 5-32.
31. Hellan, K., Introduction to Fracture Mechanics, McGraw-Hill, New York, 1984, p. 244.
32. Gerstle, W., Personal Communications, Cornell University, July, 1984.
33. Atlas of Microstructures of Industrial Metals, Metals Handbook, Vol. 7, American Society for Metals, 1972.

COMPOSITE LIST OF TECHNICAL REPORTS
TO THE
OFFICE OF NAVAL RESEARCH

NUMERICAL SOLUTIONS FOR COUPLED MAGNETOTHERMOMECHANICS

Contract Number N00014-79-C-0224
Task Number NR 064-621

Departments of Structural Engineering and
Theoretical and Applied Mechanics,
Cornell University,
Ithaca, New York 14853

1. K. Y. Yuan, F. C. Moon, and J. F. Abel, "Numerical Solutions for Coupled Magnetomechanics", Department of Structural Engineering Report Number 80-5, February 1980.
2. F. C. Moon and K. Hara, "Detection of Vibrations in Metallic Structures Using Small Passive Magnetic Fields", January 1981.
3. S. Mukherjee, M. A. Morjaria, and F. C. Moon, "Eddy Current Flows Around Cracks in Thin Plates for Nondestructive Testing", March 1981.
4. K. Y. Yuan, F. C. Moon, and J. F. Abel, "Finite Element Analysis of Coupled Magnetomechanical Problems of Conducting Plates", Department of Structural Engineering Report Number 81-10, May 1981.
5. F. C. Moon, "The Virtual Theorem and Scaling Laws for Superconducting Magnet Systems", May 1981.
6. K. Y. Yuan, "Finite Element Analysis of Magnetoelastic Plate Problems", Department of Structural Engineering Report Number 81-14, August 1981.
7. K. Y. Yuan et al., "Two Papers on Eddy Current Calculations in Thin Plates", September 1981.
8. G. R. Doelp, J. F. Abel, and F. C. Moon, "Experimental and Numerical Analysis of Electric Currents and Electromagnetic Blunting of Cracks in Thin Plates", Department of Structural Engineering Report Number 84-12, December 1984.
9. K. Hara and F. C. Moon, "Stability and Vibrations of Internal Windings of High Current Superconducting Solenoids", December 1984.
10. J. F. Abel, F. C. Moon, and T. J. McCoy, "Pre- and Post-Processing for Stream-Function Eddy Current Calculations", Department of Structural Engineering Report Number 84-13, December 1984.

U219362 .